論文 / 著書情報
Article / Book Information

題目(和文)	傾斜利用ブリルアン光相関領域反射計の提案および性能向上
Title(English)	Proposal and performance improvement of slope-assisted Brillouin optical correlation-domain reflectometry
著者(和文)	李熙永
Author(English)	Heeyoung Lee
出典(和文)	学位:博士(工学), 学位授与機関:東京工業大学, 報告番号:甲第11311号, 授与年月日:2019年9月20日, 学位の種別:課程博士, 審査員:中村 健太郎,梶川 浩太郎,山口 雅浩,植之原 裕行,宮本 智之
Citation(English)	Degree:Doctor (Engineering), Conferring organization: Tokyo Institute of Technology, Report number:甲第11311号, Conferred date:2019/9/20, Degree Type:Course doctor, Examiner:,,,,
学位種別(和文)	博士論文
Type(English)	Doctoral Thesis

Dissertation

博士号請求論文

Proposal and performance improvement of slope-assisted Brillouin optical correlation-domain reflectometry

傾斜利用ブリルアン光相関領域反射計の提案および性能向上

Supervisor: **Professor Kentaro NAKAMURA**

指導教員: 中村 健太郎 教授

Submitted on August 2019

2019年 8月 提出

Department of Electrical and Electronic Engineering,
School of Engineering, Tokyo Institute of Technology
東京工業大学 工学院 電気電子系

Heeyoung LEE

李 熙永

Contents

1 Introduction

In this Chapter, I introduce the overall background and the aim of this dissertation. First of all, I briefly describe the history of glass and polymer optical fibers. Next, I will explain the fundamentals of Brillouin scattering in optical fibers and the principle of Brillouin-based optical fiber sensing. Then, I review some of the conventional distributed Brillouin sensing techniques, which include Brillouin optical time-, frequency, and correlation-domain analysis/reflectometry. Finally, I present the purpose of this thesis.

1. 1 Optical fibers

It was in 1966 that Prof. Charles K. Kao [1] made a greatest-ever discovery in fiber optics, which laid the groundwork for the evolution of the Internet. He calculated how light can be propagated over a long distance along an optical glass fiber and found that, using a fiber composed of perfectly pure glass, light can be propagated for >100 km. Note that the longest propagation distance for the fibers available in the 1960's was only 20 m [2–4]. Inspired by his achievement, other researchers shared his vision of the future potential of fiber optics. Just four years later, the first ultrapure fiber with a propagation loss of <20 dB/km was fabricated [5]. Further progress in fabrication technology [6] led to a loss of only 0.2 dB/km at 1.55 μm [7], where the loss level was limited by the fundamental process of Rayleigh scattering. The availability of low-loss silica fibers has brought a revolution in fiber-optic communications [8–10] and sensing [11–14]. It was no wonder that Kao, currently known as the "Godfather of Broadband" and the "Father of Fiber Optics", was awarded the 2009 Nobel Prize in Physics for his "groundbreaking achievements concerning the transmission of light in fibers for optical communication". In 2018, while I was working on fiber-optic sensing as a Ph.D

candidate, he passed away at the age of 84. I would like to respectfully express my sincere condolences.

To date, silica fibers are the most commonly used optical fibers not merely for network communication but for fiber-optic sensing, which I describe in the next section. However, they are extremely fragile and break easily even when a relatively small strain is applied. One method for reducing the fragility is to coat the glass fibers with some smooth materials such as polymer, but as long as the cores are composed of glass, they cannot withstand much larger strains. Extremely flexible fibers with polymer cores are referred to as polymer (or plastic) optical fibers (POFs), which have been attracting considerable attention recently. The first product of POFs named “Eska” was commercialized in 1975 by Mitsubishi Rayon Co. Ltd., in Japan. As the propagation loss is high (440 dB/km at 650 nm) partly because of its step-index structure, Eska was not suitable for longer-range applications. In 1990, to improve the propagation loss, led by Prof. Yasuhiro Koike, Keio University succeeded in inducing graded-index structure into the core of POFs and achieved a relatively low loss of 143 dB/km at 650 nm [15], which was still far from being sufficient at that time. However, using perfluorinated polymer as core material, the same group has recently reduced the propagation loss to < 40 dB/km; the low-loss wavelength window is currently extended even to telecom wavelength [16]. As the propagation loss of perfluorinated graded-index POFs is higher than that of silica glass fibers, POFs have been exploited for medium-range applications, such as home and in-vehicle networks [17] as well as for large-strain sensing applications [18]. What is notable about POF sensing is its “memory effect” [19, 20], which will provide a new function to the existing fiber-optic sensing techniques.

1. 2 Optical fiber sensors based on Brillouin scattering

Health monitoring of civil structures, such as buildings, dams, tunnels, bridges, highways, pipelines, railway lines, containers, airplanes, ships, aircraft wings, windmill blades, etc., is beneficial from the economic and security viewpoints. Using an appropriate sensing system, we can obtain information about the structural conditions (e.g., damages caused by earthquakes and aging deterioration), which can be used to

design repair schedules and to provide early warnings which will someday result in a catastrophic failure. Health monitoring has been traditionally performed based on visual inspection [21]. This method is, however, limited in time and scope, since it is only possible to see degradations that are visible and apparent at the time of the inspection. Moreover, one can only see degradations relative to the original state (or the state at the previous inspection), but the defects hidden in the structure from the start cannot be detected. Fitting the structure with a comprehensive sensor network capable of continuously gathering information on all relevant structural parameters offers a better way of assessing its actual behavior. Various types of sensors have been developed for over a half century to measure structural parameters, such as strain, temperature, pressure, rotation, oscillation, humidity, and acceleration. A number of researchers now believe that optical fiber sensors — in particular, distributed Brillouin sensors — will also be a key technology to fulfill this purpose. Prof. Kazuo Hotate, who was a professor at the University of Tokyo and now serves as President at Toyota Technological Institute, named such systems “fiber-optic nerve systems” because these structures can “feel pain” just like human beings [22, 23].

1. 2. 1 Brillouin scattering in optical fibers

Light scattering in optical fibers is omnipresent irrespective of the amount of optical power present in the fibers. When a monochromatic lightwave at frequency f_0 is launched into a fiber, it is scattered via three kinds of scattering phenomena (Fig. 1.1). These scatterings physically correspond to two cases: elastic scattering and inelastic scattering. In elastic scattering, that is, Rayleigh scattering, the scattered photons maintain their energy and thus have the same frequency as the incident light. On the other hand, in inelastic scattering, that is, Brillouin scattering (interaction with acoustic phonons) and Raman scattering (interaction with optical phonons), the scattered photons lose or gain energy and thus undergo a frequency shift. In “Stokes-type” scattering, the photons lose energy and their frequency is downshifted, whereas in “anti-Stokes-type” scattering, the photons gain energy with their frequency upshifted. Among these scatterings, Brillouin scattering [24] is especially suitable for developing distributed

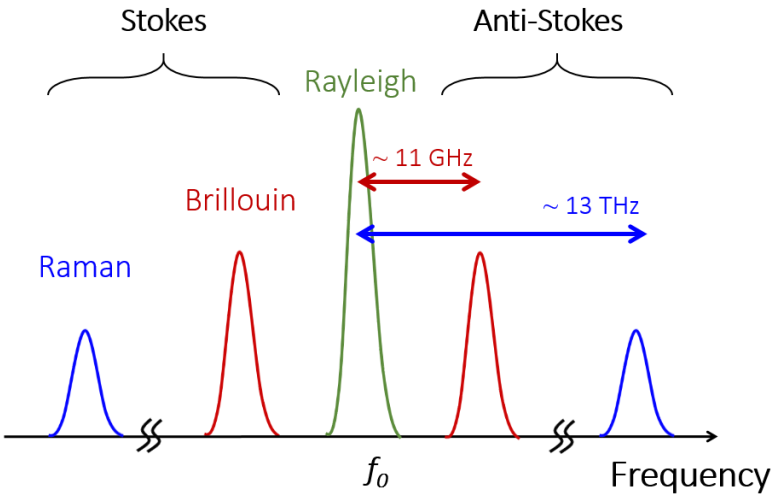

Fig. 1.1 Schematics of the spectra of the reflected light via Rayleigh, Brillouin, and Raman scattering in optical fibers.

sensors, because its frequency shift is linearly dependent on both strain [25] and temperature [26], as detailed later. In this thesis, we will focus on Brillouin scattering.

Brillouin scattering is a photon-phonon interaction; in other words, it is based on the annihilation of a pump photon that creates a Stokes photon and a phonon simultaneously. The phonon is the vibrated modes of molecules (i.e., an acoustic phonon). The Brillouin frequency shift (BFS) is approximately 11 GHz in silica fibers. This mechanism can be more classically understood in the following way. At non-zero temperature, the molecules involved in the fiber are thermally oscillating at numerous frequencies or wavelengths. When one of these wavelengths is the same as half of the optical wavelength in the fiber (Bragg's condition), the incident light is strongly scattered. As this "grating" is moving forward (in the case of Stokes) at an acoustic velocity, the frequency of the scattered light is downshifted owing to a Doppler effect by the amount of BFS, which is determined by the acoustic velocity (i.e., by the Young's modulus and density).

Brillouin scattering is classified into two configurations: spontaneous and stimulated scattering. The configuration for spontaneous Brillouin scattering is shown in Fig. 1.2(a), where only one pump light beam is injected into one end of the fiber. Its reflectivity is extremely low (even lower than that of Rayleigh scattering). In contrast, the reflectivity of stimulated Brillouin scattering is tens of dB higher than that of spontaneous scattering, which is attractive from the viewpoint of a signal-to-noise ratio

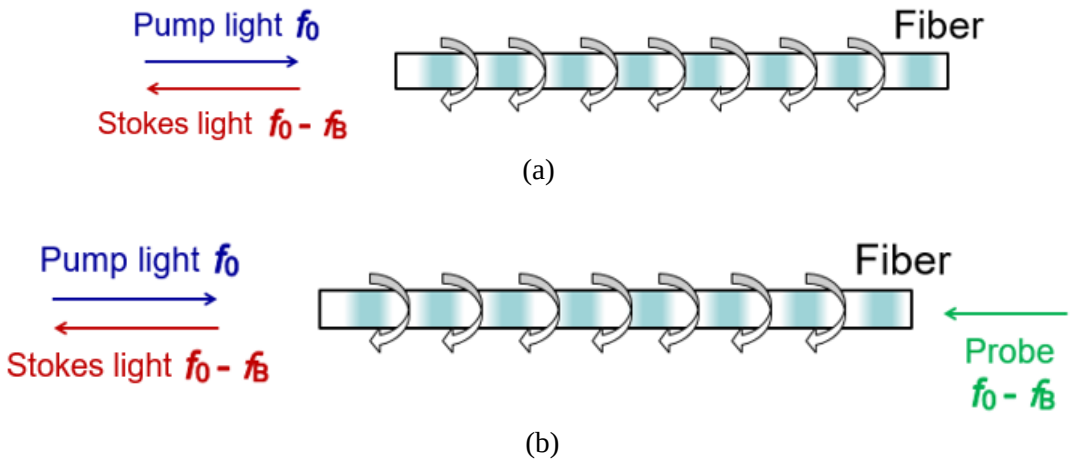

Fig. 1.2 Schematics of (a) spontaneous Brillouin scattering and (b) stimulated Brillouin scattering.

(SNR) of the system. However, stimulated scattering requires a probe light beam injected into the other end of the fiber besides the pump light (Fig. 1.2(b)), which sometimes lacks practical convenience of end-users. Thus, depending on the priority of the system performance, spontaneous and stimulated Brillouin scatterings are both used to develop fiber-optic sensors, as detailed in the next section.

1. 2. 2 Brillouin-based optical fiber sensors

As already mentioned, because of increasing demand for structural health monitoring techniques, a wide variety of fiber-optic sensors have been developed [27–29]. Above all, those based on Brillouin scattering [24] have been gathering worldwide attention owing to their capability of measuring strain and temperature distributions. As I have already described how to measure the magnitude of strain and temperature change in the previous section, what is important next is how to resolve the locations where strain or temperature change is applied. There are some spatially resolving methods, such as time-, frequency-, correlation-domain techniques. In this section, I survey their basic concepts.

Fiber-optic Brillouin sensors can be classified into six configurations, which are called Brillouin optical time-domain analysis (BOTDA) [30–40] and reflectometry

(BOTDR) [41–47], Brillouin optical frequency-domain analysis (BOFDA) [48, 49] and reflectometry (BOFDR) [50], and Brillouin optical correlation-domain analysis (BOCDA) [51–60] and reflectometry (BOCDR) [61–74]. Each configuration has its unique merits and demerits and has been extensively studied.

In analyzers (BOTDA, BOFDA, and BOCDA), stimulated Brillouin scattering with a relatively high reflectivity is used, resulting in a high SNR. As a result, high sensing performances, such as an ultimately fast measurement speed in BOTDA [40] and a nominal spatial resolution of as high as 1.6 mm in BOCDA [55], have been achieved. However, analyzers require light injections to both ends of a fiber under test (FUT), which reduces the degree of freedom in embedding the FUT into structures; they do not operate appropriately when the FUT has one breakage point, either. In addition, relatively expensive devices, such as single-sideband modulators, are often needed to generate probe light. Thus, from the users' standpoint, reflectometers (BOTDR, BOFDR, and BOCDR) which operate by single-end light injection are preferable, even if their SNR is relatively low owing to the use of spontaneous scattering.

In BOTDR, short optical pulses are used to resolve the positions by a well-known time-of-flight technique. BOTDR has a measurement range of several tens of kilometers or longer, and its spatial resolution is determined by the width of the optical pulses. However, when the width is lower than ~10 ns, the Brillouin spectrum is broadened, resulting in the inherent limitation of the resolution of ~1 m [75]. Using a special scheme, such as double-pulse configuration [47], the spatial resolution has been enhanced, but it is still in the order of (tens of) centimeter. As the reflected light signals of numerous pulses need to be processed, its relatively low operating speed is also a problem. BOFDR has been very recently developed by Aldo Minardo [50]. This system is based on the use of a pump light the amplitude of which is sinusoidally modulated at a variable frequency. Although BOFDR requires only less expensive electrical devices for relatively low-frequency uses, it is still at the stage of the first demonstration and its performance reported so far is far from being sufficient for practical use. Thus, the third configuration called BOCDR is the only technique that can simultaneously achieve operation by single-end light injection and high spatial resolution of millimeter order. This is why BOCDR is focused on in this thesis.

1. 3 Brillouin optical correlation-domain reflectometry (BOCDR)

In 2008, attempting to implement a single-end-access configuration of BOCDA, Yosuke Mizuno succeeded in demonstrating the basic operation of BOCDR [61], which can measure the distribution of strain and temperature along an FUT by light injection from merely one end.

The conceptual schematic of the proposed BOCDR system is shown in Fig. 1.3 [61]. A light beam from a laser is divided into pump and reference light beams. The pump light is injected into the FUT, and the Stokes light is directed into a heterodyne receiver composed of two balanced photodiodes (PDs). The reference light is used as an optical local oscillator. The electrical beat signal of the two light beams is monitored by an electrical spectrum analyzer (ESA). Since there is, without any additional frequency shifters, a frequency difference of about 11 GHz between the Stokes light and the reference light, this configuration is called self-heterodyne scheme.

In order to resolve the position in the FUT, the optical frequency of the light beam from the laser is directly modulated in a sinusoidal wave by modulating the injection current to the laser. From the viewpoint of time averaging, the correlation (or coherence) function is synthesized into a series of periodical peaks [76], whose period is inversely proportional to the frequency of the sinusoidal modulation f_m. By controlling

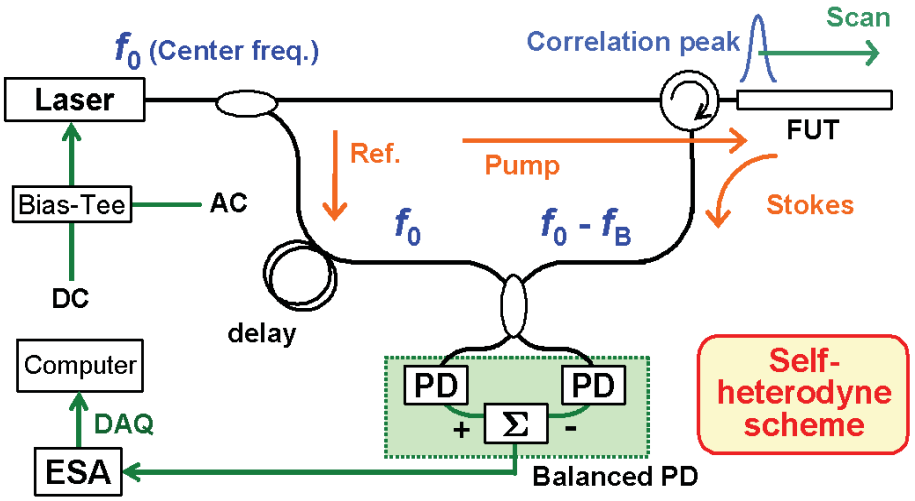

Fig. 1.3 Conceptual schematic of BOCDR. AC, alternating current; DAQ, data acquisition; DC, direct current; ESA, electrical spectrum analyzer; FUT, fiber under test; PD, photo diode.

f_m to leave only one correlation peak within the range of the FUT, so that only the Brillouin scattering generated at the position correspondent to the peak has high correlation with the reference light, and then gives high heterodyne output. The peak frequency observed in the ESA gives the BFS caused at the position. By sweeping f_m, the correlation peak is scanned along the FUT to obtain the distribution of BGS or BFS, thus, distributed BFS measurement becomes feasible. Sinusoidal frequency modulation results in the periodic generation of multiple correlation peaks along the FUT, and their frequency determines the measurement range d_m (distance between the neighboring correlation peaks) by [62],

$$d_m = \frac{c}{2n f_m} \tag{1-1}$$

where c is the velocity of light in vacuum and n is the core refractive index. When f_m is lower than the Brillouin bandwidth $\Delta\nu_B$, the spatial resolution Δz is also given by [62],

$$\Delta z = \frac{c\Delta\nu_B}{2\pi n f_m \Delta f} \tag{1-2}$$

where Δf is the modulation amplitude of the optical frequency.

Since the basic BOCDR system was first proposed [61], numerous configurations have been developed in order to improve its performance [65–74]. For example, the measurement range was elongated using temporal gating [65] and double modulation [66]; millimeter-order spatial resolution was achieved by use of a tellurite glass fiber [67] and by apodization [68]; and the strain dynamic range was extended using polymer optical fibers [69–73]. However, its sampling rate was lower than 20 Hz, which was not sufficient for some practical applications. Thus, it is of crucial importance to develop high-speed BOCDR to real-time distributed strain and temperature measurements or vibration measurements.

1. 4 Objectives and constitution of this thesis

The purpose of this thesis is to propose a new BOCDR configuration—named slope-assisted (SA-) BOCDR—to achieve real-time distributed measurements and to improve

its performance from a variety of aspects. Finally, we perform pseudo-field tests toward future development of SA-BOCDR-based structural health monitoring system.

In order to achieve these objectives, this thesis consists of six chapters, including the present Introduction. The structure of the thesis is illustrated in Fig. 1.4.

Following Chapter 1: "Introduction," in Chapter 2: "Proposal of slope-assisted (SA-) BOCDR," a new configuration of BOCDR assisted by the slope of the BGS—named slope-assisted (SA-) BOCDR—is proposed. After explaining its principle, we experimentally verify the basic operation of simultaneous distributed measurement of strain, temperature and loss with a high sampling rate.

In Chapter 3: "Characterization," the detailed operation of the system is described. After investigating the system output of SA-BOCDR both theoretically and experimentally, we show that SA-BOCDR has a unique ability to detect strained or heated sections even shorter than the nominal spatial resolution. This "beyond-nominal-resolution" effect is well clarified, and the shortest-ever hotspots are detected using this effect both in silica and polymer fibers. Then, the influences of the experimental conditions, such as incident power and spatial resolution, on the measurement

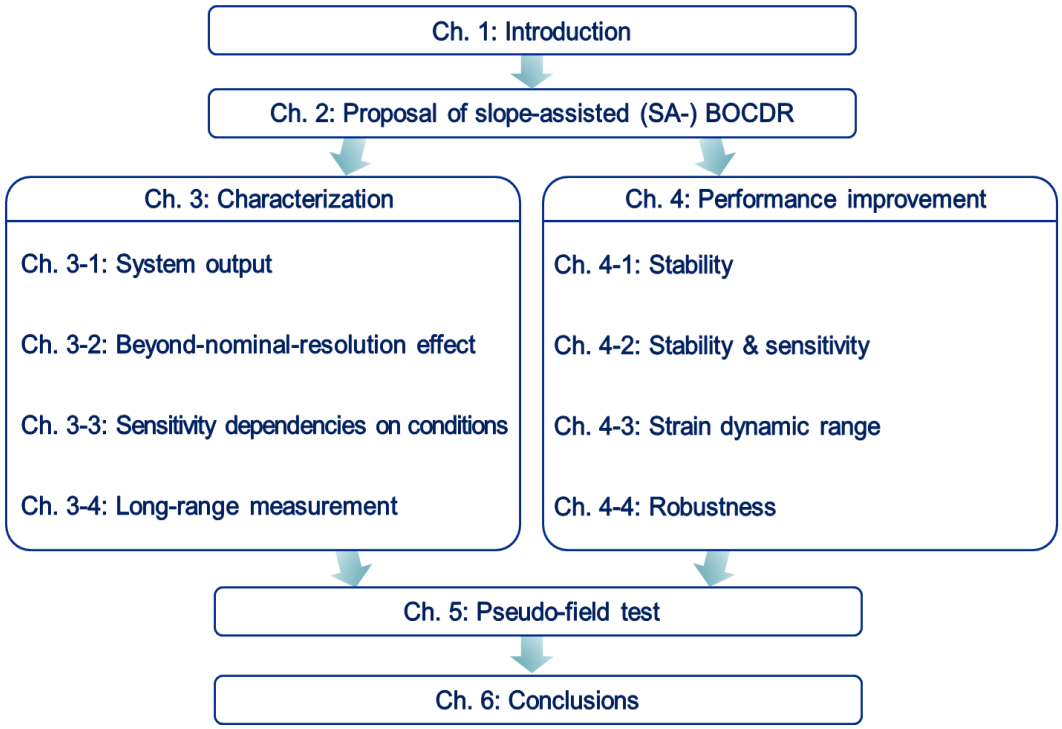

Fig. 1.4 Structure of this thesis.

sensitivity of SA-BOCDR are investigated. Finally, we demonstrate SA-BOCDR with a long measurement range of >10 km to enhance its applicability.

In Chapter 4: “Performance improvement,” we provide experimental results for the enhancement of stability, sensitivity, strain dynamic range, and robustness. First, loss-insensitive operation of SA-BOCDR is demonstrated using a trench-index-type special silica fiber. Then, by employing polarization maintaining fibers and optimizing the state of polarization, polarization-dependent power fluctuations are suppressed and the measurement sensitivity are improved. The strain dynamic range is also enhanced by investigating its trade-off relation to the spatial resolution. Finally, we demonstrate distributed strain and temperature measurements based on SA-BOCDR using a POF. Unlike a silica fiber, POF can endure large strains of over several tens of percent and provide much higher temperature sensitivity.

In Chapter 5: “Pseudo-field test,” an example of structural diagnosis using SA-BOCDR is provided to show the practical usefulness of the system. As a specimen, we prepare a carbon-fiber-reinforced-plastic strengthened steel plate, in which a standard silica fiber is embedded. The tensile and compressive strains are then applied to the embedded fiber by applying load to the specimen using a three-point bending device, and distributed strain measurements are performed. The obtained results moderately agree with the theoretical trends. In addition, we carry out similar experiments by applying larger strains until the embedded fiber is broken, and show that the detection of fiber breakage is feasible by measuring loss distributions.

In Chapter 6: “Conclusions,” we summarize each Chapter of this thesis and provide concluding remarks by discussing which of the two configurations, standard BOCDR or SA-BOCDR, should be used in practical situations.

2 Proposal of slope-assisted (SA-) BOCDR

In this Chapter, using the slope of the Brillouin gain spectrum, we propose a new configuration of Brillouin optical correlation-domain reflectometry (BOCDR)—named slope-assisted (SA-) BOCDR—which can measure strain, temperature and even loss distributions simultaneously with a high sampling rate. The strain, temperature, and loss dependence coefficients of the output signal are measured to be 1.95×10^{-4} dB/με, 4.42×10^{-3} dB/K, and 0.191, respectively, which well agrees with the theoretical predictions. The basic operation of the system is verified through simultaneous distributed measurement of the three parameters with a high sampling rate

2. 1 Preface

Among Brillouin-based fiber-optic distributed sensors, BOCDR has been extensively studied since it is the only scheme with single-end accessibility and high spatial resolution. However, one of the important drawbacks of standard BOCDR is its limited sampling rate due to the necessity of acquiring the whole Brillouin gain spectrum (BGS) to obtain the Brillouin frequency shift (BFS) values (corresponding to strain and temperature).

Thus, to overcome this drawback and to achieve real-time distributed measurement with intrinsic single-end accessibility and a high spatial resolution, we develop a new BOCDR configuration—named slope-assisted BOCDR (SA-BOCDR) in analogy with SA-BOTDA [77, 78]—which operates with the assistance of the BGS slope. In this method, the whole BGS need not be observed to derive the BFS value, which leads to a higher sampling (or repetition) rate in principle. In addition, since it operates based on power information, unlike standard (frequency-based) BOCDR, newly developed SA-BOCDR can provide loss distribution along the fiber under test (FUT).

2. 2 Principle

In standard BOCDR systems, the BFS (i.e. strain or temperature) at one sensing point is derived after obtaining the whole BGS. In contrast, the main idea of SA-BOCDR is to exploit BGS slope. As depicted in Fig. 2.1(a), the BFS is in one-to-one correspondence with the spectral power P_{B0} at a certain frequency ν_{B0}, which is set at the high-frequency point in the linear region (lower-frequency side) of the BGS slope. When the FUT is strained or heated and BFS shifts to a higher frequency, P_{B0} decreases almost linearly. Then, when the slight loss occurs in the FUT, since the propagation light decreased entirely from the loss point, the spectral power of the BGS decreases, leading to the reduction of P_{B0}.

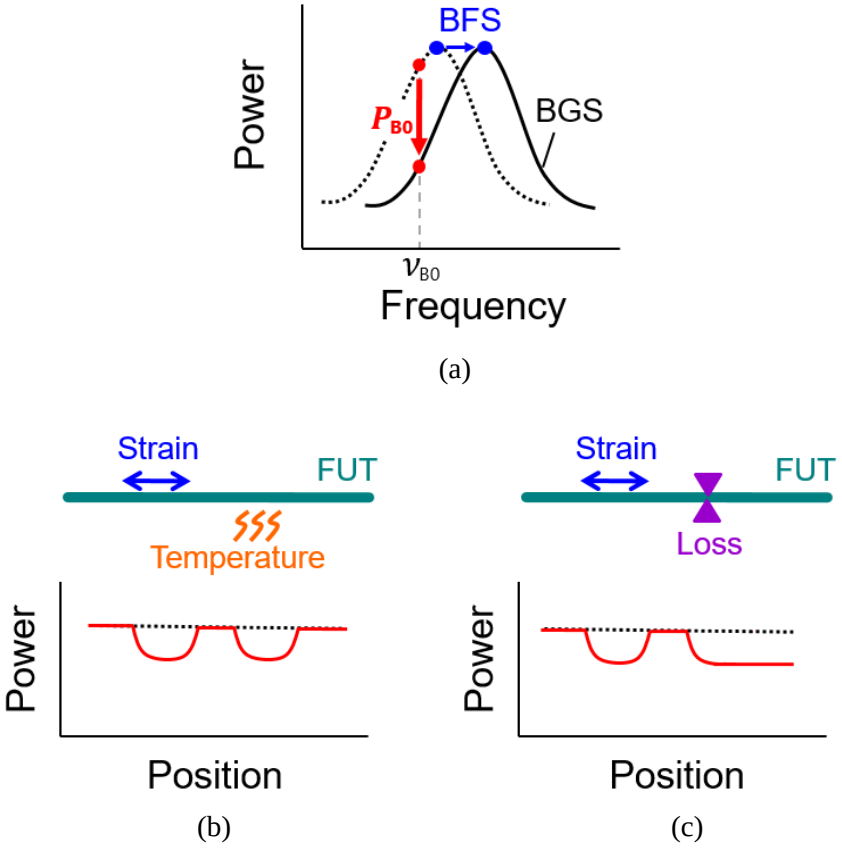

Fig. 2.1 Schematic illustrations of the operating principle of SA-BOCDR. (a) One-to-one correspondence between the BFS and the spectral power P_{B0} at frequency ν_{B0}. The dotted curve is the initial BGS, and the solid curve is the BGS shifted to higher frequency on account of strain and/or heat. (b) P_{B0} distributions along the sensing fiber with (solid curve) and without (dotted line) partial strain and heat. (c) P_{B0} distributions along the sensing fiber with (solid curve) and without (dotted line) partial strain and a point loss.

Figures 2.1(b) and 2.1(c) schematically show the changes in the P_{B0} distributions when strain (or temperature change) and loss are locally applied, respectively. Note that the strain and temperature effects cannot be separated in this method, but the loss effect can be discriminated from the locally applied strain (or temperature change) because the once decreased P_{B0} value does not return to the initial value (If strain (or temperature change) is applied from a certain point to the distal end of the FUT, it cannot be separated from the point loss; in which case, the problem could be resolved by utilizing the ratio of the spectral powers at two frequencies. The details will be published elsewhere). The P_{B0}

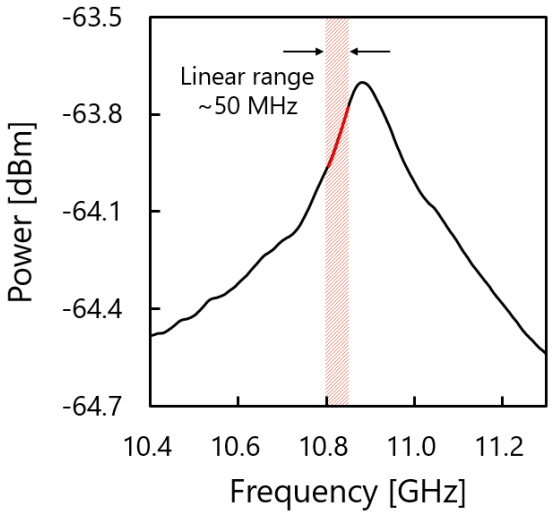

(a)

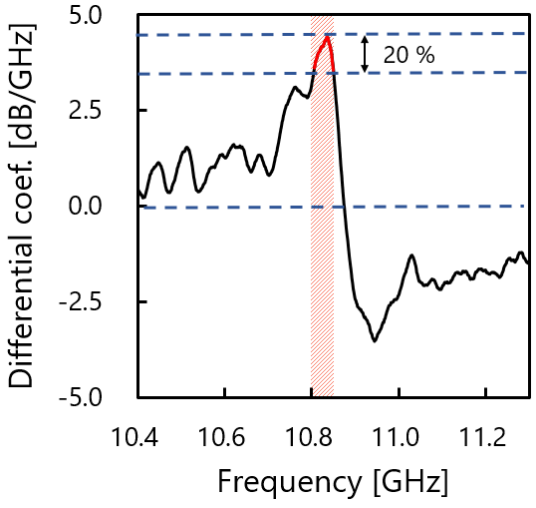

(b)

Fig. 2.2 (a) Measured BGS and (b) its differential coefficient at each frequency. Highlighted region indicates the linear region of the BGS (lower-frequency side is indicated).

change distributions (calculated by substituting the resultant P_{B0} distributions (solid curves) from their initial distributions (dotted lines)) are used as final measurement data.

As shown in Fig. 2.2(a), to evaluate the optimal ν_{B0} value and the bandwidth of the linear region, we analyzed a raw BGS with a BFS of 10.89 GHz, which was experimentally obtained when the FUT length L and experimental conditions (such as the modulation frequency f_m and amplitude Δf) were set to the same values as those for the experiment (L = 5.0 m, f_m = 8.0 MHz, Δf = 1.4 GHz; refer to the following sections). Here, we define the linear region as the region where the change in the BGS slope is suppressed within 20% compared to its maximum. Based on the slope (i.e. differential coefficient) dependence on the frequency (Fig. 2.2(b)) obtained by differentiating the BGS with respect to frequency, the optimal ν_{B0} value to widen the linear region was found to be 10.85 GHz. The bandwidth of the linear region was approximately 50 MHz, which corresponds to the strain of up to ~1035 με and the temperature change of ~45 K. In this linear region, the theoretical strain and temperature dependence coefficients were calculated to be 2.11×10^{-4} dB/με and 4.27×10^{-3} dB/K, respectively. Note that these coefficients will be different if the experimental conditions alter. For instance, if the spatial resolution is set lower, the coefficients will be larger, while if the video bandwidth (VBW) of an electrical spectrum analyzer (ESA) is set lower, they will be smaller.

2. 3 Experimental setup

We employed a 5.0-m-long silica single-mode fiber (SMF) as an FUT. Its BFS at 1.55 μm at room temperature was 10.89 GHz. Figure 2.3 shows the experimental setup of SA-BOCDR, which is basically the same as that of standard BOCDR [61, 62]. The final signal processing is mainly different from the standard BOCDR. The output light from a distributed-feedback laser diode at 1.55 μm was divided into two light beams, pump and reference. The pump light was amplified to ~24 dBm using an erbium-doped fiber amplifier (EDFA) and injected into the FUT. After passing through a ~1-km-long delay line and another EDFA (amplified to ~5 dBm), the reference light was used for heterodyne detection with the Stokes light, which was amplified to ~2 dBm. The heterodyned optical signal was converted into an electrical signal using a photo diode

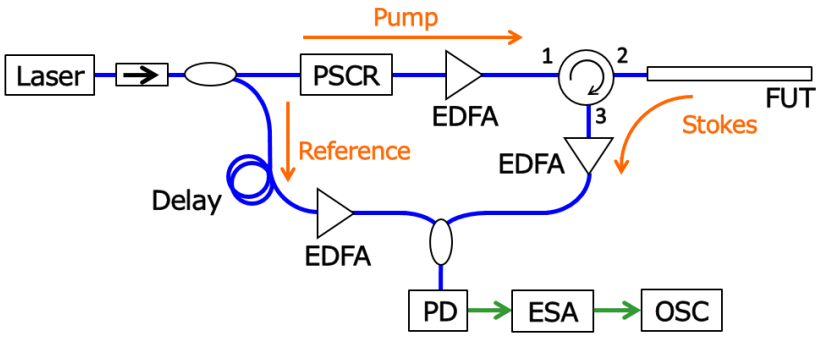

Fig. 2.3 Experimental setup of SA-BOCDR. EDFA, erbium-doped fiber amplifier; ESA, electrical spectrum analyzer; FUT, fiber under test; LD, laser diode; OSC, oscilloscope; PD, photo diode; PSCR, polarization scrambler.

(PD) and was guided to an ESA (VBW: 3 kHz, resolution bandwidth: 300 kHz). Using the narrowband-pass filtering function of the ESA, the P_{B0} change at a fixed frequency ν_{B0} (= 10.85 GHz) was sequentially output to an oscilloscope (OSC). The polarization-dependent fluctuations were suppressed using a polarization scrambler (PSCR).

A 0.1-m-long section around the distal open end of the FUT was bent to suppress the Fresnel reflection. The modulation frequency f_m and amplitude Δf were set to 7.975–8.055 MHz and 1.4 GHz, respectively, corresponding to the measurement range of 12.9 m and the theoretical spatial resolution of 88 mm from the equations in [62]. The repetition rate was 100 Hz, and 16 times averaging was performed on the OSC. The room temperature was 26°C.

2. 4 Experimental results

First, we investigated the P_{B0} change dependence on strain. Strains of 0 to 850 με were applied to a 0.2-m-long section (3.5–3.7 m away from the circulator) of the FUT. The measured P_{B0} change distributions along the FUT are shown in Fig. 2.4(a). With increasing strain, the P_{B0} change increased (P_{B0} itself decreased). The P_{B0} change dependence was almost linear in this range (Fig. 2.4(b)), and its coefficient was 1.95×10^{-4} dB/με, which moderately agrees with the theoretical value (2.11×10^{-4} dB/με). Note that, in Fig. 2.4(a), the SNR was so low that relatively small strains of < 300 με were unable

to be distinguished from the signal fluctuations in this measurement.

Subsequently, the P_{B0} change dependence on temperature was measured. The result obtained when the temperature was locally changed to 75°C in a 0.2-m-long section (2.0–2.2 m) is shown in Fig. 2.4(c). With increasing temperature, the P_{B0} change increased. As shown in Fig. 2.4(d), the P_{B0} change dependence was almost linear with a coefficient of 4.42×10^{-3} dB/K, which agrees with the theoretical value (4.27×10^{-3} dB/K).

The loss dependence of the P_{B0} change distribution was also measured. Bending losses of 0 to 2.8 dB were applied at a midpoint of the FUT (2.5 m away from the circulator).

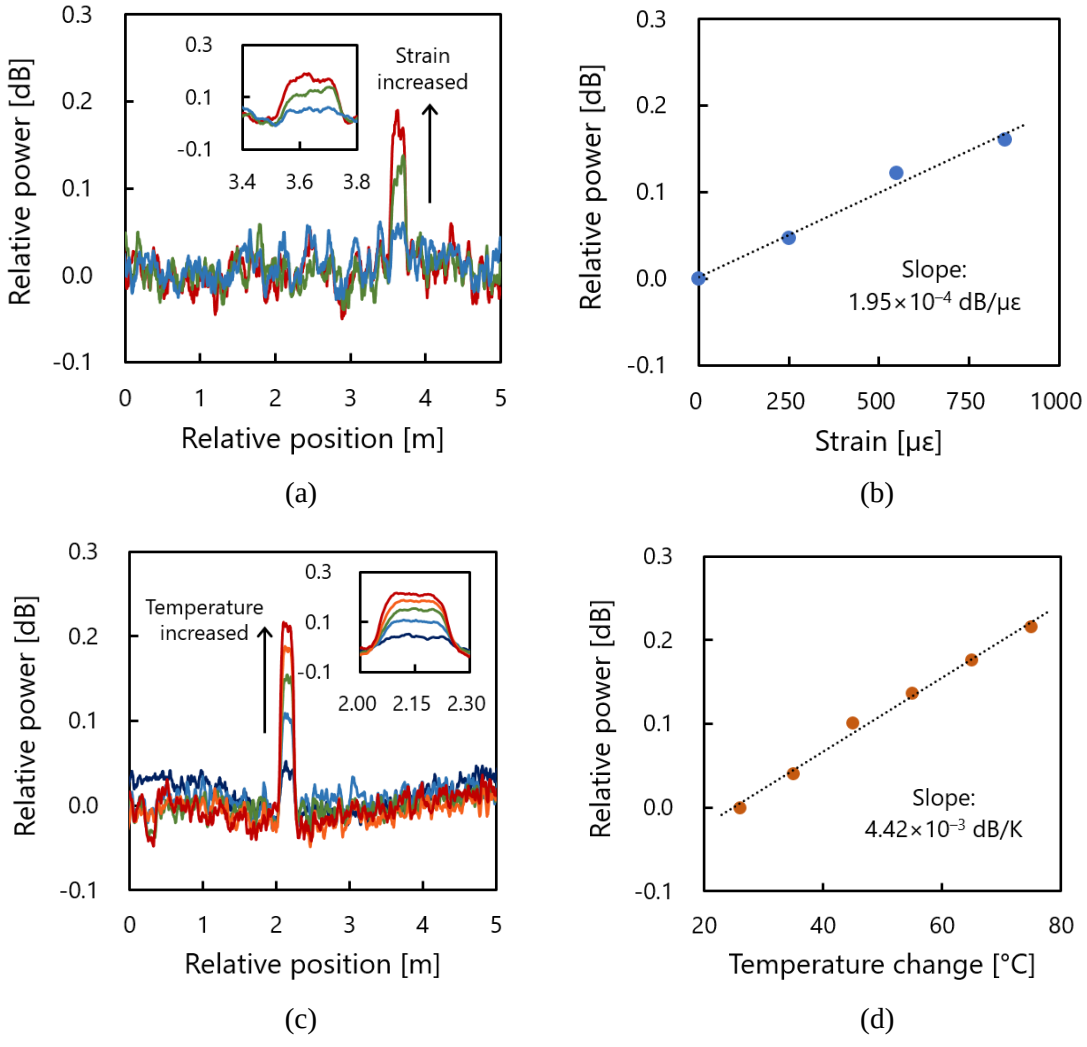

Fig. 2.4 (a) P_{B0} change distribution when strains were locally applied, and (b) P_{B0} change dependence on strain. The dotted line is a linear fit. (c) P_{B0} change distribution when temperature was locally changed, and (d) P_{B0} change dependence on temperature. The dotted line indicates a linear fit.

As shown in Fig. 2.5(a), with increasing loss, the P_{B0} change increased on the distal side from the loss-applied point (again, note that the P_{B0} value itself decreased). The loss dependence of the P_{B0} change (averaged in the 2.5-m-long distal section (2.5–5.0 m)) was almost linear (Fig. 2.5(b)) with a coefficient of 0.191.

We then evaluated the stability of this method. When neither strain/temperature change nor loss was applied to the FUT, we measured the temporal variations of P_{B0} for 20 ms

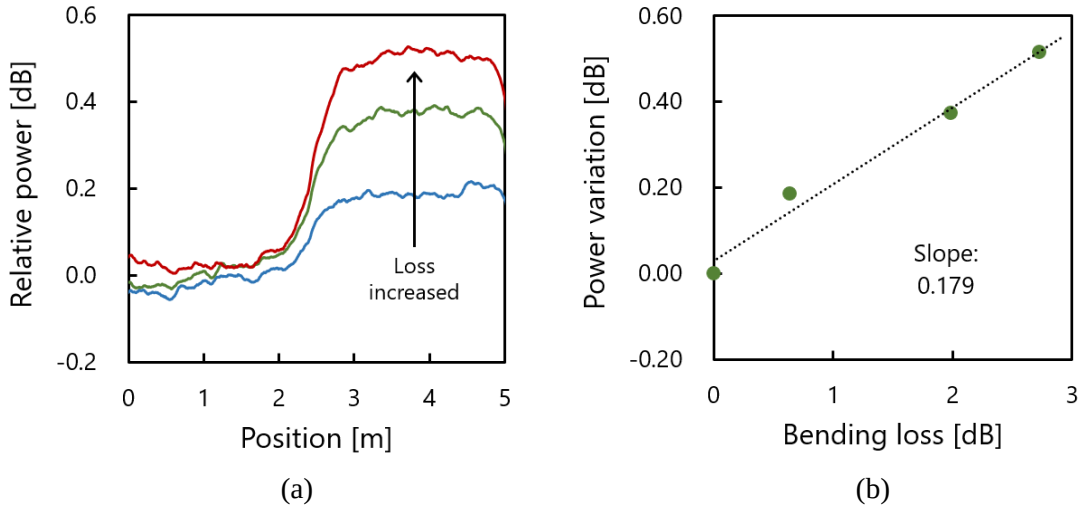

Fig. 2.5 (a) P_{B0} change distribution when losses were locally applied, and (b) P_{B0} change dependence on loss. The dotted line is a linear fit.

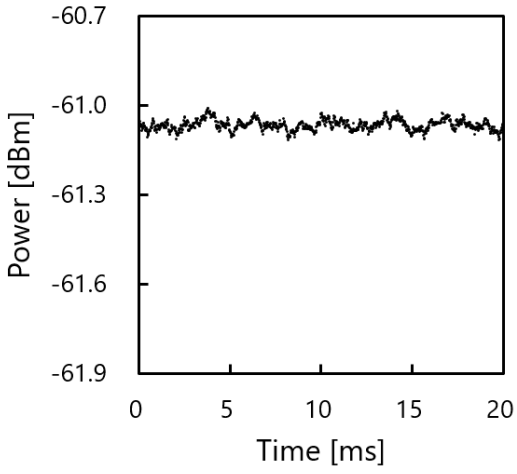

Fig. 2.6 Measured temporal variations of P_{B0}.

(Fig. 2.6). The standard deviation was calculated to be ~0.0178 dB, which corresponds to a strain error of +/– 92 με, a temperature error of +/– 4 K, and a loss error of +/– 0.1 dB. These values, which can be suppressed further by averaging more data at the cost of a

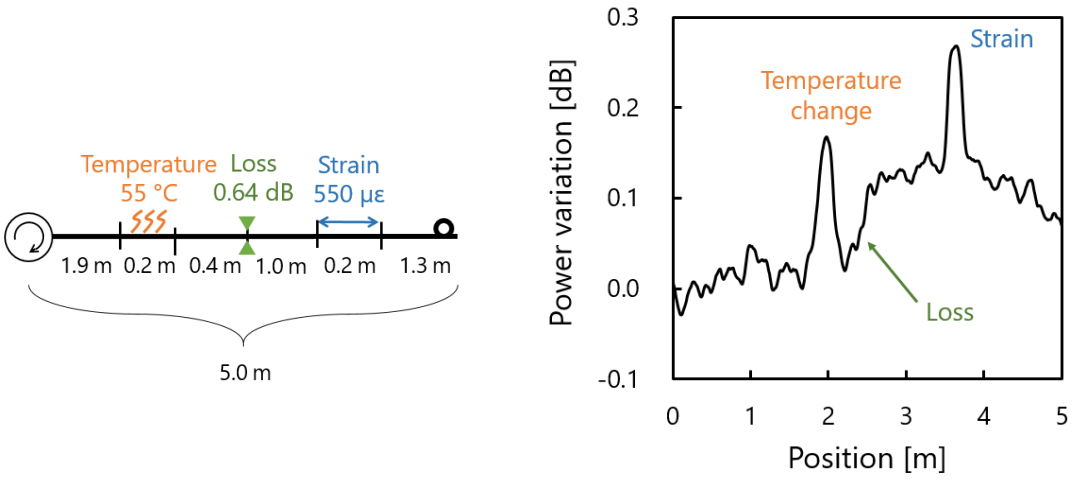

(a) (b)

Fig. 2.7 (a) Structure of the FUT. (b) Measured P_{B0} change distribution.

reduced sampling (or repetition) rate, showed no quantifiable changes when the measurement time was longer than 10 minutes.

Finally, a proof-of-concept demonstration of SA-BOCDR was performed by simultaneous measurement of strain, temperature, and loss. The structure of the 5.0-m-long FUT is shown in Fig. 2.7(a); ambient temperature was changed to 55°C along the 1.9–2.1-m section, a 0.64 dB loss was applied at the midpoint, and a 550 με strain was applied to the 3.5–3.7-m section. Figure 2.7(b) shows the measured P_{B0} change distribution along the FUT. The P_{B0} changes corresponding to the temperature change, loss, and strain were observed at the expected sections. The amounts of the P_{B0} changes for the temperature change, loss, and strain were approximately 0.16, 0.14, and 0.12 (= 0.26 – 0.14) dB (corresponding to the temperature change, loss, and strain of ~62°C, ~0.73 dB, and ~615 με, respectively). The measurement errors probably originate from the signal fluctuations and the resultant low SNR, which needs to be improved by optimal low-pass filtering and/or increase in the number of averaging in future.

2. 5 Discussions

Before make the conclusions, here we make a discussion on operating speed of standard BOCDR and SA-BOCDR. Figure 2.8(a) shows the measured BGS with a frequency span of 500 MHz when the spatial resolution and measurement range of the system are ~90 mm and ~13 m, respectively. To clarify the measurement error of SA-BOCDR, we measured the temporal variation of spectral power for 20 ms, as shown in Fig. 2.8(b). From this result, it was found that the standard deviation corresponds to a strain error of +/– 46 με and a temperature error of +/– 2 K. Since the BGS power fluctuations of BOCDR becomes the measurement error of SA-BOCDR, these obtained values are regarded as measurement error of strain and temperature in SA-BOCDR. Then, the measurement error dependence on the number of measured points in the frequency span of 500 MHz was plotted as described in Fig. 2.9. With decreasing the number of points, the measurement error drastically increased. The result shows that the spectral power should be obtained at least from eight points to keep the measurement error level of the standard BOCDR system same as that of the SA-BOCDR, which indicates that the measurement speed of SA-BOCDR is expected to be at least eight times faster than that of the standard BOCDR.

However, considering that the BGS shifts to a higher frequency as strain or temperature change is applied to the sensing fiber, the frequency span should be wider than 500 MHz.

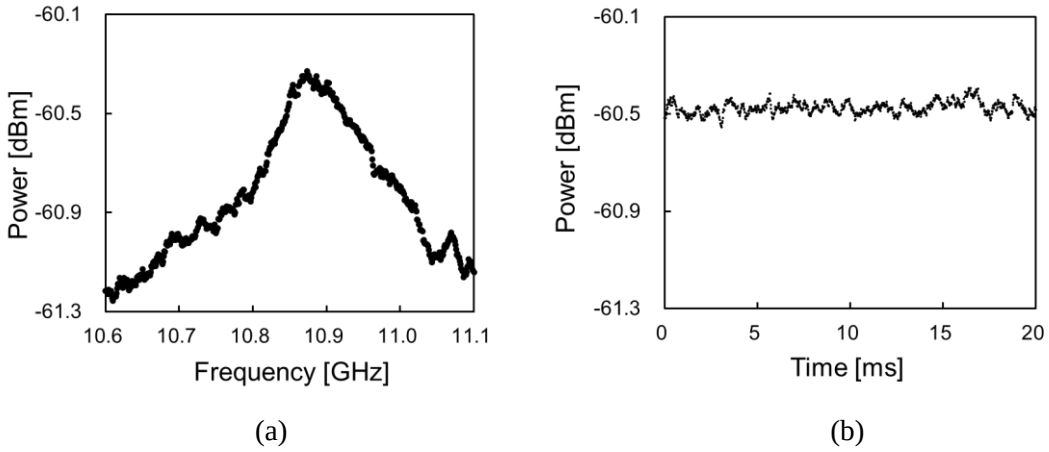

Fig. 2.8 (a) Measured BGS, and (b) temporal variations of spectral power.

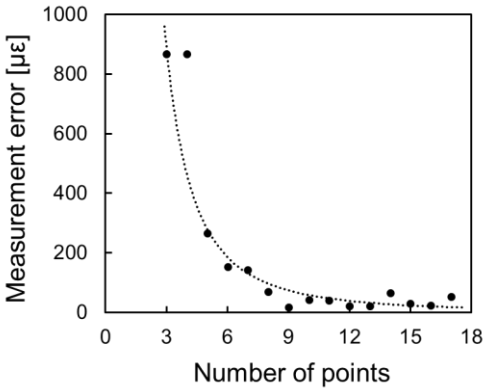

Fig. 2.9 Measurement error dependence on number of points in standard BOCDR.

Furthermore, the number of measurement points are set more than eight in most practical cases to achieve highly accurate measurements. Therefore, the operating speed of SA-BOCDR is expected to be significantly faster than eight times in actual sites.

2. 6 Conclusions

We experimentally proved the concept of a new BOCDR configuration, SA-BOCDR, which can perform the simultaneous distributed measurement of strain, temperature, and loss by exploiting the slope of the BGS. After measuring the strain-, temperature-, and loss-dependence coefficients of the output signal (1.95×10^{-4} dB/με, 4.42×10^{-3} dB/K, and 0.191), we verified the basic operation of simultaneous measurement of the three parameters. The improvement of the low SNR is one of the most important future tasks. Note that the idea of the slope-assisted technique has been already reported to enhance the operating speed of Brillouin optical time-domain systems by other researchers [77, 78]. What we presented in this Chapter can be regarded as the first trial to exploit this idea to develop high-speed correlation-domain systems. From the next Chapter, we will describe some novel functions of SA-BOCDR that have not been obtained in time-domain systems before.

3 Characterization

In this Chapter, we characterize the operation of SA-BOCDR and describe the unique features of the system with an emphasis on a so-called beyond-nominal-resolution effect. First, we theoretically and experimentally investigate the relationship between the system output of SA-BOCDR and the actual BFS distribution along the FUT and show that these two are not identical. Then, we prove that the strained/heated sections even shorter than the nominal resolution can still be detected using SA-BOCDR, which is not the case for standard BOCDR. After characterizing this unique "beyond-nominal-resolution" effect, we show the usefulness of this effect by demonstrating the detection of a 2-mm-long strained section along a silica fiber and a 5-mm-long heated section along a polymer optical fiber POF. The lengths of these detected sections are smaller than those of the other demonstrations reported so far. Next, the influences of the experimental conditions on the measurement sensitivity of SA-BOCDR are investigated. The sensitivity is found to be improved with increasing incident power and/or lowering spatial resolution. Finally, we demonstrate distributed temperature sensing based on SA-BOCDR with a long measurement range of > 10 km. We find that, to achieve such a long-range measurement, a delay line in a reference path needs to be at least 4 times longer than the FUT. Finally, by exploiting a beyond-nominal-resolution effect of the SA-BOCDR, we detect a 3-m-long heated section in a 13-km-long silica fiber in a distributed manner.

3. 1 System output

3. 1. 1 Preface

The proof of concept for SA-BOCDR has been demonstrated in Chapter 2, but its detailed

operation has to be provided. One fundamental issue is the correspondence between the final system output (i.e., power-change distribution) and the actual BFS distribution. In standard BOCDR systems based on frequency information, these two distributions have been proven to be identical, in principle; however, in an SA-BOCDR system based on power information, these two are not identical.

In this section, we theoretically and experimentally show that the final system output of SA-BOCDR is generally different from the actual BFS distribution. When the strained section is sufficiently longer than the nominal spatial resolution, the power-change distribution almost reproduces the actual BFS (or strain) distribution. However, when the strained section is almost equal to or only a few times longer than the nominal resolution, the actual BFS distribution is not directly obtained (further data processing is necessary). We also show that even when the strained section is shorter than the nominal resolution some shift in the power change can be observed. This feature is unique to SA-BOCDR and potentially useful for practical applications.

3. 1. 2 Simulation

To start with, the system output of SA-BOCDR was theoretically investigated. We assumed that the strain was uniformly applied to one section of the FUT and its magnitude was smaller than the upper limit of the linear region (~2000 με). The strained length was assumed to be 0.25*R*, 0.5*R*, 0.75*R*, *R*, 2*R*, 5*R*, and 10*R*, when *R* indicates the nominal spatial resolution of the system. Figure 3.1(a) shows the simulation results in standard BOCDR. The strain distributions were deduced from the BFS information, and we can confirm that the final output completely reproduce the actual BFS distributions. Next, the simulation results for the strain distributions obtained from SA-BOCDR (also deduced from the final power-change distributions simply based on the linear power-to-strain relationship) are shown in Fig. 3.1(b) (strained: 0.5*R*, *R*, 2*R*, 5*R*, and 10*R*) and Fig. 3.1(c) (strained: 0.25*R*, 0.5*R*, 0.75*R*, and *R*). To make the calculation simple, the complicated longitudinal shape of the correlation peak and the influence of its sidelobes [59] were neglected; that is, the longitudinal shape of the correlation peak was approximated by a rectangular profile with a length of *R*. At the ends of the strained section (i.e., the

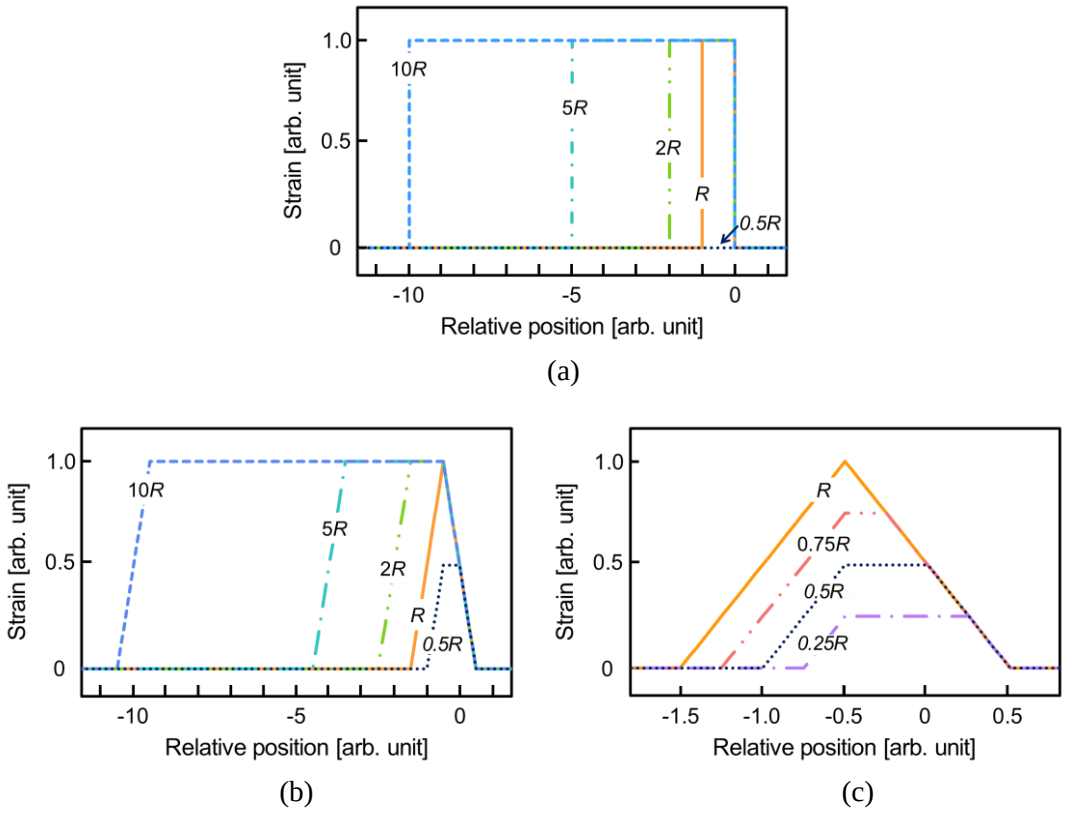

Fig. 3.1 Simulation results (deduced strain distributions directly obtained from power change distributions) of (a) standard BOCDR and (b, c) SA-BOCDR. Note that (a) gives the correct strain distributions.

boundaries between the strained and non-strained sections), the power change varied linearly with the length of *R*; consequently, each whole power-change distribution showed a trapezoidal shape (including triangular). Thus, we see that when the strained section is sufficiently longer than *R*, the power-change distribution almost reproduces the actual BFS distribution. In contrast, when the length of the strained section is approximately *R* or only a few times longer than *R*, the correct BFS distribution cannot be directly obtained (under the assumption that the strain is uniformly applied; however, the correct information can be easily derived). What we should focus here is that we can observe some signal change (trapezoidal-shaped shift in the power change) even when the strained section is shorter than *R*. For instance, when the strained length is 0.5*R*, a trapezoidal shape with a maximal power-change shift corresponding to half the amount seen with a strained section longer than *R* is observed. This "beyond-nominal-resolution" information, which neither standard BOCDR systems nor SA-BOTDR/BOTDA systems

can provide (note that standard BOCDR systems determine the BFS as the frequency at which the highest spectral peak is observed; even when the local Brillouin spectrum includes a low spectral peak corresponding to strain, as long as this peak is lower than the initial spectral peak corresponding to the non-strained sections, it does not contribute to the derived BFS), will be of great use in practical applications. One important benefit is that using this effect, we can effectively elongate the measurement range of BOCDR, which generally suffers from the trade-off relation between the spatial resolution and the measurement range.

3. 1. 3 Experimental setup

Figure 3.2(a) schematically shows the experimental setup of SA-BOCDR for evaluating the simulation results described above. The light output from a 1.55 μm laser was divided into two light beams: pump and reference. The pump beam was guided through a PSCR to suppress the polarization-dependent signal fluctuations, then amplified to ~27 dBm using an EDFA and injected into the FUT. The backscattered Stokes light was amplified to ~2 dBm using another EDFA. The reference beam was guided through a ~1-km-long delay line and amplified to ~1 dBm. The Stokes and the reference beams were then mixed (heterodyned), converted into an electrical signal using a PD, and guided to an ESA. Using the narrow band-pass filtering function of the ESA (with the video bandwidth and resolution bandwidth set to 10 kHz and 10 MHz, respectively), the change in the spectral power at 10.81 GHz was sequentially output to an OSC. An electrical amplifier was not used in this measurement.

As an FUT, we used a 13.0-m-long single-mode silica fiber with a BFS of 10.86 GHz at 1.55 μm at room temperature. Measurements were performed using two configurations: one for a relatively high spatial resolution and the other for a relatively low resolution (required to investigate the beyond-nominal-resolution effect). In the first, high-resolution configuration, strains of 750 με and 1500 με were applied to 5-cm-, 10-cm-, 20-cm-, 50-cm-, and 100-cm-long sections of the FUT, as shown in Fig. 3.2(b). The modulation frequency f_m and amplitude Δf were set to 7.11–7.31 MHz and 1.3 GHz, respectively, corresponding to the measurement range of 14.5 m and the theoretical spatial resolution of 9.5 cm according to Eqs. (1-1) and (1-2). In the second, low-

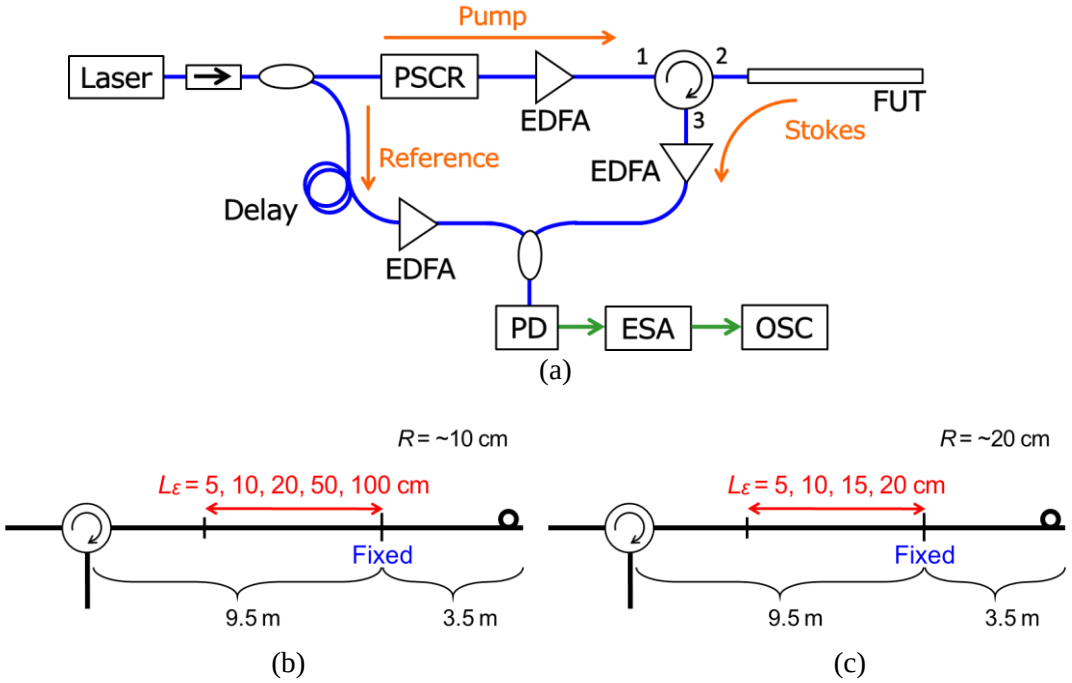

Fig. 3.2 (a) Experimental setup for SA-BOCDR. EDFA, erbium-doped fiber amplifier; ESA, electrical spectrum analyzer; FUT, fiber under test; OSC, oscilloscope; PD, photo diode; PSCR, polarization scrambler. The silica fibers and electrical cables are shown in the blue curves and green lines, respectively. (b) Structure of an FUT when the spatial resolution was relatively high (9.5 cm). (c) Structure of an FUT when the spatial resolution was relatively low (19.6 cm).

resolution configuration, a strain of 1500 με was applied to 5-cm-, 10-cm-, 15-cm-, and 20-cm-long sections of the FUT (see Fig. 3.2(c)). The modulation frequency f_m was swept in the same range (7.11–7.31 MHz), thus giving the same measurement range (14.5 m). The modulation amplitude Δf was reduced to 0.7 GHz, corresponding to a theoretical spatial resolution of 19.6 cm. In both configurations, the repetition rate was set to 100 Hz, and 64 times averaging was performed on the OSC to improve the SNR. The room temperature was 25 °C.

3. 1. 4 Experimental results

First, we present the experimental results with relatively high spatial resolution (9.5 cm). An example of the measured power change distribution (converted into strain) along the whole length of the FUT (with a 1500 με strain applied to a 20-cm-long section) is shown in Fig. 3.3(a). At this scale, it appears that the correct amount of strain was detected at the

correct location. The strain distributions measured when strains of 750 με and 1500 με were applied (magnified views around the strained sections), simply deduced from the power-change distributions based on the linear power-to-strain relationship, are shown in Fig. 3.3(b) and 3.3(c), respectively. Each distribution is shifted by 3000 με, and the simulated data is indicated by dotted lines. The trends in the measured distributions agree well with the simulation results, including the case where the strained section is half the nominal spatial resolution. This indicates that our relatively rough simulation is almost

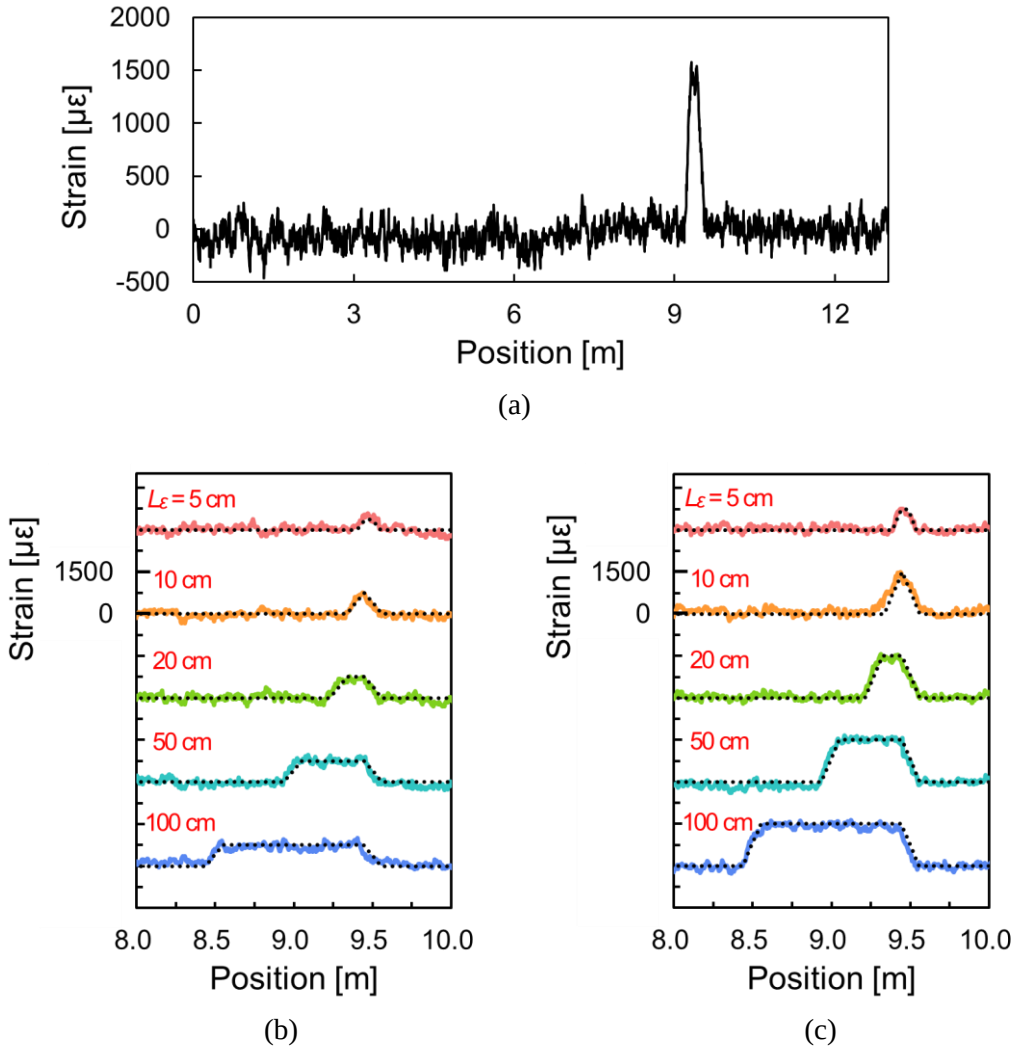

Fig. 3.3 Obtained strain distributions calculated from power change distributions. Note that the spatial resolution was 9.5 cm. (a) Example measurement along a 13-m-long FUT when a 20-cm-long section was strained (1500 με). and the magnified views when strains of (b) 750 με and (c) 1500 με were applied to 5-cm- to 100-cm-long sections. In (b) and (c), the simulated data was shown in dotted lines, and each distribution was shifted by 3000 με.

sufficient to predict the experimental results, which is beneficial from the viewpoint of simulation cost. The discrepancy from the simulation results probably originates from signal fluctuations due to an insufficient SNR and the fact that the influence of the correlation peak sidelobes was not considered in the simulation process.

Subsequently, we performed similar experiments with a relatively low spatial resolution (19.6 cm) to evaluate the beyond-nominal-resolution effect. The magnified views of the strain distributions (simply deduced from the power-change distributions), measured when a strain of 1500 με was applied, are shown in Fig. 3.4. As the strained section becomes shorter, the maximal power-change shift becomes smaller. The trend in the measured distributions is basically in good agreement with the simulation results. As the strained section is shortened further, the signal is buried by the noise. The standard deviation of the noise floor (power fluctuations corresponding to the strain of the non-strained sections) was calculated to be approximately 130 με in this measurement. This amount is theoretically obtained as the maximal strain when the strained section is 1.7 cm, which could be regarded as the shortest detectable length. Note that this value is influenced by various experimental parameters, such as the amount of the actual strain, the number of averaging, the incident power, etc.

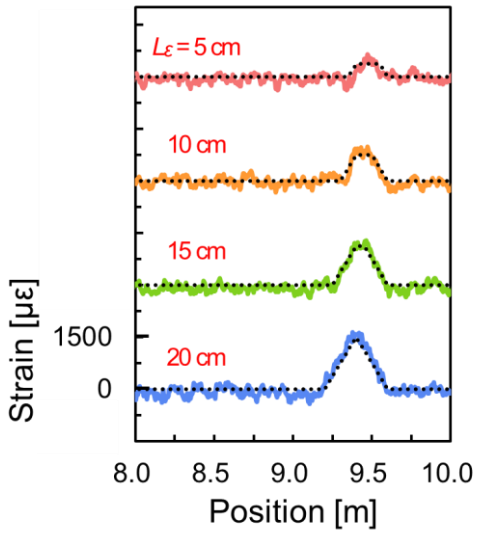

Fig. 3.4 Magnified views of the deduced strain distributions with a spatial resolution of 19.6 cm; a 1500 με strain was applied to 5-cm- to 20-cm-long sections. Each distribution was shifted by 3000 με, and the dotted lines indicate the simulated data.

3. 1. 5 Conclusion

The final system output (i.e., the power-change distribution) of the SA-BOCDR system has been shown, both theoretically and experimentally, not to reproduce the actual BFS (or strain) distribution. When the strained section was sufficiently longer than the nominal spatial resolution, the system output almost corresponded to the actual BFS distribution. In contrast, when the length of the strained section was equal to or only a few times the nominal resolution, the BFS distribution was not reproduced correctly. These findings will be of great importance in improving the performance of SA-BOCDR systems in the future. In addition, we have also demonstrated that a strained section that is even shorter than the nominal resolution can still be detected as a shift in the power change. Beyond-nominal-resolution sensing of temperature change will be also feasible in the same way (cf. the influence of thermal expansion [79] is smaller than the noise floor fluctuations in this measurement). As for loss sensing, as it is point detection, the same effect cannot be observed (not available); in theory, the measured power gradually changes along the length equal to the nominal resolution. We anticipate that this feature, unique to SA-BOCDR, will be an attractive advantage in every application where even slight strain or heat cannot be permitted (regarded as irregular) because of the required high-level constancy, such as nuclear plant monitoring.

3. 2 Beyond-nominal-resolution effect

3. 2. 1 Preface

In previous section, it has been proved that, even when the strained (or heated) section is shorter than the nominal spatial resolution, some shift in the power change can be observed. Although this “beyond-nominal-resolution” effect unique to SA-BOCDR is very attractive for practical applications, the detailed characterization of this feature has not been carried out.

Here, first, we experimentally characterize the beyond-nominal-resolution effect using

a silica SMF. We find that a strained section that is over 50 times shorter than the nominal spatial resolution can be detected. Then, we show the usefulness of the beyond-nominal-resolution effect by detecting a 2-mm-long strained section along a silica SMF and a 5-mm-long heated section along a polymer optical fiber (POF). These values are smaller than the world records previously reported, which are 3 mm [55] and 100 mm [69] for a silica SMF and a POF, respectively (both values were restricted by the SNRs of the systems].

3. 2. 2 Experimental setup

Figure 3.5 shows the experimental setup of SA-BOCDR used in the experiment. A laser diode at 1550 nm with a bandwidth of ~1 MHz was used as a light source. Throughout the experiment in this work, the video and resolution bandwidths of the ESA were set to 3 kHz and 10 MHz, respectively, while the repetition rate was 100 Hz. Note that a PSCR was inserted in the pump path in this setup, but it could be inserted immediately after the laser output before an optical coupler.

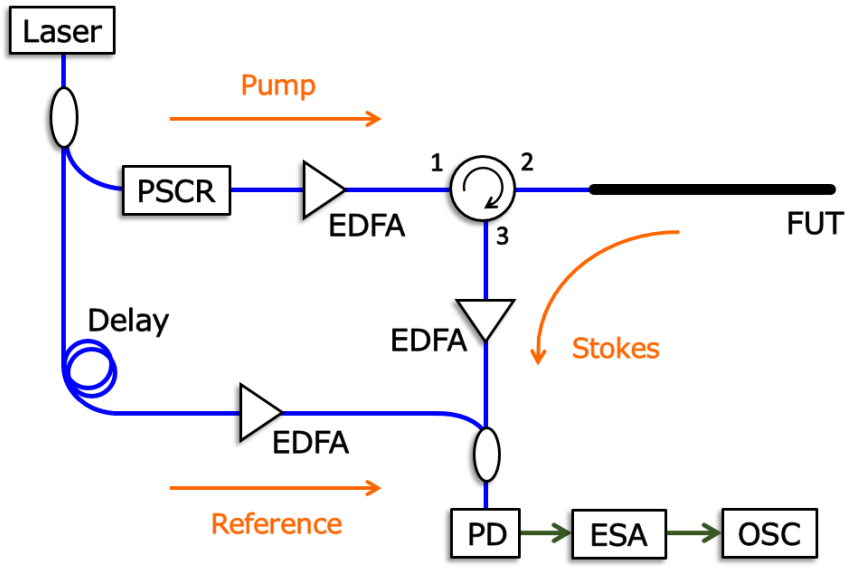

Fig. 3.5 Experimental setup for SA-BOCDR. EDFA, erbium-doped fiber amplifier; ESA, electrical spectrum analyzer; FUT, fiber under test; OSC, oscilloscope; PD, photo diode; PSCR, polarization scrambler.

First, to characterize the beyond-nominal-resolution effect, we employed a 14.0-m-long silica SMF as a FUT. The output light from a laser was amplified to ~25 dBm using an EDFA and injected into the FUT. The BFS of the FUT was 10.89 GHz at 1.55 μm at 26 °C (room temperature). The open end of the FUT was bent to suppress the Fresnel reflection. The spectral power change at 10.87 GHz (determined by differentiating the BGS) was monitored using an OSC. The modulation amplitude Δf and the modulation frequency f_m were set to 0.19 GHz and 5.10–5.26 MHz, respectively, leading to the nominal spatial resolution of 1.01 m and the measurement range of 20.1 m, calculated using Eqs. (1-1) and (1-2). A strain of 0.1% was applied to 0.01-, 0.02-, 0.05-, 0.10-, 0.20-, 0.50-, and 1.00-m-long sections of the FUT, as shown in Fig. 3.6(a). When the length of the strained section was changed, the position of its proximal end was fixed. Averaging was performed 512 times on the OSC to obtain a higher SNR. The number of sampling points was 2500.

Subsequently, exploiting the beyond-nominal-resolution effect, we attempted to detect the shortest-ever strained and heated sections along a silica SMF and a POF. In this experiment, we injected ~28 dBm light to the FUTs to enhance the measurement sensitivity (See Chapter 3.3 for further explanation), and averaging was performed 1024 times. The number of sampling points was 2500. To begin with, as an FUT, we employed a 2.0-m-long silica SMF, the BFS of which was 10.85 GHz at room temperature. We applied strains of 0.10, 0.15, and 0.20% to a 2-mm-long section (fixed on translation stages using epoxy glue; ~55 times shorter than the nominal spatial resolution; see below), as depicted in Fig. 3.6(b). The nominal spatial resolution and the measurement range were 0.11 and 7.64 m (modulation amplitude Δf: 0.67 GHz; modulation frequency f_m: 13.45–13.54 MHz), respectively. The change in the spectral power at 10.84 GHz was observed using the OSC. Then, a 2.0-m-long perfluorinated graded-index (PFGI-) POF [80] (core diameter: 50 μm; propagation loss at 1.55 μm: 0.25 dB/m; BFS at room temperature: 2.75 GHz) was used as an FUT. A 5-mm-long section was heated to 35, 45, and 55 °C [See Fig. 3.6(c)]. The modulation amplitude Δf and the modulation frequency f_m were set to 0.69 GHz and 24.70–24.84 MHz, respectively, resulting in the nominal spatial resolution of 0.21 m and the measurement range of 4.5 m [62]. Note that the length of the heated section was over 40 times smaller than the nominal spatial resolution. The change in the spectral power at 2.78 GHz was monitored.

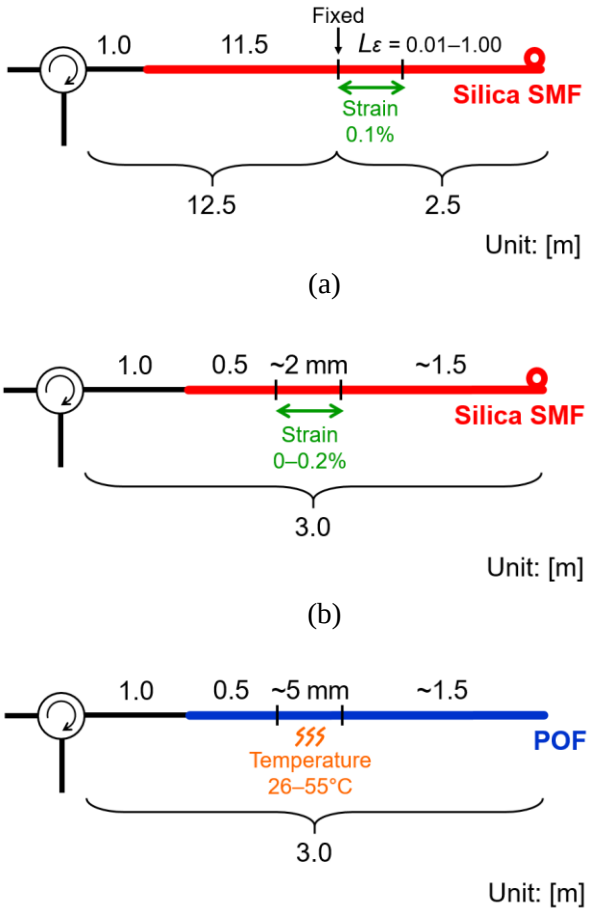

Fig. 3.6 (a) Structure of the FUT (silica SMF). The strained length L_ε was set to 0.01, 0.02, 0.05, 0.10, 0.20, 0.50, and 1.00 m, while keeping the spatial resolution at 1.01 m.(b) Structure of the FUT (silica SMF), which was locally strained for 0, 0.10, 0.15, and 0.20%. (c) Structure of the FUT (POF), which was locally heated to 26, 35, 45, and 55 °C.

3. 2. 3 Experimental results

Figure 3.7(a) shows the measured power-change distributions when the strained length L_ε was reduced from 1.00 to 0.01 m, while keeping the nominal spatial resolution at 1.01 m throughout the experiments. The vertical axis was normalized so that the maximal power change became 1 when L_ε was 1.00 m. Each distribution was shifted by 0.5 in vertical ways. The power-change distribution showed a triangular shape, only when L_ε was 1.00 m (almost same as the spatial resolution),which is natural considering the operating

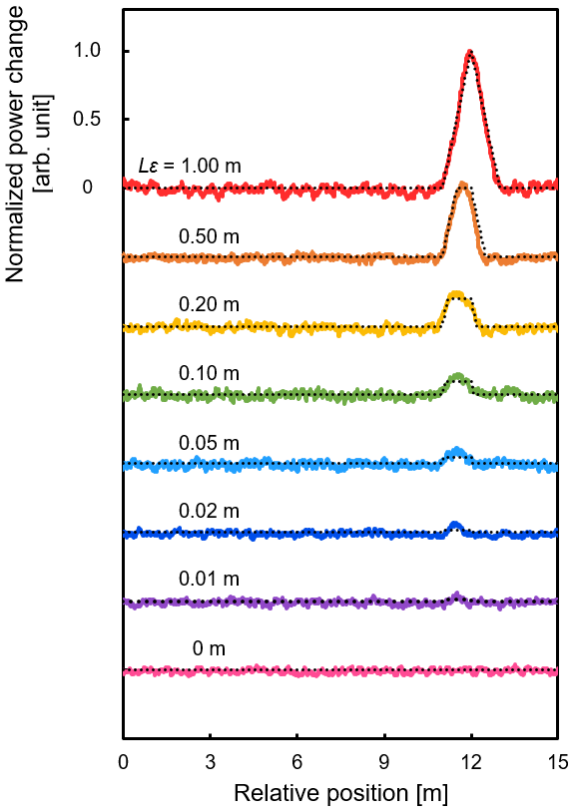

(a)

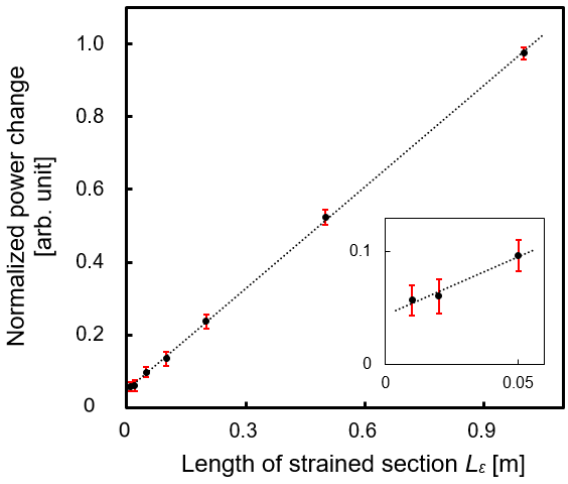

(b)

Fig. 3.7 (a) Normalized power-change distributions measured when the length of the strained section L_ε was reduced from 1.00 to 0.01 m; each distribution was shifted by 0.5. The dotted lines indicate the theoretical trends. (b) Maximal power changes plotted as a function of L_ε. The error bars are calculated as standard deviations of the signal fluctuations at nonstrained sections. The dotted line is a linear fit. The inset shows the magnified view at L_ε shorter than 0.1 m.

mechanism of SA-BOCDR (See Chapter 3.1). As L_ε decreased, the maximal power change also decreased. When L_ε was 0.02 m, the power change was still clearly detected, however, when L_ε was shorter than 0.02 m, it became difficult graph the power change due to the signal fluctuations (calculated standard deviation: 0.06). Accordingly, a strained section at least 50 times shorter than the nominal spatial resolution was shown to be detectable under this experimental condition. The normalized maximal power change was then plotted as a function of L_ε in Fig. 3.7(b). The error bars were standard deviations of the signal fluctuations at nonstrained sections. The maximal power change decreased almost linearly with decreasing L_ε, which agrees well with the theory. The observed

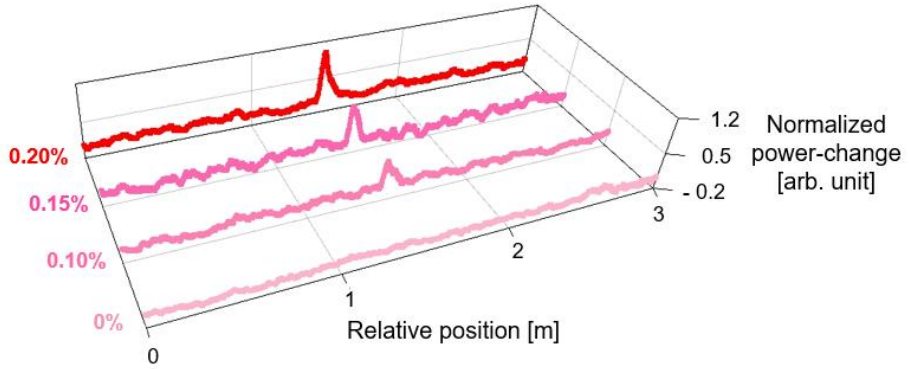

(a)

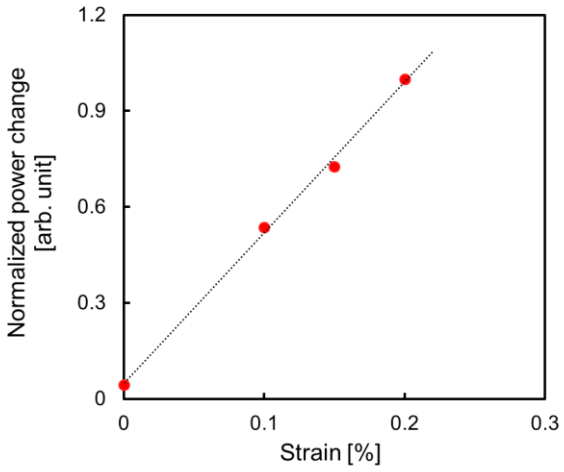

(b)

Fig. 3.8 (a) Normalized power-change distributions along a silica SMF measured at four strains. Each distribution was shifted by 1. (b) Maximal power changes plotted as a function of strain. The dotted line is a linear fit.

length of the nonzero-power-change section was almost equal to the sum of the strained length L_ε and the nominal spatial resolution, which also agrees with the theory (quantitative evaluation is difficult because of the low SNR when L_ε is short).

Subsequently, using the "beyond-nominal-resolution" effect verified above, we tried to detect the shortest-ever hotspots both in a silica SMF and a POF. Figure 3.8(a) shows the normalized power-change distributions measured when strains of 0.10, 0.15, and 0.20% were applied to a 2-mm-long section of the silica SMF. At the correct position, the local power changes corresponding to the strain were observed. The lengths of the power-

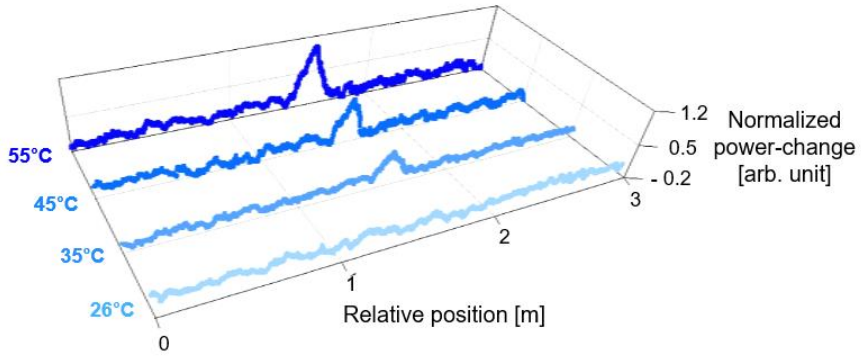

(a)

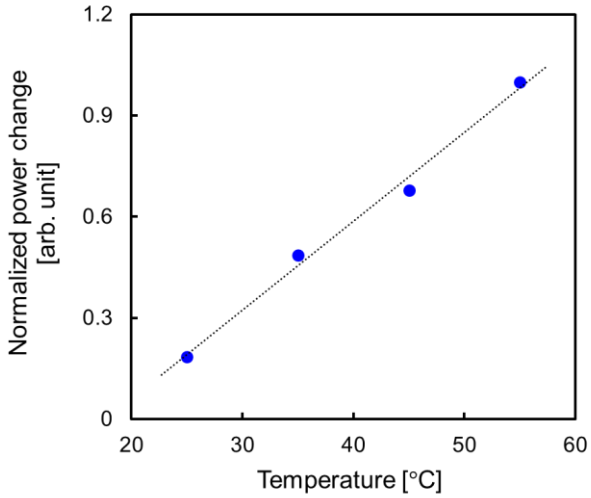

(b)

Fig. 3.9 (a) Normalized power-change distributions along a POF measured at four temperatures. Each distribution was shifted by 1. (b) Maximal power changes plotted as a function of temperature. The dotted line is a linear fit.

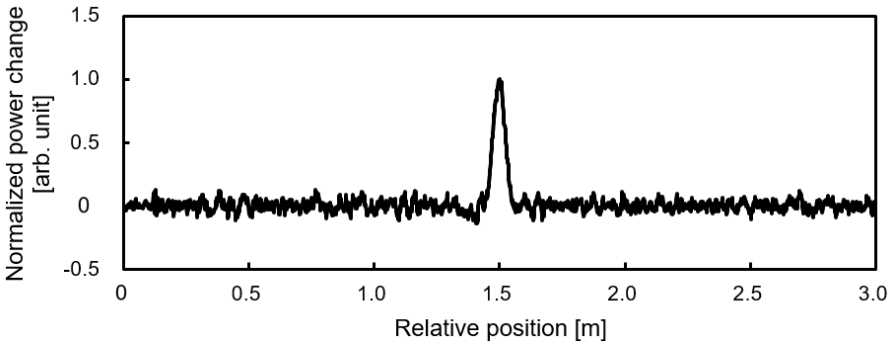

Fig. 3.10 Normalized power-change distribution along a silica SMF. A 2-mm-long silica SMF with different BFS was, as pseudostrain, spliced between two silica SMFs.

changed sections appeared to be much larger than 2 mm; in theory, they should be almost the same as the nominal resolution (0.11 m), which moderately agrees with the measured results. The maximal normalized power change of each distribution in Fig. 3.8(a) was plotted as a function of applied strain in Fig. 3.8(b). With increasing strain, the power-change also increased almost linearly, which indicates that the magnitude of the strain can be correctly measured in this strain range. Then, we performed a similar experiment using the POF. The normalized power-change distributions measured when the 5-mm-long section was heated to 26 (room temperature), 35, 45, and 55 °C are shown in Fig. 3.9(a). The abrupt power changes were observed at the correct position along the POF. The lengths of the power-changed sections moderately agreed with the nominal resolution (0.21 m). The magnitude of the maximal power change was proportional to the temperature change as shown in Fig. 3.9(b), indicating the potential feasibility of distributed temperature sensing.

3. 2. 4 Discussions

Hereafter, we discuss the unique features of the beyond-nominal-resolution effect of SA-BOCDR in detail. The first discussion is regarding the measurement capability of the location, length, and magnitude of applied strain, when the strain is shorter than the nominal spatial resolution. The strain location can be derived from the system output as

the center of the nonzero-power-change section, and the strained length can be given by subtracting the nominal spatial resolution from the length of the nonzero-power-change section, as already described. The strain magnitude can also be given by the maximal power change and the ratio of the strained length to the nominal spatial resolution. Thus, if the SNR of the system is sufficiently high, these three parameters of strain can be theoretically obtained from the measured power-change distribution, although the SNR may not be sufficiently high in most practical cases.

Next, we discuss the validity of claiming that the 2-mm-long strained SMF section and the 5-mm-long heated POF section were detected. When a 2-mm-long strain was applied to the SMF using epoxy glue, unintended strain distribution was inevitably induced along the SMF inside the glue. This may result in a practically longer strain to be measured. To avoid this effect and to prove that the 2-mm-long strain was truly detected, we performed an additional experiment. By splicing a 2-mm-long SMF with a different BFS (11.02 GHz at room temperature), we induced pseudostrain with a length of exactly 2 mm and measured the power-change distribution [the other experimental conditions were the same as those used in Fig. 3.8(a)]. The result shown in Fig. 3.10 clearly indicates that the 2-mm-long pseudostrain was truly detected. As for the temperature measurement, it is difficult to completely avoid the influence of the thermal conduction, and the detected heated section may be slightly longer than 5 mm; however, the conclusion that this system has the capability to detect a 2-mm-long section with a different BFS remains true.

The third discussion is regarding the limitation of the detectable strained length. In this experiment, it was restricted to 2 mm because of the deteriorated SNR. Therefore, the limitation could be enhanced by improving the SNR by using higher-power incident light or by applying a larger strain. For instance, in Fig. 3.8(a), a clear peak (which can be discriminated from the noise floor even when the power-change becomes half) was observed at 0.2% strain; this may indicate that strain with a length of less than half of 2 mm, namely of submillimeter length, can be potentially detected by SA-BOCDR.

Lastly, we discuss the possibility of employing this technique in other types of Brillouin sensors. We consider that the beyond-nominal-resolution effect can also be given to BOCDA systems, because they work on a similar principle of BOCDR (the final system output of BOCDA can be expressed by the same mathematical forms as that of

BOCDR). As BOCDA exploits stimulated Brillouin scattering, which is much larger than spontaneous scattering, we predict that the beyond-nominal-resolution effect of SA-BOCDA will have higher performance than SA-BOCDR and deserve developing in the future, despite its shortcomings in terms of the two-end-access nature and the complexity of the setup.

3. 2. 5 Conclusion

First, we experimentally characterized the "beyond-nominal-resolution" effect of SA-BOCDR using the silica SMF. When the nominal spatial resolution was constant, the measured maximal power change decreased almost linearly with decreasing length of the strained section. Even when the strained length was over 50 times shorter than the nominal spatial resolution, power change was still clearly observed at the correct position. Subsequently, by exploiting this effect, we demonstrated detection of the 2-mm-long strained section in the silica SMF and a 5-mm-long heated section in the POF. In both cases, the power-change distributions at four different strains and temperatures were measured, and the maximal power changes at each distribution increased almost linearly with increasing strain and temperature. These results indicate that, even when the strained (or heated) section is much shorter than the nominal spatial resolution, if the SNR is sufficiently high, its length and the magnitude of the applied strain (or temperature change) can be potentially calculated from the measured power-change distribution. Thus, we anticipate that this work, which has proven the capability of detecting extremely short strained/heated sections along optical fibers, will greatly enhance the practical applicability of SA-BOCDR in the near future.

3. 3 Sensitivity dependencies on experimental conditions

3. 3. 1 Preface

Since SA-BOCDR operates by exploiting the spectral power of the BGS, unlike in the

case of standard BOCDR, the measurement sensitivity of SA-BOCDR is susceptible to the experimental conditions, such as incident power and spatial resolution, which determines the Brillouin signal power.

In this work, first, by analyzing the BGS shape, we investigate the measurement sensitivity dependencies on the incident power and the spatial resolution in SA-BOCDR. We show that the sensitivity is enhanced with higher incident power and/or lower spatial resolution. Then, this result is verified through distributed temperature measurements.

3. 3. 2 Experimental setup

In the experiment, we employed a 3.0-m-long silica SMF as an FUT. The experimental setup depicted in Fig. 3.11 is basically the same as that previously used. The output from a 1.55 μm laser (3 dB bandwidth: ~1 MHz, power: 4 dBm) was divided into two light beams, pump and reference. The incident power to the FUT was changed by adjusting the output power of an EDFA in the pump path. The backscattered Stokes light was amplified to ~1 dBm using another EDFA and heterodyned with the reference light, which was amplified to ~3 dBm after passing through a 1-km-long delay line (used to control the order of the correlation peak generated in the FUT). The heterodyned signal was

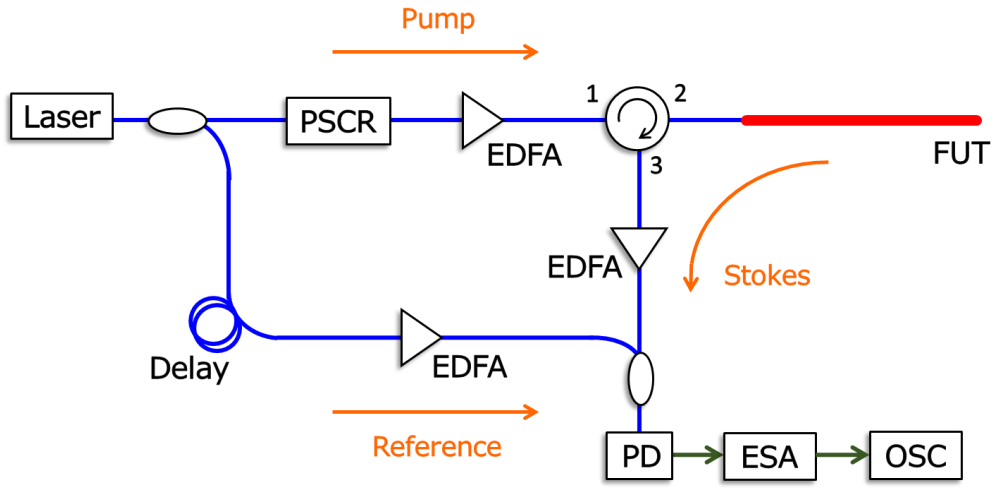

Fig. 3.11 Experimental setup for SA-BOCDR. EDFA, erbium-doped fiber amplifier; ESA, electrical spectrum analyzer; FUT, fiber under test; OSC, oscilloscope; PD, photo diode; PSCR, polarization scrambler.

converted to an electrical signal using a PD. The polarization state was scrambled to suppress the polarization-dependent signal fluctuations. The video bandwidth and the resolution bandwidth of the ESA were set to 10 kHz and 10 MHz, respectively.

The modulation frequency f_m and amplitude Δf were set to 10.858 MHz (swept from 10.825 to 10.891 MHz for distributed measurement) and 0.06–3.08 GHz, respectively, corresponding to a measurement range of ~9.5 m and a theoretical spatial resolution of 1.65–0.03 m according to Eqs. (1-1) and (1-2). For each measurement, ν_{B0} was adjusted to maximize the linear range (i.e., strain/temperature dynamic range) by differentiating the spectral slope; see Chapter 2 for the details. The repetition rate was set to 100 Hz, and 128 times averaging was performed on the oscilloscope to obtain a sufficiently high SNR. The room temperature was 21°C.

3. 3. 3 Experimental results

First, to clarify the measurement sensitivity (defined as a spectral slope at ν_{B0}) at each incident power and spatial resolution, we obtained the BGS at incident powers from 9 to 27 dBm (step: 3 dB), while the spatial resolution was simultaneously varied in the range from 0.03 to 1.65 m. Examples of the BGS measured at 15 and 24 dBm are shown in Figs. 3.12(a) and (b), respectively. In both cases, the BGS gradually became weaker and broader as the spatial resolution grew higher (the value itself became smaller), which leads to the reduction in its spectral slope. Here, the reduction in the peak power is natural if we simply consider that the Brillouin signal returns only from the fiber section roughly equal to the spatial resolution. The broadening of the bandwidth caused by the frequency modulation has also been reported. Note that, in Fig. 3.12(b), when the spatial resolution was 1.65 m, an irregular peak was observed at ~11.1 GHz. This peak, which originated from the 2nd-order Brillouin peak [81], immediately disappeared by increasing modulation amplitude and did not influence the results of this measurement.

We then precisely analyzed the spectral slopes of each BGS and investigated the measurement sensitivity dependence on the spatial resolution. Here, the values of the optimal fixed frequency ν_{B0} (at which the slope power is measured) and the bandwidth of the linear region w_L (which is evaluated by differentiating the spectral slope; see Chapter

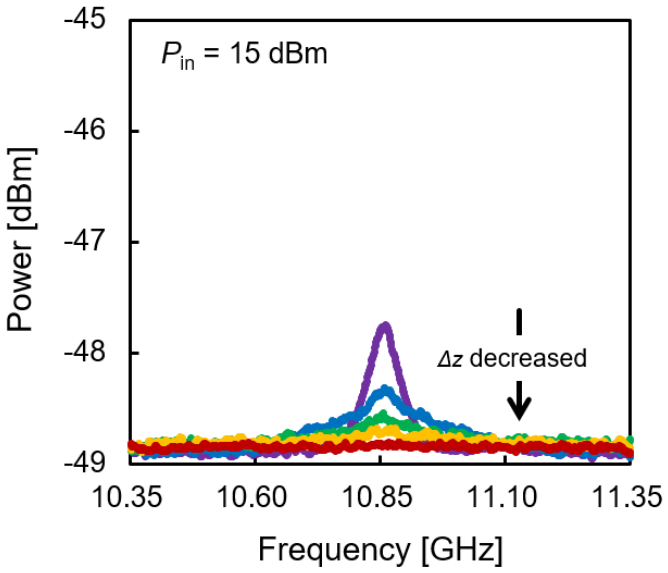

(a)

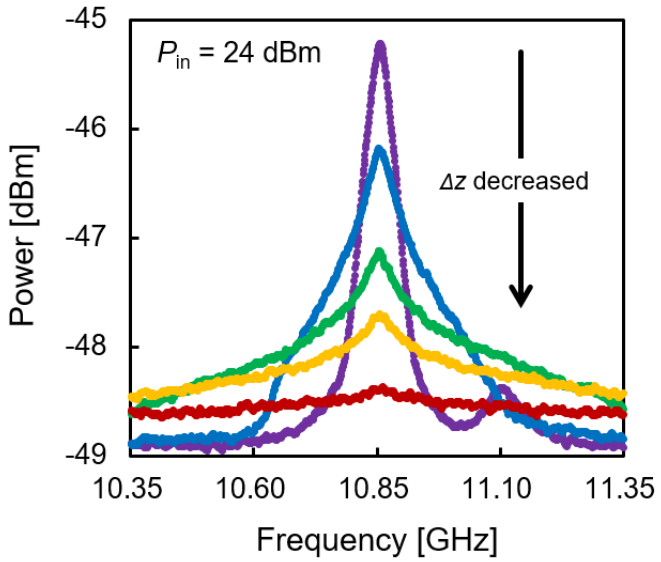

(b)

Fig. 3.12 Examples of the BGS when the spatial resolution Δz was 1.65 (purple), 0.43 (aqua), 0.18 (green), 0.09 (yellow), and 0.03 m (red). (a) Measured at 15-dBm incident power. (b) Measured at 24-dBm incident power.

2 for its detailed definition) were calculated for each BGS. For instance, when the incident power was 24 dBm and the spatial resolution was 1.65 m, ν_{B0} was set to 10.83 GHz and w_L was approximately 50 MHz (10.78–10.83 GHz). Fig. 3.13 shows the measurement sensitivities plotted as functions of the spatial resolution at seven different incident

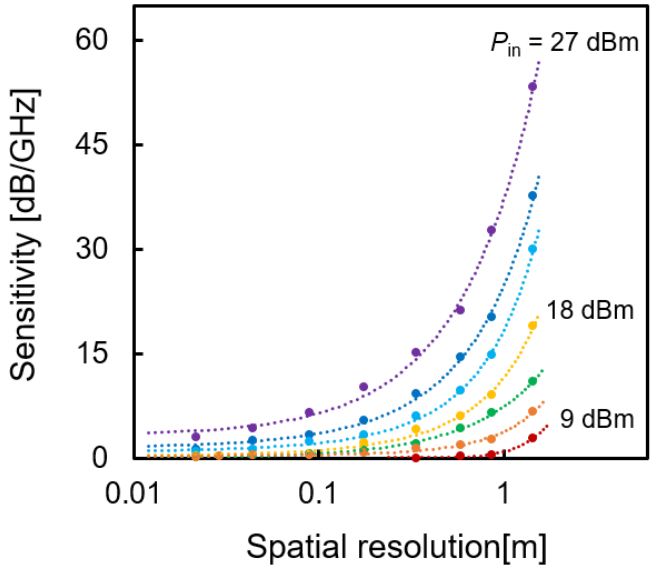

Fig. 3.13 Measurement sensitivities plotted as functions of the spatial resolution at incident powers from 9 to 27 dBm (step: 3 dB).

powers. Regardless of the incident power, the measurement sensitivity decreased and finally converged to 0 dB/GHz as the spatial resolution grew higher (the value of the resolution itself grew smaller). At 9-dBm incident power, it was difficult to calculate the BGS slopes when the spatial resolution was lower than ~0.3 m, because the BGS was buried by the noise. Note that, as Brillouin-scattered power does not generally increase in proportion to increasing incident power [10], we did not normalize the plots in Fig. 3.13. Note also that, though the temperature dynamic range seems to be dependent on incident power and spatial resolution as well, it cannot be simply evaluated by the range of the linear region because of the structural noise floor unique to correlation-domain techniques [82].

Subsequently, we performed distributed temperature measurements to verify that the results shown in Fig. 3.13 (indirectly acquired based on the analysis of the BGS slope) can be practically employed. The structure of the FUT is depicted in the inset of Fig. 3.14. While maintaining the temperature of a 0.30-m-long section (1.7 m away from the proximal FUT end) at 60°C using a heater, the power-change distributions along the FUT were obtained under the following four experimental conditions: (incident power P_{in}, spatial resolution Δz) = (15 dBm, 0.09 m), (15 dBm, 0.18 m), (24 dBm, 0.09 m), and (24

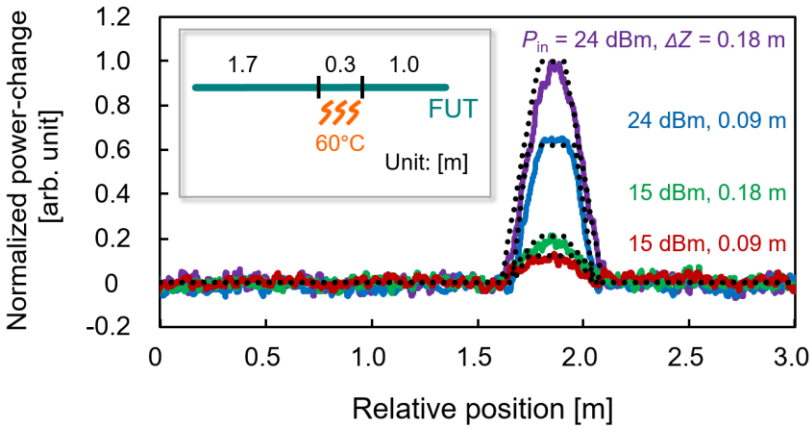

Fig. 3.14 Normalized power-change distributions along the FUT measured at four experimental conditions. The solid curves are measured data, and the dotted curves are calculated trends. The inset indicates the structure of the FUT.

dBm, 0.18 m). Fig. 3.14 shows the power-change distributions; the vertical axis was normalized so that the maximal value became 1 when (P_{in}, Δz) = (24 dBm, 0.18 m). Note that the proportions among the four data on the vertical axis were maintained. The maximal value of each data were in good agreement with the trends (shown as dotted curves in Fig. 3.13) calculated using Fig. 3.13. Note that, in the calculation, the shape of the correlation peak was assumed to be a rectangle (see Chapter 3.1.2), which is not accurate. The discrepancy between the measured data and the calculated trends seems to be partially caused by this assumption. For each power-change distribution, we measured the standard deviation of the noise floor (signal fluctuations of the non-heated sections). Under the four experimental conditions: (P_{in}, Δz) = (15 dBm, 0.09 m), (15 dBm, 0.18 m), (24 dBm, 0.09 m), and (24 dBm, 0.18 m), the standard deviations (unit: °C) were calculated to be approximately 4.8, 3.3, 1.2, and 0.9°C, respectively. The sensing error decreased with increasing measurement sensitivity (increasing incident power and/or lowering spatial resolution). Note that these values are also affected by other experimental parameters, such as the measurement speed, the number of averaging, etc. Thus, higher-power light was confirmed to be required to enhance the measurement sensitivity as well as the signal-to-noise ratio. However, injection of extremely high-power light sometimes induces a so-called optical fiber fuse phenomenon, which destroys the FUT [83–85]. Consequently, the optimal incident power will be approximately 25 dBm, which should be increased or decreased considering the actual situations.

3. 3. 4 Conclusion

Based on the analysis of the BGS shape, we investigated the measurement sensitivity dependencies on the incident power and the spatial resolution in SA-BOCDR. The sensitivity decreased and then converged to 0 dB/GHz as the incident power decreased and/or the spatial resolution grew higher. Then, we verified this result through distributed temperature measurements. Thus, we believe that this work will provide a useful guideline in setting the experimental conditions of SA-BOCDR and then in achieving single-end-access high-speed distributed sensing with high spatial resolution in the future.

3. 4 Long-range measurement

3. 4. 1 Preface

Considering practical applications, SA-BOCDR with a long measurement range needs to be demonstrated. However, most of the previously reported demonstrations of SA-BOCDR and even standard BOCDR had measurement rages shorter than ~1.5 km [65] (Only one exception is referred to in Conclusion).

In this work, the operation of SA-BOCDR with a long measurement range of > 10 km is demonstrated. First, we show that a delay line in a reference path should be at least 4 times longer than the sensing fiber to achieve such a long measurement range. We also show that the use of such a long delay line inevitably accompanies forward-propagating Brillouin-scattered light in the reference path, which leads to a deteriorated SNR and thus should be filtered out. Then, based on the beyond-nominal-resolution effect, we demonstrate the detection of a 3-m-long heated section in a 13-km-long FUT. We also discuss the reason for the low SNR of the long-range measurement.

3. 4. 2 Experimental setup

The experimental setup of SA-BOCDR with a long measurement range is depicted in

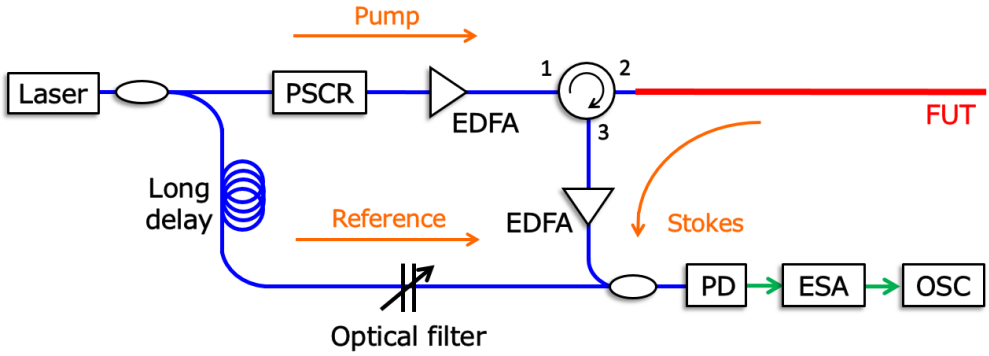

(a)

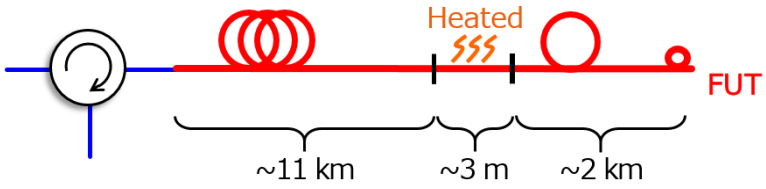

(b)

Fig. 3.15 (a) Setup of SA-BOCDR with a long measurement range. EDFA, erbium-doped fiber amplifier; ESA, electrical spectrum analyzer; FUT, fiber under test; OSC, oscilloscope; PD, photo diode; PSCR, polarization scrambler. (b) Structure of the FUT.

Fig. 3.15(a). The output from a frequency-modulated laser (linewidth: ~1 MHz) was divided into pump light and reference light. The pump light was amplified to 10 dBm using an EDFA and injected into a 13-km-long FUT (see below for details). The polarization state was scrambled. Here, it is notable that the incident power should not be too high, because the Brillouin threshold power of a long FUT is generally low and, even when the frequency is modulated, most of the high-power incident light does not reach the end of the FUT by stimulated Brillouin scattering [24]. What is also unique to long-range measurement is the structure of the reference path; unlike in standard BOCDR, a long delay line and an optical narrowband-pass filter (3-dB bandwidth: ~10 GHz) were employed. One of the new findings is that the length of the delay line should be at least 4 times longer than the FUT. In this experiment, a 60-km-long delay line was employed; otherwise, the 1st-order correlation peak cannot be scanned along the entire length of the FUT (the use of a higher-order correlation peak requires an even longer delay line, which

is not ideal considering its cost and propagation loss). Another finding is that, when the delay line is extremely long, in addition to the carrier at laser frequency, forward-propagating Brillouin-scattered light, both Stokes and anti-Stokes, is induced and appears as sidebands in the optical spectrum. This results from the back reflection of spontaneous Brillouin scattered components, etc. These unintended Brillouin components in the reference path cause considerable noise in the final system output if they interfere with the Rayleigh-scattered light from the FUT. Therefore, the optical filter was newly employed in the reference path to suppress the Brillouin components. The Brillouin-scattered light was amplified and heterodyned with the reference light. Then it was converted into an electrical signal using a PD; its spectral power at 10.87 GHz (on the BGS slope) was output using a zero-span mode of an ESA and monitored using an OSC. The video bandwidth and the resolution bandwidth of the ESA were 10 kHz and 10 MHz, respectively. Averaging was performed 128 times on the OSC.

The structure of the FUT is depicted in Fig. 3.15(b). A 13-km-long silica single-mode fiber (SMF; BFS = 10.88 GHz) was employed as an FUT, and a considerable bending loss was artificially applied near its end to suppress the Fresnel reflection. A 3-m-long section (11 km far from the proximal end) was heated from room temperature (23°C) to 70°C. The modulation amplitude was 5 GHz, and the modulation frequency was swept from 4.51 kHz to 7.07 kHz, corresponding to the measurement range of 14.5 km and the nominal spatial resolution from 26.7 m to 41.9 m [62]. Note that the variation of the resolution according to the measurement position is striking when the FUT is extremely long.

3. 4. 3 Experimental results

The normalized power-change distributions near the heated section (23°C, 50°C, and 70°C) are shown in Fig. 3.16(a). Clear peaks were observed at the heated section. The shape of the waveforms at the heated section is not rectangular, which is valid considering the nature of SA-BOCDR (see Chapter 3.1 for details). It is also valid that the peaks were broadened because the nominal spatial resolution at this position is 28.2 m. The SNR was not high in this long-range measurement, because (1) the incident power was much lower than those of shorter-range measurement, (2) the weak incident power was reduced

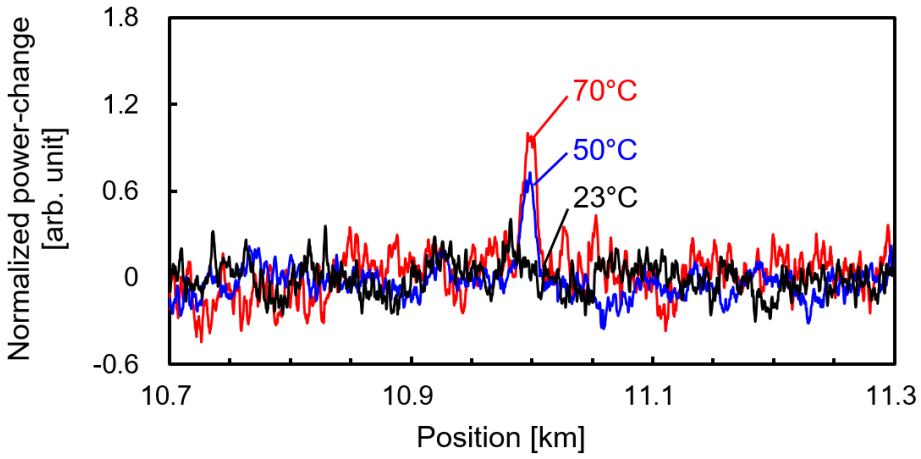

(a)

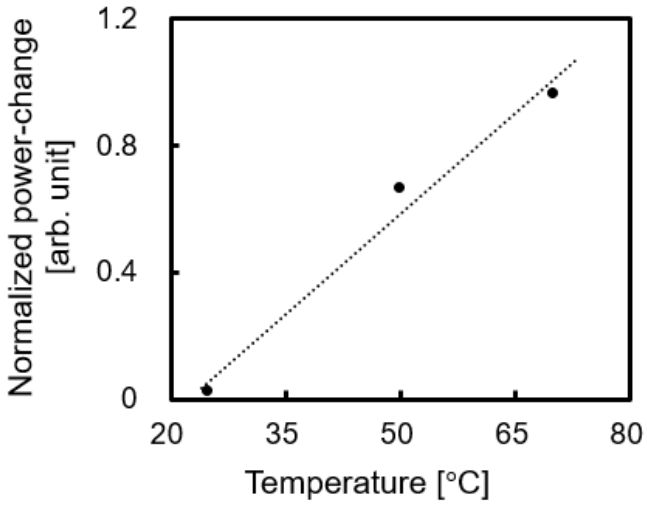

(b)

Fig. 3.16 Measured results. (a) Power-change distributions near the 3-m-long heated section. (b) Maximal power-change plotted as a function of temperature. The dotted line is a linear fit.

further during propagation of the long FUT, (3) the measurement position is far beyond the coherence length of the laser (~100 m) [86], and (4) the aforementioned noise caused by the Brillouin components in the reference path cannot be completely suppressed. Subsequently, we plotted the maximal power-change at the heated section as a function of temperature (Fig. 3.16(b)). The dependence was almost linear, indicating that, although the SNR was low, a 3-m-long heated section was properly detected at a >10 km distant position.

3. 4. 4 Conclusion

We demonstrated the operation of SA-BOCDR with a >10 km measurement range. The experimental setup needed to be modified from a standard short-range setup. We found that a delay line of at least 4 times the length of the FUT should be inserted in the reference path. We also showed that the long delay line induces forward-propagating Brillouin-scattered light in the reference path, and that it should be filtered out to avoid the deterioration of the SNR. Finally, based on the beyond-nominal-resolution effect, a 3-m-long heated section in a 13-km-long FUT was detected. We discussed four reasons why the SNR was relatively low in this measurement.

Although there is a report that BOCDR with such a long measurement range properly operated [86], the temporal gating scheme was employed to extend the measurement range [64] and, in that case, a long delay line did not need to be used. Unlike this report, our study is useful on the point that the influences of the long delay line on the performance of BOCDR have been investigated for the first time to the best of our knowledge.

4 Performance improvement

In this Chapter, some studies are carried out to improve the performance of SA-BOCDR, such as stability, sensitivity, strain dynamic range, and the robustness. First, we verify the loss-insensitive operation of SA-BOCDR by using a special silica SMF. Following the fundamental characterizations, by comparing the distributed strain and temperature measurement results using the standard fiber and the special fiber, we prove the effectiveness of this loss-insensitively configured slope-assisted BOCDR. Then, we develop polarization-scrambling-free SA-BOCDR and evaluate the performance of this scheme. After showing that this system can operate with higher stability even when the PSCR is switched off, we investigate the fundamental sensing properties. We also show that the measurement sensitivity of the scheme is 1.4 times higher than the conventional value. Next, we try to enhance the strain dynamic range of SA-BOCDR, which has been limited to approximately 0.15%. We clarify that, unlike widely used time-domain techniques, SA-BOCDR has a trade-off relation between the strain dynamic range and the spatial resolution. This trade-off originates from the unique bell-shaped noise floor inherently involved in the BGS observed with correlation-domain techniques. We experimentally show that, at the cost of 3 times lowered spatial resolution, the strain dynamic range of >0.6% can be achieved. Finally, we investigate the influence of the use of a high-loss polymer optical fiber (POF) on SA-BOCDR, which enhance the robustness, temperature sensitivity, and maximal detectable strain. Due to the gradual reduction in the transmitted power along the POF, the measurement sensitivities are found to depend on sensing position, unlike the case of standard silica fiber-based configurations. This unique effect is investigated experimentally, and then a correct POF-based distributed measurement is performed by compensating this effect.

4. 1 Stability

4. 1. 1 Preface

SA-BOCDR has the detection capability of not only strain and temperature but also locally applied loss. This feature is sometimes beneficial to practical applications, but from the viewpoint of stable measurement, the influence of unintendedly applied losses should be minimized.

In this section, we demonstrate loss-insensitive operation of SA-BOCDR by employing a special silica fiber with low bending loss. We characterize the sensing performance of the loss-insensitive SA-BOCDR and find that the coefficients of the power-change dependencies on strain and temperature are 1.42×10^{-4} dB/με and 3.28×10^{-3} dB/K, respectively (when the spatial resolution is 144 mm and the measurement range is 14.7 m). Subsequently, by comparing the distributed strain and temperature measurement results using a standard silica fiber and the special fiber, we show that this configuration offers highly stable loss-insensitive operation for practical use in the future.

4. 1. 2 Experimental setup

Figure 4.1 shows the experimental setup of SA-BOCDR, which is basically the same as that previously used. The pump light was amplified to ~26 dBm using an erbium-doped fiber amplifier and injected into the FUT. The reference light was passed through a ~1-km-long delay fiber, amplified to ~2 dBm, and coupled with the Brillouin-scattered light (amplified to ~1 dBm) for heterodyne detection. By inserting a polarization scrambler in the pump path, the polarization-dependent signal fluctuations were suppressed to improve the SNR. The heterodyned optical signal was converted into an electrical signal with a photodiode, amplified by 23 dB using an electrical amplifier, and observed with an ESA (video bandwidth: 3 kHz, resolution bandwidth: 10 MHz) as a BGS. Exploiting the narrow band-pass filtering function of the ESA, the power change at a fixed frequency (= 10.81 GHz; calculated by analyzing the measured BGS, as

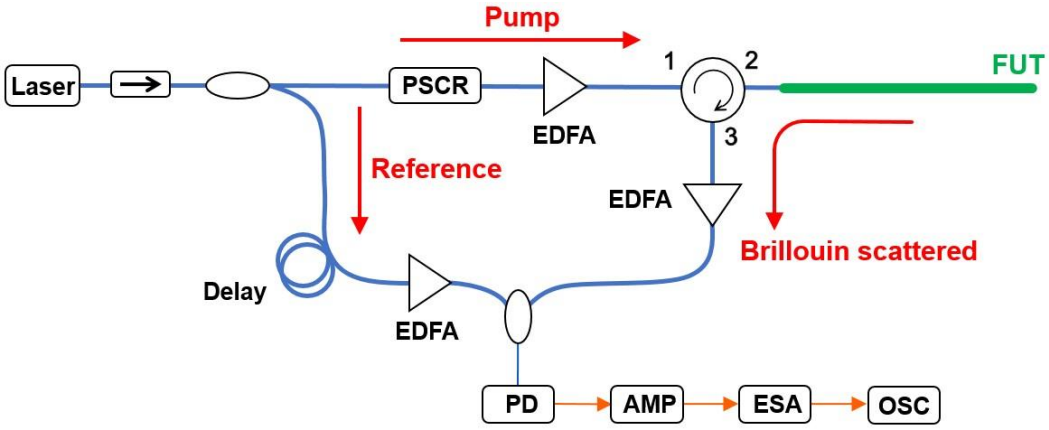

Fig. 4.1 Schematic of the SA-BOCDR setup. AMP, electrical amplifier; EDFA, erbium-doped fiber amplifier; ESA, electrical spectrum analyzer; OSC, oscilloscope; PD, photo diode; PSCR, polarization scrambler. 梶川

mentioned below) on the BGS slope was sequentially output to an oscilloscope, on which averaging was performed 1024 times. The modulation amplitude Δf was set to 1.3 GHz. For distributed measurements, the modulation frequency f_m was swept from 6.91 to 7.10 MHz (note that, in a single-point measurement for characterizing the system performance, f_m was fixed at 7.04 MHz, which corresponds to the location of the correlation peak 7.9 m away from the circulator). According to Eqs. (1-1) and (1-2), these conditions resulted in the nominal spatial resolution of 144 mm and the measurement range of 14.7 m. The room temperature was 21 °C.

The low-bending-loss silica fiber used in the experiment was a 12.0-m-long trench-index-type SMF (FutureGuide-BIS-B, Fujikura [88, 89]) with a low bending loss (e.g., 0.018 dB/turn at 1550 nm for a bending radius of 7.5 mm). One end of this special fiber was connected to the 1.0-m-long pigtail of the second port of an optical circulator via an "FC/APC" adaptor, and the other end was cut with an angle and immersed into index matching oil to suppress the Fresnel-reflection-dependent signal fluctuations.

4. 1. 3 Experimental results

First, without modulating the optical frequency of the laser output (i.e., using the

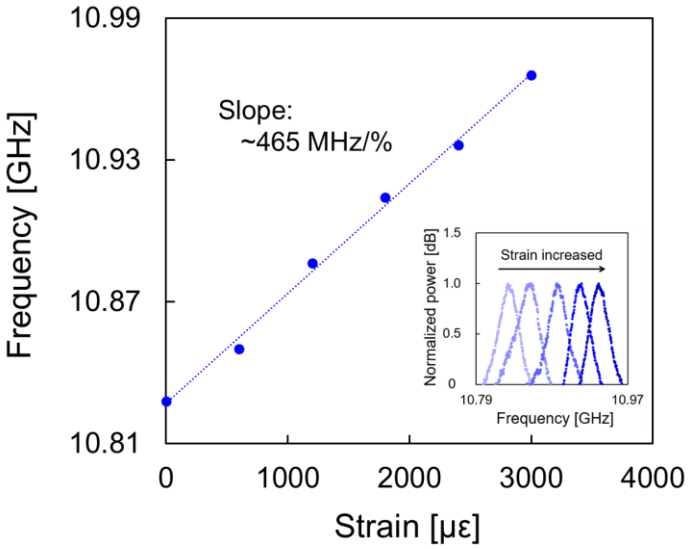

(a)

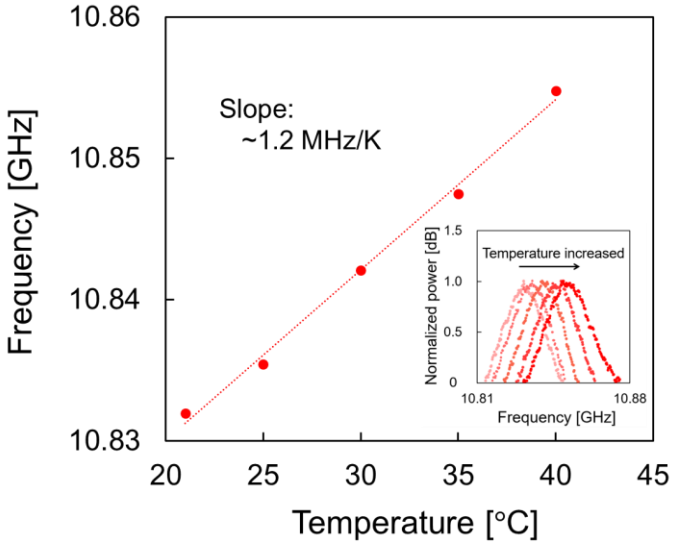

(b)

Fig. 4.2 Measured dependencies of the BGS (insets) and the BFS on (a) strain and (b) temperature. Each BGS was normalized so that its maximal power became 1. The BFS was extracted from the BGS using Lorentzian fitting. The dotted lines are linear fits.

whole length of the FUT), the strain and temperature dependencies of the BGS and BFS in the low-bending-loss fiber were investigated. As shown in Fig. 4.2(a), with increasing strain, the BGS shifted to higher frequency (see the inset), and the BFS linearly depended on strain with a coefficient of 465 MHz/%. In the same manner (Fig. 4.2(b)),

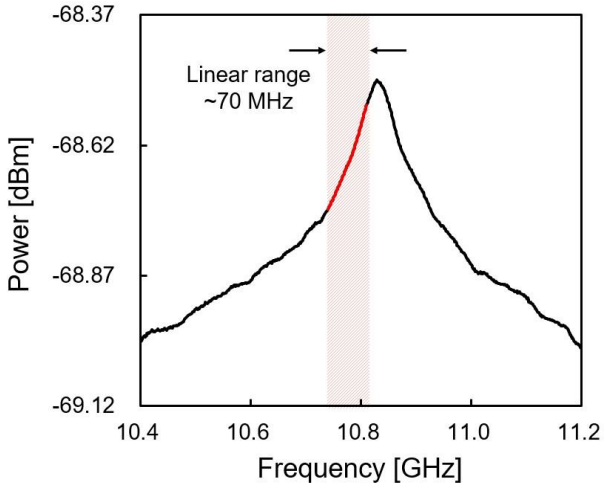

Fig. 4.3 BGS measured when the spatial resolution was 144 mm and the measurement range of 14.7 m. The linear range on the lower-frequency side is indicated in red.

with increasing temperature, the BGS also shifted to higher frequency (see the inset), with increasing temperature, the BGS also shifted to higher frequency (see the inset), and the BFS dependence coefficient on temperature was 1.2 MHz/K. The strain and temperature dependence coefficients are 0.9 and 1.1 times the values in standard silica fibers reported in Ref. 24 and 25; the small discrepancies are natural considering that the fiber cores are both composed of germanium-doped silica. Note that Brillouin bandwidth $\Delta\nu_B$ of this special fiber (non-strained, at room temperature) was approximately 40 MHz, which was used to calculate the nominal spatial resolution of the system using this fiber (see Eq. (1-2)). Next, we performed a single-point measurement of strain and temperature to evaluate the sensing performance of SA-BOCDR using the low-bending-loss fiber. The measured BGS is shown in Fig 4.3. By differentiating the BGS with respect to frequency, the optimal ν_{B0} value was calculated to be 10.81 GHz, and the linear range (defined as the range where the change in the BGS slope is suppressed within 20% compared to its maximum) was calculated to be ~70 MHz. We then applied strains of up to 1200 με to the 0.15-m-long section (at the midpoint of which the correlation peak was located) and measured the dependencies of the power-change distributions (Fig. 4.4). Each distribution was displayed with an artificial shift of 0.2 dB for clear comparison. At the strained position, a clear peak was observed, and its peak amplitude increased with increasing strain. Refer to Methods for the reason why the power-change distributions do not form rectangular shapes at the

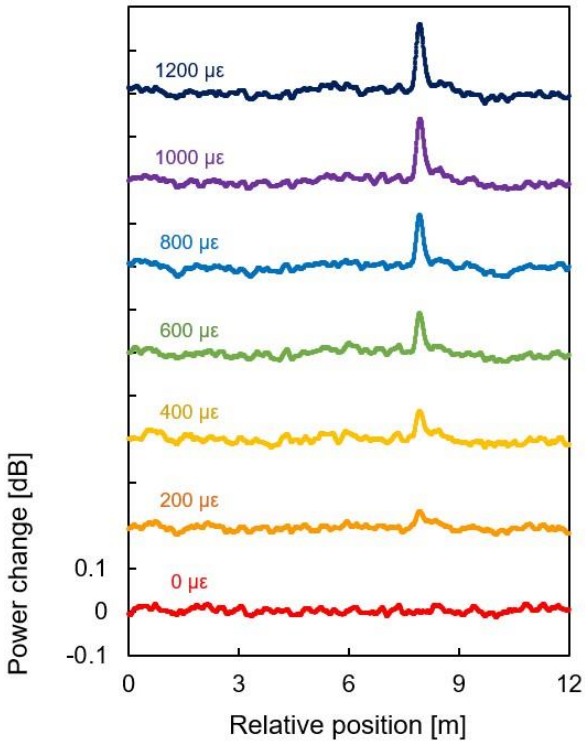

Fig. 4.4 Measured strain dependence of the power-change distributions. Each distribution is shifted by 0.2 dB.

strained position. Figure 4.5(a) shows the maximal power change plotted as a function of the strain. The dependence was almost linear with a coefficient of 1.42×10^{-4} dB/με; the slight discrepancy from the linear trend seems to have been caused by the imperfectly straight BGS slope even within the linear range. The power-change dependence on temperature (< 50 °C) was investigated under the same conditions, and as shown in Fig. 4.5(b), an almost linear behavior with a coefficient of 3.28×10^{-3} dB/K was obtained. These values were in moderate agreement with the theoretical values calculated using the BGS shape and the strain and temperature dependence coefficients of the BFS.

Finally, the loss-insensitive operation of SA-BOCDR was demonstrated using the FUTs depicted in Fig. 4.6. Two different types of 12.0-m-long silica SMFs (a standard SMF (FPC-SM20, Alnair Labs) and the aforementioned low-bending-loss SMF) were employed. Heat (50 °C) and strain (600 με) were applied to 0.15-m-long sections, and bending losses were applied between the heated and strained sections. The bending loss was applied by winding the fibers around rods for one turn without strain. The radii of

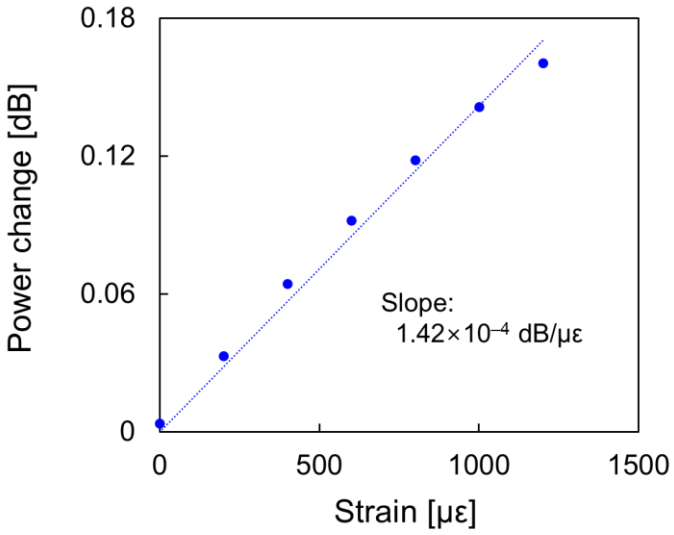

(a)

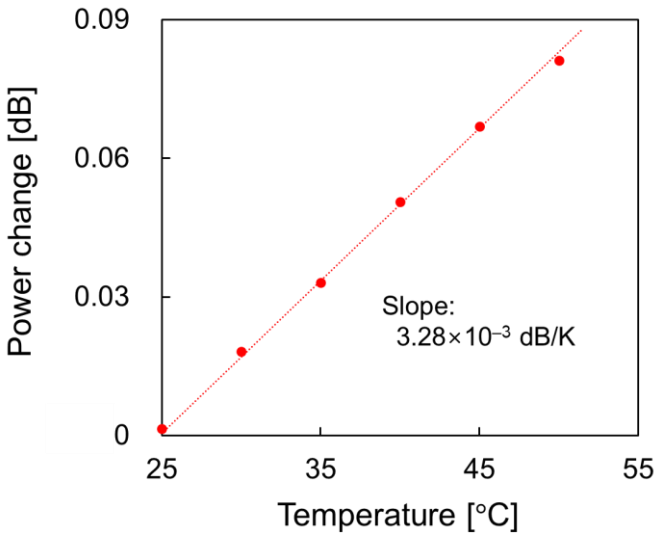

(b)

Fig. 4.5 Measured power-change dependencies on (a) strain and (b) temperature. The dotted lines are linear fits.

the rods were 8 and 10 mm, which theoretically induce bending losses of ~3.1 and ~0.8 dB for the standard SMF, respectively [89]. The bending losses induced to the special SMF were relatively low (<0.02 dB).

Figure 4.7(a) shows the power-change distributions measured along the standard SMF with 8- and 10-mm rod radii. The vertical axis was normalized so that the maximal power change at the heated section became 1 (when the rod radius was 10 mm). Note

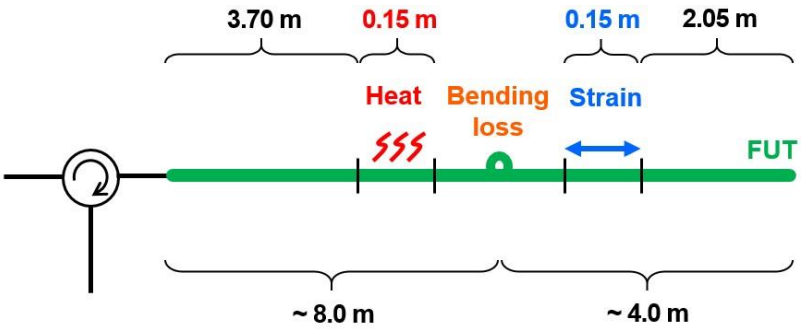

Fig. 4.6 Structure of the FUT, where heat, strain, and bending loss were applied.

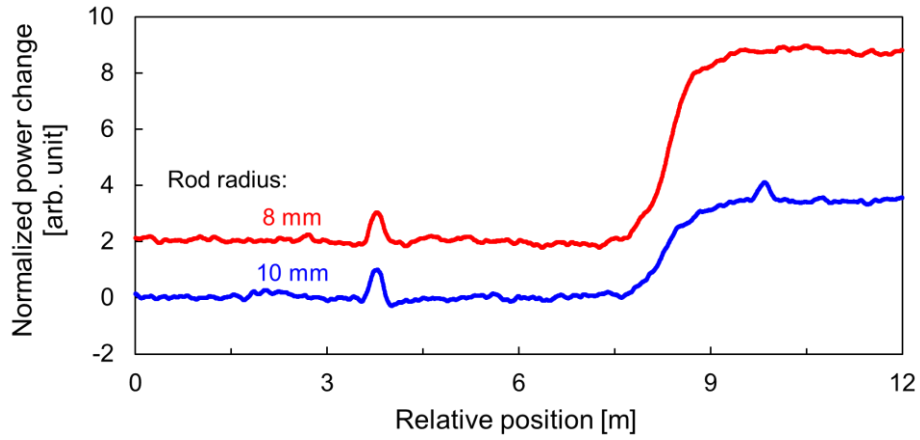

(a)

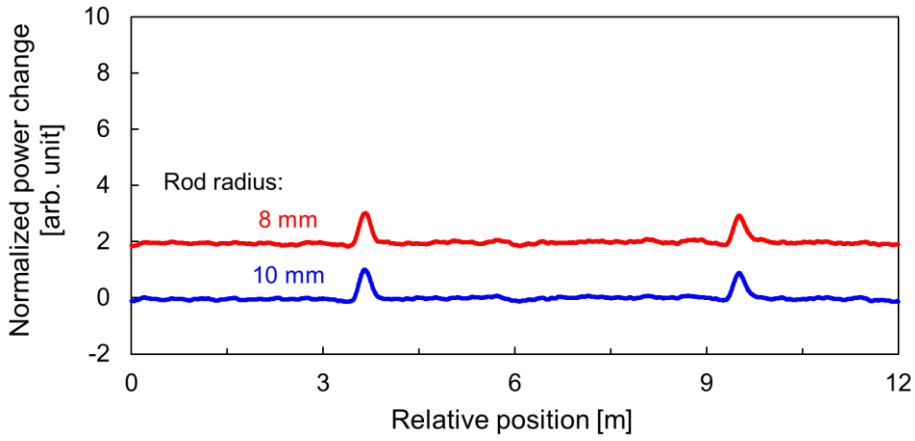

(b)

Fig. 4.7 Normalized power-change distributions with rod radii of 8 and 10 mm when the FUT was (a) the standard silica SMF and (b) the low-bending-loss silica SMF. Each distribution is shifted by 2.

that the two distributions were displayed with an artificial shift of 2 for clear comparison. Regardless of the rod radii, the heated sections were correctly detected, and the rough locations of the applied bending losses were also detected (Refer to Methods for the reason why the power-change distributions do not form rectangular shapes at the heated/strained positions). However, when the rod radius was 10 mm, the location of the strained section was correctly detected, but the strain magnitude appeared to be much smaller than the actual value (which is approximately 0.6). This is because the BGS power reduced by bending loss lead to the reduction in the spectral slope, resulting in the reduced sensitivity to strain. When the rod radius was even smaller (8 mm), the loss was so high that the strained section was not detected at all. This is because the considerable loss almost completely diminished the BGS (i.e., the spectral slope became almost flat), and consequently, the strain-induced spectral shift posed only negligible influence on the final output. In contrast, Fig. 4.7(b) shows the normalized power-change distributions measured along the low-bending-loss SMF with 8- and 10-mm rod radii. The two distributions were similar to each other irrespective of the rod radii, and the heated and strained sections were correctly detected in both measurements. The applied bending losses did not affect the measured results, indicating that, by SA-BOCDR using this special fiber, a stable distributed measurement of strain and temperature can be performed with no influence of unintended local loss.

4. 1. 4 Conclusion

In this work, we verified the loss-insensitive operation of SA-BOCDR using the special SMF. First, we measured the coefficients of the power-change dependencies on strain and temperature to be 1.42×10^{-4} dB/με and 3.28×10^{-3} dB/K, respectively. Then, by comparing the distributed strain and temperature measurement results using the standard SMF and the special SMF, we proved the effectiveness of this loss-insensitively configured SA-BOCDR. To enhance the measurement stability further, the use of low-bending-loss polarization-maintaining fibers may be an option. We anticipate this configuration with high stability is of significant use in practically employing SA-BOCDR for structural health monitoring in the future.

4. 2 Stability and sensitivity

4. 2. 1 Preface

Since SA-BOCDR operates based on power information, the output signal is highly affected by the polarization-dependent power fluctuations. To mitigate this problem, a PSCR has been employed in the system. However, but the averaged state of polarization (SOP) leads to non-ideal sensitivity, and in addition, the use of the PSCR increases the cost and encumbers the downsizing of the system.

Thus, in this section, to resolve these shortcomings, we develop polarization-scrambling-free SA-BOCDR using a polarization-maintaining fiber (PMF) as an FUT. A PSCR is not employed in this configuration, leading to the cost reduction (when the FUT is relatively short). In addition, what is more important, the SOP can be optimized so that the sensitivity can be higher. First, we experimentally show that, unlike the case where the FUT is a silica SMF, PMF-based SA-BOCDR can operate correctly even when the PSCR is switched off. Subsequently, we characterize the fundamental sensing properties, such as the strain/temperature dependencies of the BFS and the Brillouin spectral power in the PMF, and show that the strain sensitivity of the PMF-based SA-BOCDR is 1.4 times higher than that of the conventional configuration.

4. 2. 2 Experimental setup

As the FUTs for distributed measurements, we used a silica SMF (LPSGK-S-SM, Sigma Koki) and a polarization-maintaining and absorption-reducing (PANDA) fiber (most commonly used PMF; P3-1550PM-FC, Thorlabs) [90]. The PANDA fiber had a core diameter of 8.5 μm and a relatively low propagation loss of ~0.4 dB/km. The BFSs of the silica SMF and PANDA fiber were 10.855 and 10.863 GHz, respectively, at 1.55 μm at room temperature (20 °C). The lengths of the two FUTs were both 9.15 m. Figure 4.8 schematically shows the experimental setup of SA-BOCDR, in which a PSCR can be switched on and off. Compared to the previous setup, a PC was newly employed to control the SOP when the PSCR was switched off. The 1.55-μm light from a

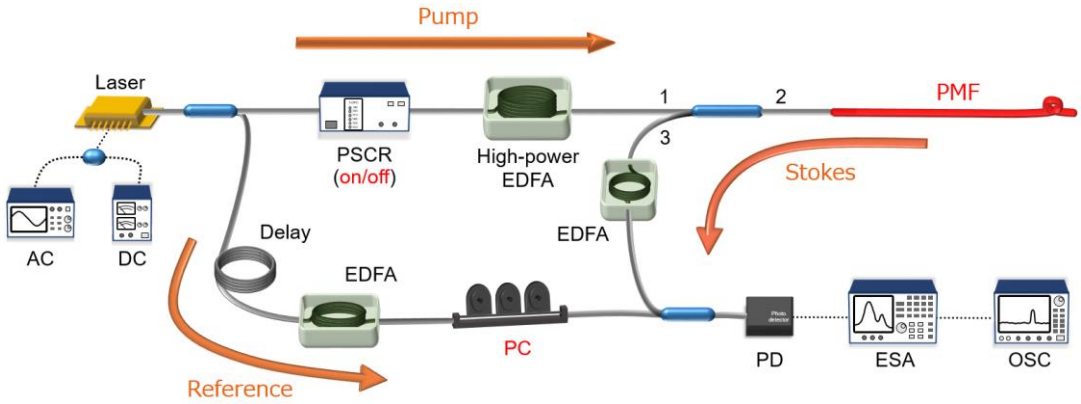

Fig. 4.8 Experimental setup of SA-BOCDR, in which the polarization scrambler (PSCR) can be switched on and off. EDFA, erbium-doped fiber amplifier; ESA, electrical spectrum analyzer; OSC, oscilloscope; PC, polarization controller; PD, photo diode; PMF, polarization-maintaining fiber.

distributed-feedback laser diode (NLK1C5GAAA, NTT Electronics) was divided into two: pump and reference lights. After amplified to 26 dBm using a high-power EDFA, the pump light was injected into the FUT. In this measurement, no special attempt was made to align the polarization state of the pump light to one of the eigenaxes of the PMF. To suppress the Fresnel reflection, a bending loss was applied near the distal end of the FUT. The backscattered Brillouin Stokes light from the FUT was amplified to ~1 dBm using another EDFA and coupled with the reference light. The reference light was amplified to ~2 dBm in advance after passing through a delay fiber (which was employed to avoid the appearance of the zero-optical-path-difference point, i.e., the 0th correlation peak, in the FUT; the length can be shortened to <<1 km, if necessary). Then, using a PD, the self-heterodyned optical signal was converted into an electrical signal, which was observed as a BGS using an ESA. The spectral power change at a fixed frequency (10.86 GHz for the PMF and 10.85 GHz for the SMF) was obtained using a zero-span mode of the ESA and observed using an OSC with 256 times averaging. The resolution and video bandwidths of the ESA were 10 MHz and 10 kHz, respectively. The room temperature was 20 °C.

By sinusoidally modulating the optical frequency of the laser output, a correlation peak was generated and scanned along the FUT, which enabled distributed measurement. Based on Eqs. (1-1) and (1-2), the spatial resolution and the measurement range were ~72.5 mm and ~11.4 m by setting the modulation frequency and amplitude

to 8.990–9.036 MHz and 1.5 GHz, respectively. Only when we performed single-point measurements to investigate the system performance, the modulation frequency was maintained at 9.023 MHz to obtain the Brillouin signal only from the correlation peak (located 7.15 m away from the end of the second-port pigtail of an optical circulator).

4. 2. 3 Experimental results

First, we performed distributed measurements of Brillouin spectral powers using the partially strained SMF and PMF under three SOPs: 1) optimized using the PC so that the power change at the strained section was maximized, 2) scrambled by switching the PSCR on so that the polarization-dependent power change along the FUTs was suppressed, and 3) anti-optimized using the PC so that the power change at the strained section was minimized. Strains of 1000 με were applied to 0.3-m-long sections (7.0–7.3 m away from the circulator) in both the FUTs. Figure 4.9 (a) and (b) show the power distributions along the SMF and PMF, respectively, under three SOPs. In the case of the SMF, only when the SOP was scrambled, the power distribution was relatively flat and the strained section was correctly detected. However, when the SOP was optimized, although the strained section was detected with higher strain sensitivity, the baseline was significantly distorted and the distributed measurement was clearly erroneous. In addition, when the SOP was anti-optimized, not only was the distributed measurement erroneous but also even the signal at the strained section was completely buried under the distorted baseline. Thus, when the SMF was used, polarization scrambling was found to be of paramount necessity for correct distributed measurements. In contrast, in the case of the PMF, regardless of the SOPs, the baselines were relatively flat and the strained sections were correctly detected. The strain sensitivity at the strained section was highest at the optimized SOP and lowest at the anti-optimized SOP (note that, when the SOP was scrambled, the results were almost identical between the SMF and PMF). Thus, when the PMF was used, polarization scrambling was not necessary any longer, leading to the cost reduction of the system (when the FUT length is relatively short; considering the high cost of the FUT, the PMF-based configuration is not suitable for long-distance measurements). Besides, from the viewpoint of strain sensitivity, the SOP should be optimized instead of being scrambled.

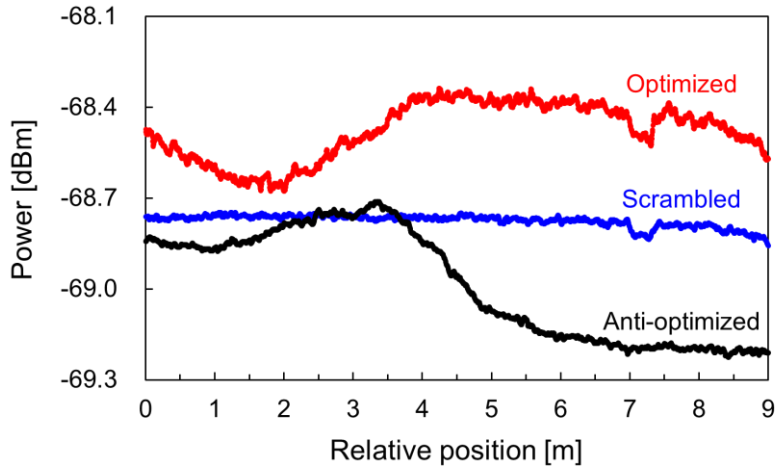

(a)

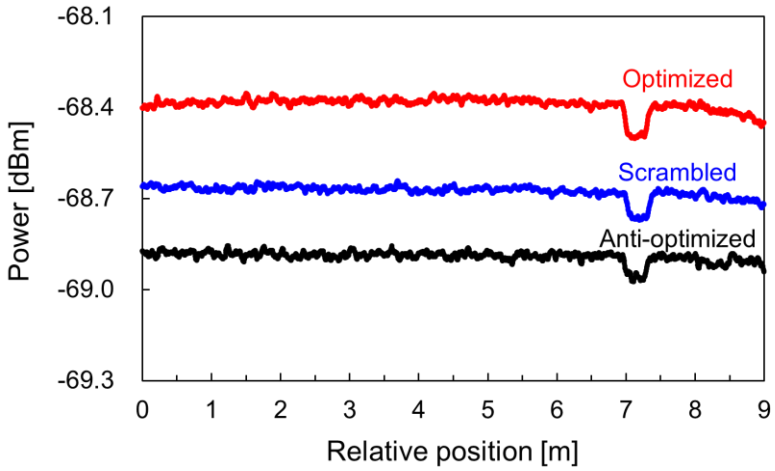

(b)

Fig. 4.9 Spectral power distributions along (a) the SMF and (b) the PMF measured at three different states of polarization, when 1000 με strain was applied to the FUTs (7.0–7.3 m).

In the experiments below, we characterized the fundamental operations of PMF-based SA-BOCDR and, in both experiment and theory, quantitatively evaluated how much the strain sensitivity can be improved by optimizing the SOP. First, we investigated the BFS dependencies on strain and temperature in a 0.57-m-long PMF. Without applying frequency modulation, the BGS was observed when strains from 0 to 4800 με were applied to the whole length of the FUT. The BFS was then plotted as a function of the strain in Fig. 4.10(a). With increasing strain, the BGS linearly shifted to

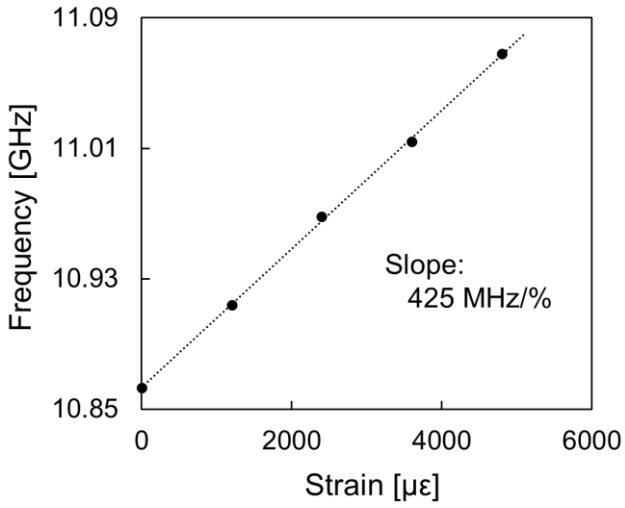

(a)

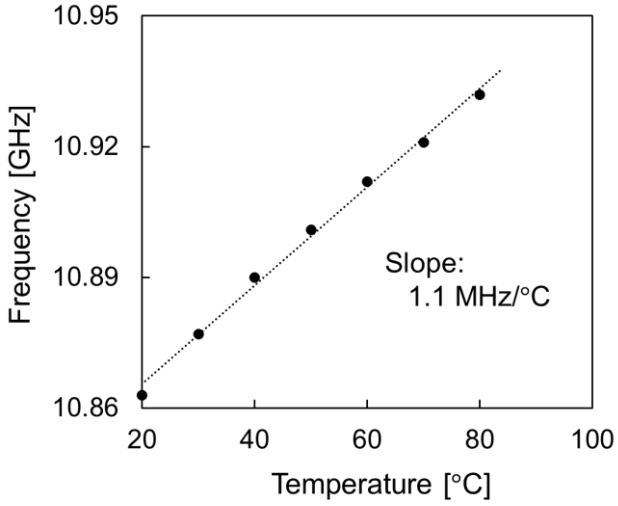

(b)

Fig. 4.10 BFS dependencies on (a) strain and (b) temperature in the PANDA-type PMF. The dotted lines are linear fits.

higher frequency with a coefficient of 425 MHz/%, which is ~0.82 times the value in a typical SMF [25]. In the same manner, the BFS dependence on temperature was also measured (Fig. 4.10(b)). With increasing temperature from 20 to 80 °C, the BFS also increased with a coefficient of 1.1 MHz/°C, which is almost the same as that in an SMF [26].

Subsequently, after frequency modulation was applied, we measured the BGSs under three different SOPs (Fig. 4.11(a)). The Brillouin spectral power was highest at the

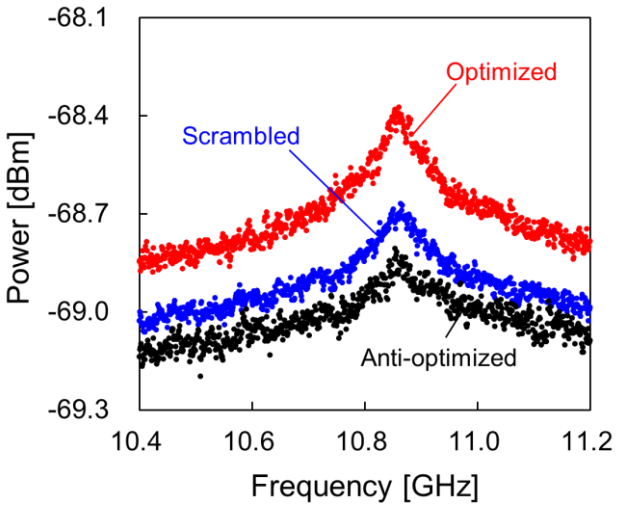

(a)

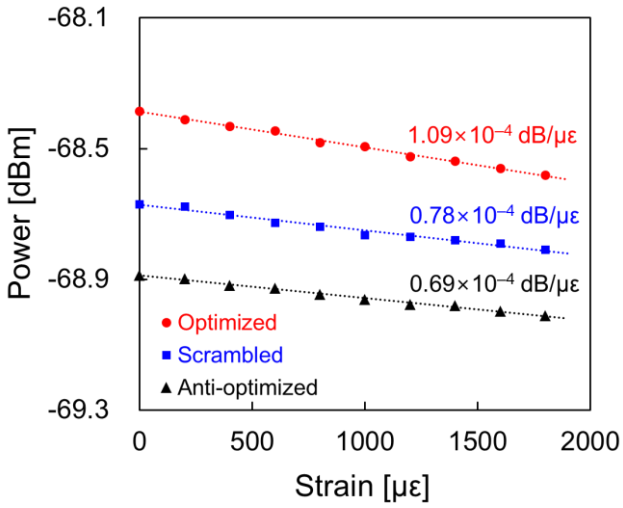

(b)

Fig. 4.11 (a) Measured BGS in the PANDA-type PMF at three different SOPs. (b) Spectral power plotted as a function of the applied strain at three different SOPs. The dotted lines are linear fits.

optimized SOP and lowest at the anti-optimized SOP, and using the spectral slope at 10.86 GHz (derived from Fig. 4.11(a)) and the strain coefficient of the BFS, we can calculate the theoretical strain sensitivities of the spectral power to be 0.96×10^{-4}, 0.76×10^{-4}, and 0.66×10^{-4} dB/με (corresponding to the temperature sensitivities of 2.49×10^{-3}, 1.97×10^{-3}, and 1.72×10^{-3} dB/°C) at optimized, scrambled, and anti-optimized SOPs, respectively. Finally, at three different SOPs, we measured the spectral power dependencies on strain (Fig. 4.11(b)). The dependencies were almost linear and

the coefficients were 1.09×10^{-4}, 0.78×10^{-4}, and 0.69×10^{-4} dB/με at optimized, scrambled, and anti-optimized SOPs, respectively. These values are in moderate agreement with the aforementioned values calculated from the BGS. In this measurement, the standard deviation of the power fluctuations along the non-strained section was approximately +/–0.01 dB, which corresponds to a strain uncertainty of ~190 με. The most important finding here is that the strain sensitivity at the optimized SOP is 1.4 times higher than that at the scrambled SOP. Note that it is difficult to derive this value theoretically based on the theory developed by Deventer *et al*. [91], because the BGS observed in correlation-domain techniques is inherently influenced by bell-shaped background noise [82]. It is also not easy to compare the increased sensitivity with the previously reported sensitivities because SA-BOCDR has the measurement sensitivity dependencies on various experimental conditions including incident light power, spatial resolution, and resolution and video bandwidths of an ESA (see Chapter 3.3 for details). Nevertheless, our results clearly indicate that, compared to conventional SMF-based SA-BOCDR, the PMF-based SA-BOCDR can offer polarization-scrambling-free operation with high strain/temperature sensitivity along with the high stability.

4. 2. 4 Conclusion

We developed and characterized the PMF-based SA-BOCDR with no need of polarization scrambling. First, we showed that, unlike silica-SMF-based systems, PMF-based SA-BOCDR can operate with higher stability even when the PSCR is switched off. This enables the use of the optimized SOP for higher sensitivity. After investigation of the strain/temperature dependencies of the BFS and the Brillouin spectral power in the PMF, we finally showed that the strain sensitivity of the PMF-based SA-BOCDR is 1.4 times the value of the standard silica-SMF-based configuration. Considering the cost of PMFs, this configuration is suitable for high-resolution sensing with a relatively short measurement range. We anticipate that this PMF-based SA-BOCDR will be of significant use for practical structural monitoring in the future owing to its single-end accessibility, higher stability, and enhanced sensitivity.

4. 3 Strain dynamic range

4. 3. 1 Preface

Remarkable progress has been made to improve performance of SA-BOCDR. However, one of the important problems unsolved yet is its strain (or temperature) dynamic range limited by the narrow linear range of the BGS slope. The linear range is generally reported to be several tens of megahertz as described in Chapter 2, which corresponds to a relatively small strain of ~0.15% (or temperature change of ~64 K). This value is far from being sufficient for some practical applications [92–94].

The simplest idea to improve the strain dynamic range is to exploit not only the linear range but also the nonlinear range of the BGS. However, this approach may not operate so effectively as expected, because the BGS observed in BOCDR involves a unique bell-shaped background noise floor [59, 82], which is not sensitive to the strain applied to the sensing position. Thus, it is crucial to extend the upper limit of the measurable strain by another method.

In this section, to start with, we experimentally confirm that the aforementioned idea, i.e., additional use of the nonlinear range of the BGS, is not effective. The maximal measurable strain obtained by this approach is found to be merely ~0.25%. Then, we clarify that SA-BOCDR has a trade-off relation between the strain dynamic range and the spatial resolution and that the former can be extended at the sacrifice of the latter. In the experiment, we achieve a strain dynamic range of >0.6% when the spatial resolution is 3 times lower.

4. 3. 2 Principle

In Chapter 2, we determined the strain dynamic range by the linear range of the BGS slope. It may be feasible to extend the dynamic range if the nonlinear range (foot of the BGS) is additionally used to measure strain at the cost of the deteriorated sensitivity. However, the effect of this method is probably limited because the BGS observed in BOCDR inherently involves a bell-shaped background noise floor. This noise is caused

by accumulation of the Brillouin signals from non-correlation (or non-sensing) sections along the FUT [59, 82]. As the nonlinear range of the BGS is mostly located on this noise floor, drastic improvement of the strain dynamic range cannot be expected by this method.

Here, we draw attention to the fact that the bell-shaped noise floor consists predominantly of the Brillouin signals from the non-sensing sections close to the sensing section (in other words, the closer the non-correlation sections are to the correlation peak, the greater their contributions to the noise floor become). Therefore, if we intentionally lower the spatial resolution and include initially non-sensing sections into newly defined sensing section, the noise floor will be drastically diminished; as a result, the strain dynamic range will be greatly enhanced. Thus, SA-BOCDR has a trade-off relation between the strain dynamic range and the spatial resolution. We give experimental analysis on this nature in this paper.

4. 3. 3 Experimental setup

The experimental setup of SA-BOCDR is depicted in Fig. 4.12. A continuous lightwave from a laser with a center wavelength of 1.55 μm was divided into two light beams: pump and reference. After amplified to ~26 dBm using an EDFA, the pump light was injected into the FUT. The Brillouin-scattered Stokes light was then amplified to ~2 dBm using another EDFA and coupled with the reference light for heterodyne detection. The reference light was amplified to ~1 dBm after passing through a ~1-km-long delay fiber. After converted into an electrical signal using a photodiode, the heterodyned signal was guided to an ESA (video bandwidth: 10 kHz, resolution bandwidth: 10 MHz). Using the narrowband- pass filtering function of the ESA, the change in the spectral power at 10.80 GHz was transmitted to an OSC. The repetition rate was 100 Hz, and averaging was performed 512 times on the OSC to achieve a higher SNR.

As shown in Fig. 4.13, we used a 7.5-m-long silica SMF with a BFS of 10.82 GHz at room temperature (20 °C). A bending loss was applied near the open end to suppress the Fresnel reflection.

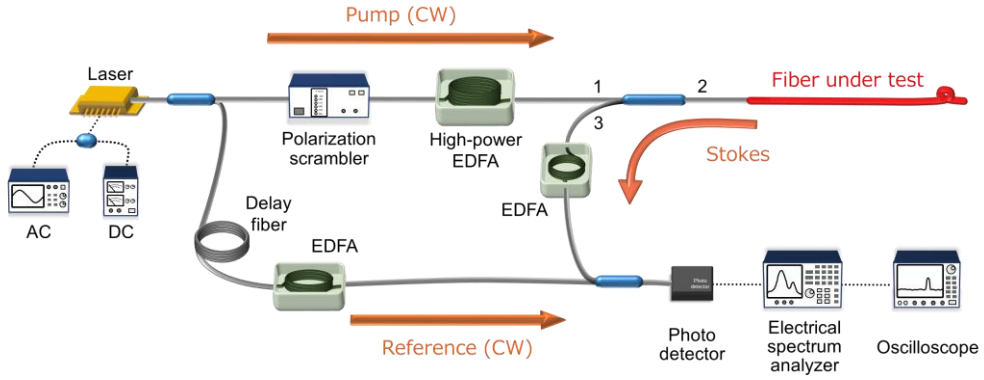

Fig. 4.12 Experimental setup of SA-BOCDR. AC, alternating current; CW, continuous wave; DC, direct current; EDFA, erbium-doped fiber amplifier.

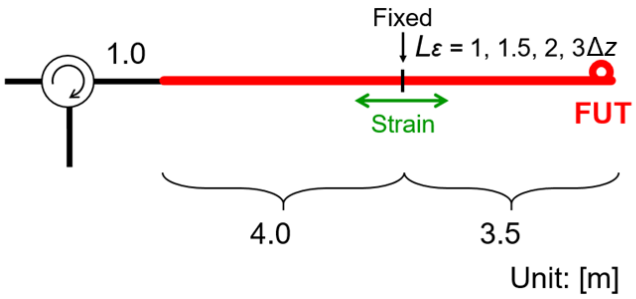

Fig. 4.13 Structure of FUT.

We performed two experiments: one was to measure the strain dynamic range of standard SA-BOCDR and to confirm the origin of its limitation, and the other was to investigate the trade-off relation between the strain dynamic range and the spatial resolution. In the first experiment, we set the modulation frequency f_m and modulation amplitude Δf to 9.80–9.97 MHz and 0.27 GHz, respectively, which correspond to the meausrement range d_m of ~10.3 m and the theoretical spatial resolution Δz of ~0.37 m according to Eqs. (1-1) and (1-2). Distributed strain measurements were performed when strains of 0–0.7% were applied to a ~0.37-m-long section (same as Δz). We simultaneously measured the BGSs in the strain range of 0–0.3% when the correlation peak was located ~4.0 m away from the end of the second-port SMF of an optical circulator (see Fig. 4.13; f_m was 9.89 MHz). In the second experiment, similar measurements of strain distributions and single-point BGSs were performed, but with elongated strained lengths L_ε from Δz to $3\Delta z$, which can be regarded as intentionally lowered spatial resolutions.

4. 3. 4 Experimental results

First, we present the results of SA-BOCDR-based distributed strain measurements when relatively large strains were applied. Figure 4.14(a) shows an example of the measured distribution of the spectral power change along the whole FUT when a 0.25% strain was applied to a ~0.37-m-long section. The vertical axis was normalized so that the maximal power change became 1. The power change at the strained section was detected; a triangular shape (not rectangular) indicates the correct operation of SA-BOCDR when the strained length equals the sptatial resolution. Similar measurements were performed at various strains in the range of 0–0.7%. Figure 4.14(b) shows the measured dependence of the normalized power change (at the midpoint of the strained section) on applied strain. With increasing strain, the power change also increased, but the slope became gradually small (moderately fitted by an exponential curve). When strain was smaller than ~0.15%, the dependence was almost linear, which agrees well with previous reports. However, in the strain range of approximately 0.15–0.25%, the slope became smaller, which can still be used to measure strain because the power change and strain are in one-to-one correspondence. In contrast, once the strain exceeded ~0.25%, the power change showed no significant growth and became almost constant. These results indicate that the use of the nonlinear range of the BGS slope is not an effective method for improving the strain dynamic range, which was slightly extended from 0.15% to 0.25% in this experiment. We also measured the BGSs while applying strains of 0–0.3% to the ~0.37-m-long section in the FUT. As shown in Fig. 4.14(c), with increasing strain, the spectral power at 10.80 GHz decreased when the applied strain was smaller than ~0.25%, which corresponds to the trend in Fig. 4.14(b). However, it is clear that, when strain was larger, the spectral power stopped decreasing because of the aforementioned bell- shaped background noise floor. This observation confirms that the strain dynamic range of SA-BOCDR is, even when the nonlinear range of the spectral slope is exploited, significantly restricted by this unique noise structure.

Subsequently, we show the results when the spatial resolution was lowered. Fig. 4.15(a) shows the BGSs measured when the strains of 0–0.6% were applied to a 1.1-m-long section (corresponding to $3\Delta z$) in the FUT. Unlike in the case where the strained

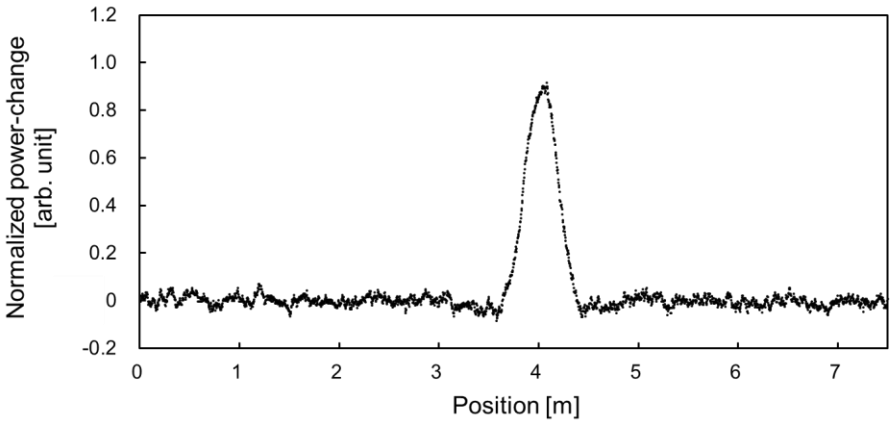

(a)

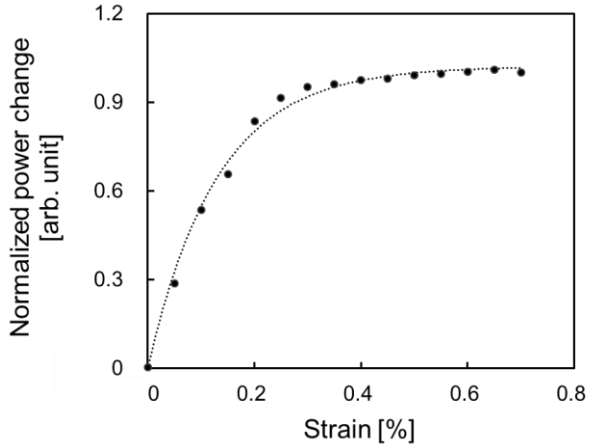

(b)

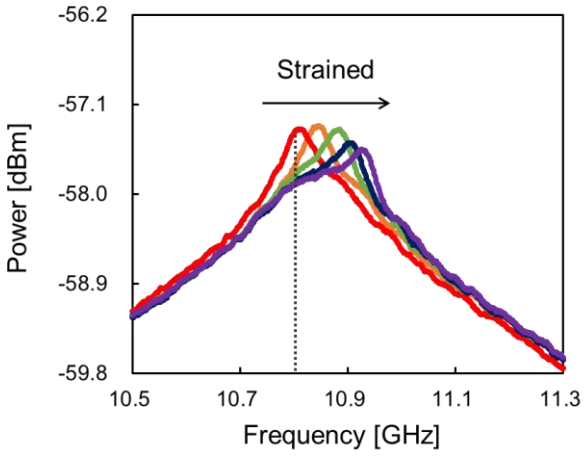

(c)

Fig. 4.14 (a) Measured distribution of the normalized power change when the applied strain was 0.25%. (b) Normalized power change plotted as a function of applied strain. The dotted curve is an exponential fit. (c) BGSs measured at strains of 0, 0.1, 0.2, 0.25, 0.3% when the strained length L_ε was the same as the nominal spatial resolution Δz (= ~0.37 m).

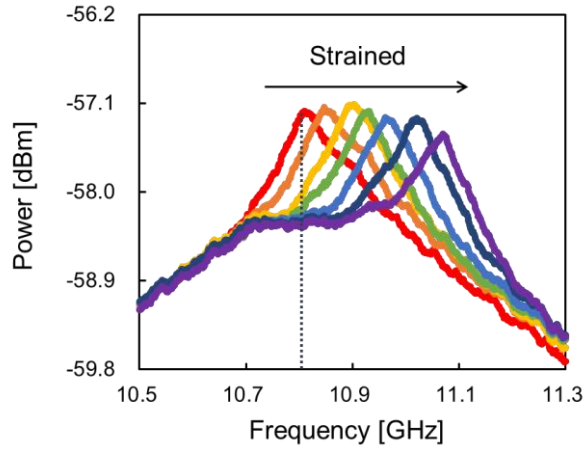

(a)

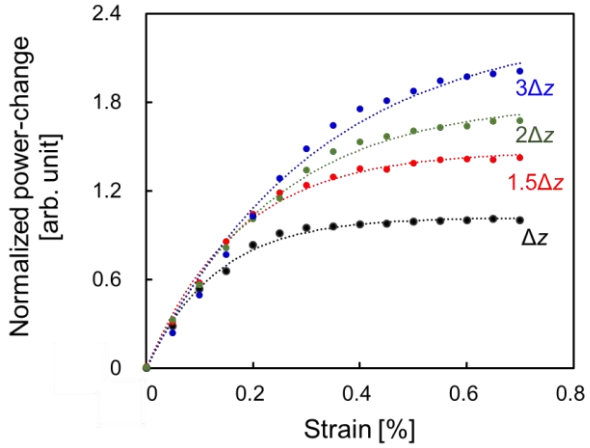

(b)

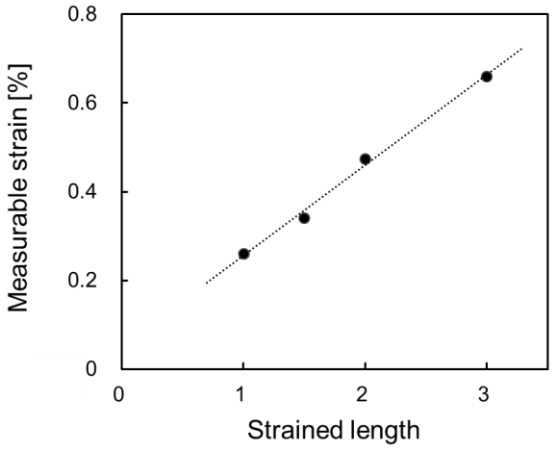

(c)

Fig. 4.15 (a) BGSs measured at strains of 0–0.6% (step: 0.1%) when the strained length L_ε was 3Δz, where Δz is ~0.37 m. (b) Normalized power changes plotted as functions of applied strain when the L_ε values were Δz, 1.5Δz, 2Δz, and 3Δz. The dotted curves are exponential fits. (c) Maximal measurable strain plotted as a function of L_ε. The dotted line is a linear fit.

length L_ε was Δz, the spectral power at 10.80 GHz decreased even when the applied strain was larger than 0.25%. This is because part of the noise floor shifted to higher frequency owing to the lowered resolution. This trend was basically the same when L_ε was $1.5\Delta z$ and $2\Delta z$. Figure 4.15(b) shows the strain dependence of the normalized power change (at the midpoint of the strained section). Regardless of L_ε, the power change increased with increasing applied strain. The slope became gradually small, and the power change finally became almost constant, in the same manner as in Fig. 4.14(b). However, is is notable that, with increasing L_ε, the strain at which the power change became constant increased. In Fig. 4.15(c), As a function of L_ε, we finally plotted the maximal measurable strain, which we defined as the strain at which the power change reaches ~86.5% of its saturated value. As L_ε increased, the maximal measurable strain increased almost linearly with a coefficient of ~0.2% in this experiment. When the spatial resolution was 3 times lowered, the strain dynamic range was >0.6%. Thus, we proved that the strain dynamic range can be improved at the cost of the spatial resolution in SA-BOCDR.

4. 3. 5 Conclusion

We clarified that SA-BOCDR has a trade-off relation between the strain dynamic range and the spatial resolution. To start with, we measured the BGSs when applied strains were larger than the previously reported upper limit (~0.15 %), and proved that the limited strain dynamic range is caused by the bell-shaped noise floor peculiar to the correlation-domain techniques. Then, by making use of the nature of this noise floor, we showed that the strain dynamic range can be improved at the cost of the spatial resolution. In the experiment, a strain dynamic range of >0.6% was achieved with a spatial resolution lowered by 3 times. Considering that the spatial resolution of BOCDR is relatively high even in its standard configuration, such a lowered spatial resolution should still be useful in some applications. We have some other ideas to improve the strain dynamic range; for instance, by low-pass filtering the BGS, the dynamic range will be improved, but at the sacrifice of the measurement sensitivity. Using multiple spectral powers will be another approach, but the signal processing will be more complicated. Thus, we believe that our simple approach to widening the strain dynamic

range of SA-BOCDR will be of significant use for practical applications in structural health monitoring in the future.

4. 4 Robustness

4. 4. 1 Preface

In previous Chapters, we have characterized the operation of SA-BOCDR with some unique features and performed some studies to improve performance of the system, such as stability, sensitivity, and strain dynamic range. However, all the experiments were carried out using silica fibers, which are relatively fragile and easily cut even at several strains.

To tackle this problem, in this section, we implement SA-BOCDR using a polymer optical fiber (POF). Furthermore, use of POF can extend upper limit of detectable strain [70] and provide much higher temperature sensitivity [72]. However, due to their high propagation loss, the strain and temperature sensitivities are dependent on sensing position because the transmitted power is gradually reduced with light propagation. After analyzing how the performance is affected by this unique effect, we show that a correct POF-based distributed measurement using SA-BOCDR is feasible by compensating the sensitivity dependence on sensing position.

4. 4. 2 Principle

As described in Chapter 1, when the pump light is injected into the fiber, due to the interaction with acoustic phonons, backscattered Stokes light is generated through Brillouin scattering. And due to the Doppler shift, the central frequency of the BGS is lowered than that of the pump light spectrum. This frequency downshift is referred to as BFS, which is about ~10.8 GHz for silica SMFs [24] and ~2.8 GHz for perfluorinated POFs [72] at telecommunication wavelength, 1550 nm. When strain or temperature change is applied to the fiber, the BFS shifts to higher or lower frequency depending on

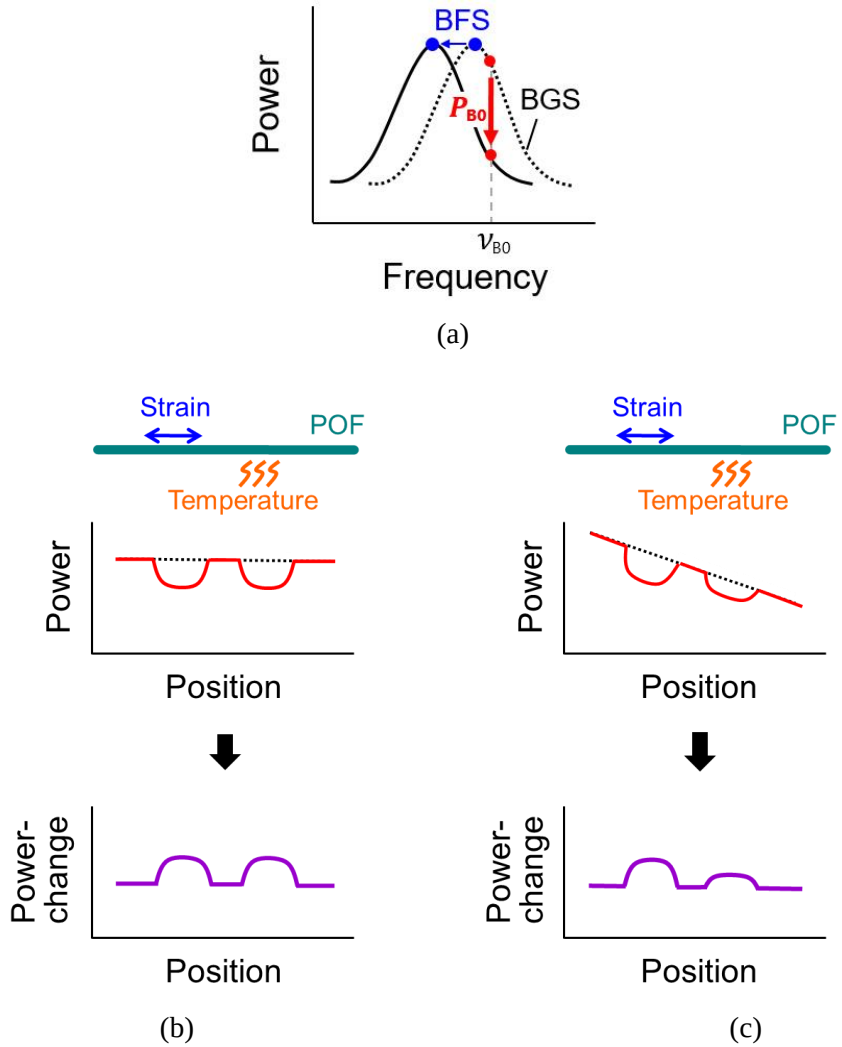

Fig. 4.16 (a) Schematic of the operating principle of SA-BOCDR. (b, c) Power and power-change distributions along (b) a low-loss fiber and (c) a high-loss fiber; with (solid curves) and without (dotted lines) partial strain and heat.

the fiber types. Their strain- and temperature-dependence coefficients are reported to be approximately 500 MHz/% and 1 MHz/K for silica SMFs [25, 26] and –120 MHz/% and –3 MHz/K for POFs [70, 72]. These dependences have been a basic sensing mechanism of Brillouin-scattering-based distributed measurements.

Since standard BOCDR needs to acquire the whole BGS to calculate the BFS at a single sensing position (as a peak frequency of the BGS) [61, 62], its operating system has been limited. On the other hand, SA-BOCDR only observe the spectral power change at a certain frequency ν_{B0} by exploiting its one-to-one correspondence to the

BFS (Fig. 4.16(a)), high-speed measurement is feasible.

When a silica SMF with a low propagation loss is used as an FUT, unless the FUT is extremely long, the Brillouin power shows almost no change irrespective of the sensing position (Fig. 4.16(b)). However, when a relatively high-loss fiber is used, even when the FUT is short, the Brillouin power decreases with increasing distance from the proximal end of the FUT (i.e., the pigtail end of the second port of a circulator) as shown in Fig. 4.16(c). Note that the final system output of SA-BOCDR is provided as a power-change distribution, and strain (or heat) is displayed as a positive shift in the vertical axis. The weakening of the BGS along the high-loss fiber leads to the reduction in the spectral slope, finally resulting in the gradual decrease in the strain and temperature sensitivities.

4. 4. 3 Experimental setup

As an FUT, a 15.0-m-long perfluorinated graded-index POF was employed. The POF had a three-layered structure consisting of core, cladding, and overcladding (diameters: 50, 70, and 490 μm, respectively), and a propagation loss of the POF was ~250 dB/km at 1550 nm.

The experimental setup of POF-based SA-BOCDR is basically the same as that of silica SMF-based SA-BOCDR. Only the FUT along all the light paths is POF. A laser diode at 1550 nm with a bandwidth of ~1 MHz was used as a light source. The pump light was amplified to ~25 dBm using an EDFA and injected into the FUT. The backscattered Stokes light was amplified to ~1 dBm using another EDFA. After passing through a ~1-km-long delay fiber, the reference light was guided to another EDFA and amplified to ~2 dBm, and then coupled with the Stokes light for heterodyne detection. Instead of polarization scrambler (PSCR), a polarization controller was used to optimize the polarization state so that the SNR became maximal for each measurement (note that the use of a PSCR for observing Brillouin signals in POFs causes considerable reduction in SNR [72]). The heterodyned signals were converted into electrical signals using a PD and observed as a Brillouin signal using an ESA.

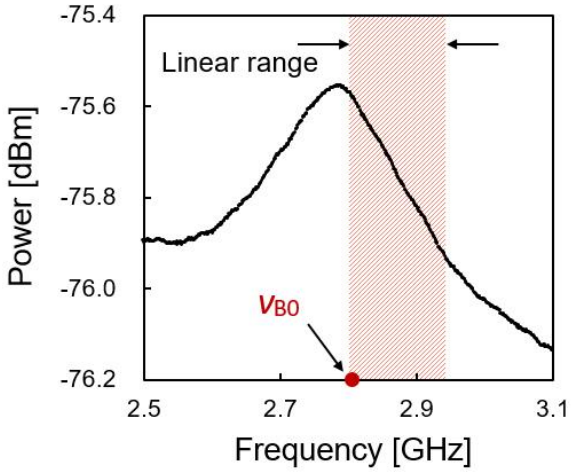

Fig. 4.17 Local BGS obtained at 1.0 m away from the proximal POF end.

Then, exploiting the zero-span mode (narrow band-pass filtering function) of the ESA (video bandwidth: 10 kHz; resolution bandwidth: 10 MHz), the spectral power change at ν_{B0} was sequentially output to an OSC. As a preparatory experiment for determining the ν_{B0} value and the bandwidth of the linear region, we measured the local BGS obtained at 1.0 m away from the proximal POF end (Fig. 4.17). The detailed measurement conditions are described in the next paragraph. The BFS was 2.76 GHz at room temperature (25°C). The optimal ν_{B0} value was found to be 2.80 GHz, which was set to a higher frequency than the BFS because the BGS shifts to lower frequency in POFs with strain and/or heating [72] (unlike the case of silica-SMF-based SA-BOCDR). The bandwidth of the linear region (see Chapter 2 for its definition) was approximately 140 MHz (2.80–2.94 GHz), which corresponds to the strain of up to ~1.15% and the temperature change of ~43°C in the POF (with light propagation, the BGS is basically weakened in the vertical direction; in other words, if normalized, the BGS shows an only negligible change depending on the location, leading to almost no position dependence of the linear range). Here we discuss the shape of the BGS, which is neither Lorentzian nor symmetrical. Compared to silica fibers, POFs inherently have a much wider Brillouin bandwidth (>100 MHz) [70]. Moreover, in general, as the modulation amplitude grows higher, the Brillouin bandwidth becomes wider [62], which deviates the BGS from a Lorentzian shape. Meanwhile, the asymmetric shape originates from the overlap of the foot of the Rayleigh spectrum [73], which also grows wider by modulation in the same manner as the BGS [62]. Note that the BFS of the POF (~2.8

GHz) is ~4 times lower than that of silica fibers [70] and that the BGS is more likely to be overlapped by the Rayleigh spectrum.

In the preceding measurement as well as in the following experiments, the modulation frequency f_m and amplitude Δf were set to 6.15–6.33 MHz and 0.6 GHz, respectively, corresponding to the measurement range of 18.1 m and the theoretical spatial resolution of 0.96 m according to Eqs. (1-1) and (1-2). The repetition rate was set to 100 Hz, and averaging was performed 128 times on the OSC to improve the SNR.

4. 4. 4 Experimental results

First, to derive the theoretical strain and temperature sensitivities as functions of sensing position, we measured the BGS distribution along the POF with a constant interval of 1.0 m using standard BOCDR (Fig. 4.18). Due to the high propagation loss in the POF, the peak power of the BGS gradually decreased with light propagation, which also induced the reduction in its spectral slope. Note that the BGS is weakened even within the fiber length of the spatial resolution, resulting an unavoidable measurement error. Here we interpreted the measured sensitivity as that of the midpoint of the corresponding fiber section.

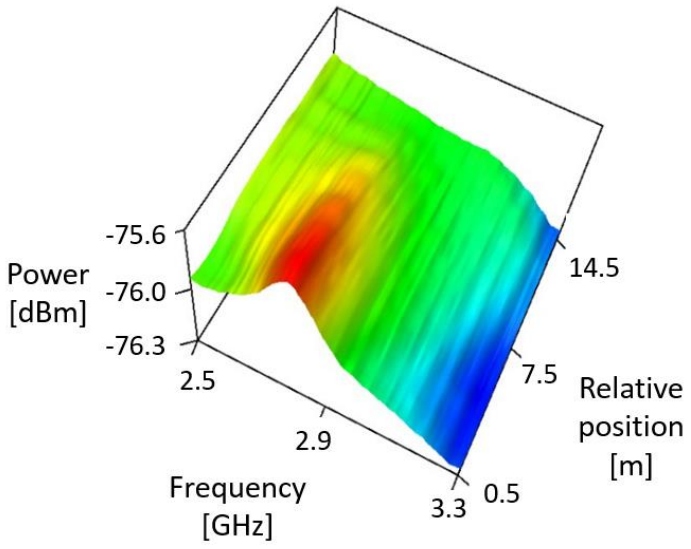

Fig. 4.18 BGS distribution along the POF.

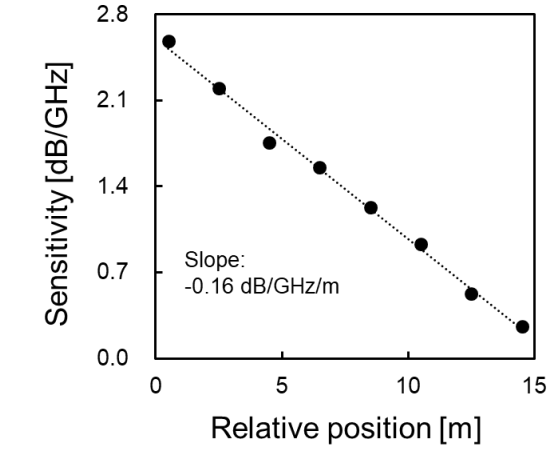

(a)

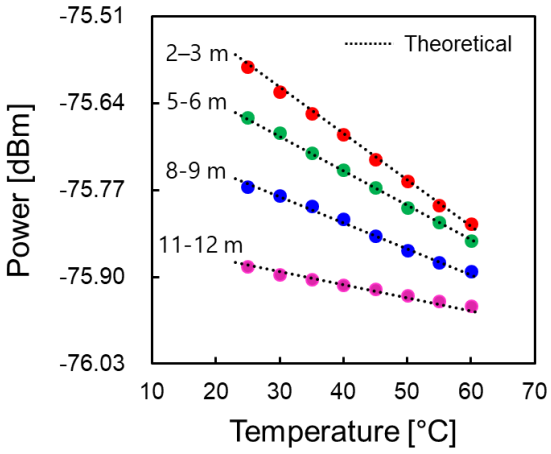

(b)

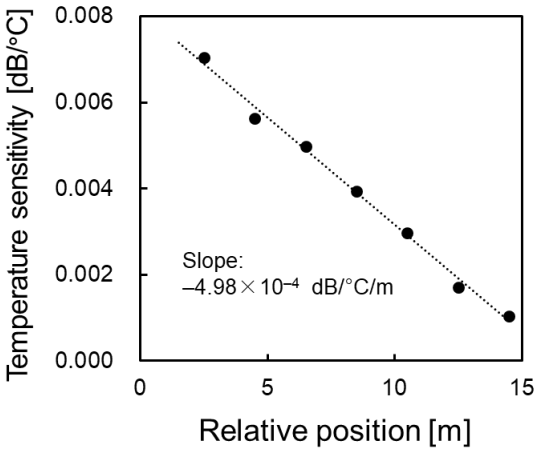

(c)

Fig. 4.19 (a) Sensitivity plotted as a function of sensing position for theoretical analysis. The dotted line is a linear fit. (b) Spectral powers plotted as functions of temperature; measured at four different sections in the POF. The dotted lines are theoretical trends. (c) Temperature sensitivity plotted as a function of sensing position. The dotted line is a linear fit.

By differentiating the spectral slope in the linear range (ν_{B0} = 2.80–2.94 GHz, the theoretical dependence of the sensitivity on sensing position was derived (Fig. 4.19(a)). The slope decreased almost linearly as the sensing position became far from the proximal POF end with a coefficient of approximately –0.16 dB/GHz/m, which corresponds to the strain sensitivity dependence of -1.99×10^{-2} dB/%/m and the temperature sensitivity dependence of -5.22×10^{-4} dB/°C/m. Subsequently, we measured the spectral power dependence on sensing position when the temperature of the POF was locally changed to 60°C. The spectral powers were measured when 1.0-m-long sections (4 sections; 2.0–3.0, 5.0–6.0, 8.0–9.0, 11.0–12.0 m distant from the proximal POF end) were heated, and plotted as functions of temperature (Fig. 4.19(b)). The measured data were in good agreement with the theoretical trends (indicated by dotted lines) obtained from the BGS distributions (Fig. 4.18). The spectral powers were almost linearly dependent on temperature, and their coefficients were found to decrease with increasing distance from the proximal POF end. For each section, the temperature sensitivity was calculated and plotted as a function of sensing position (Fig. 4.19(c)).

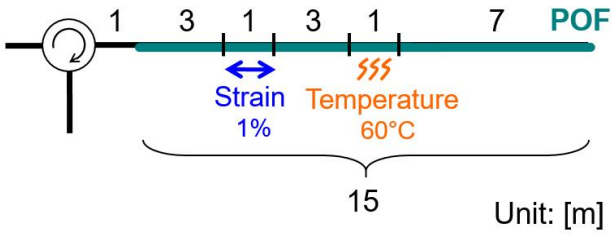

(a)

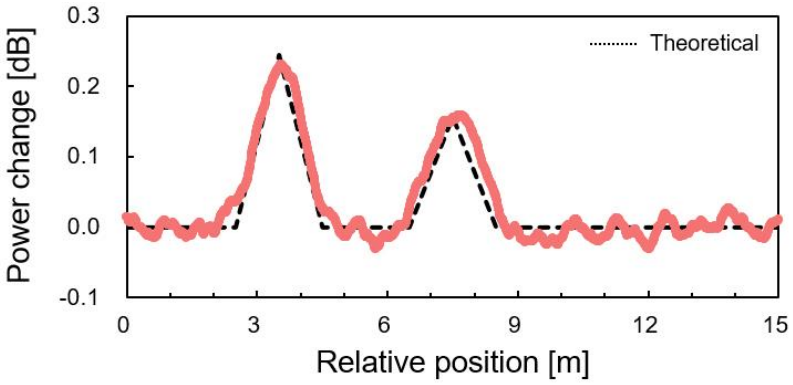

(b)

Fig. 4.20 (a) Structure of the fiber under test for final demonstration. (b) Power-change distributions along the FUT. The dotted line is a theoretical trend.

The dependence coefficient was $–4.98\times10^{–4}$ dB/°C/m (corresponding to $–2.10\times10^{–2}$ dB/%/m for strain), which is in good agreement with the theoretical value calculated from the BGS distribution ($–5.22\times10^{–4}$ dB/°C/m).

Lastly, distributed measurement of strain and temperature along the POF was demonstrated using SA-BOCDR. Using the FUT depicted in Fig. 4.20(a), a 1.0-m-long section was strained for 1 %, and another 1.0-m-long section was heated to 60 °C. The measured power-change distribution is shown in Fig. 5(b). At the expected sections, the power changes corresponding to the strain and the temperature change were observed, which moderately agrees with the theoretical dotted line considering the sensitivity dependence on sensing position and the trapezoidal effect of SA-BOCDR. Thus, the applied strain and temperature change were correctly detected. The measurement errors originate from the signal fluctuations caused by the low SNR, which can be improved by increasing the number of averaging, increasing the pump power, or optimizing the low-pass filtering function of the ESA.

4. 4. 5 Conclusion

We investigated the influences of high-loss POFs (~250 dB/km at 1550 nm) on SA-BOCDR. Due to the gradual reduction of transmitted power in the POFs, the measurement sensitivities are found to depend on sensing position, unlike the case of standard silica fiber-based configurations. This unique effect is studied both theoretically and experimentally. The dependence coefficients were $–2.10\times10^{–2}$ dB/%/m for strain and $–4.98\times10^{–4}$ dB/°C/m for temperature, which agreed well with the theoretical predictions. Furthermore, a correct POF-based distributed measurement is performed with a resolution of ~1 m by compensating this effect. We believe that these results will be an important basis in implementing high-loss fibers to SA-BOCDR, especially POFs, which allows high flexibility and high temperature sensitivity.

5 Pseudo-field test

In this Chapter, as a first step toward practical applications, we present an example of SA-BOCDR-based diagnosis using a composite structure with carbon fiber-reinforced plastics. After preparing a specimen using a so-called vacuum-assisted resin transfer molding technique, we apply load to the structure on its top or bottom using a three-point bending device. Then, we measured strain distributions along the embedded optical fiber and show that the system's output agrees well with the actual strain distributions. We also detect the breakage of the embedded fiber by applying large strains to the structure.

5. 1 Preface

We developed a new structural health monitoring technique, named SA-BOCDR to achieve real-time distributed strain, temperature, and even loss measurements along optical fibers. The basic operational principle of SA-BOCDR has been well clarified with some unique features and system performances, such as stability, sensitivity, strain dynamic range, and robustness have been improved. However, measurements using optical fibers embedded in actual structures need to be provided to employ the system to practical applications.

As a first step toward such practical applications, in this section, we present an example of SA-BOCDR-based diagnosis using an optical fiber embedded in a composite structure. As a specimen to be measured, we prepared a carbon fiber-reinforced plastic (CFRP) [95–96] strengthened steel plate, in which a standard silica SMF was embedded. As load was applied to the structure on its top or bottom, we detect the induced compressive and tensile strain distributions, respectively. We show that the breakage of the embedded fiber can also be detected as an abrupt local power change in the SA-BOCDR output.

5. 2 Fabrication of specimen

Owing to their high strength, high elastic modulus, light weight, and high corrosion resistance, CFRPs have been widely used as materials for repairing or strengthening steel structures [98]. In this experiment, as a specimen, a CFRP-strengthened steel plate was prepared using a so-called vacuum-assisted resin transfer molding (VaRTM) technique [99, 100], which is known as an advanced, highly reliable, and reproducible method for the fabrication of composite materials. The VaRTM process [99] is schematically shown in Fig. 5.1. The process was conducted by infusing a liquid resin into laminated fibers or woven fabrics using a pressure differential between the atmosphere and vacuum; thereafter, the resin was hardened by heat. This technique does not require a prepreg or an autoclave, yielding highly efficient fabrication of composite materials.

Figure 5.2 shows the structure of the specimen. A 1.4-m-long silica SMF with BFS of 10.85 GHz at room temperature (23 °C) was, as a sensing fiber, embedded between a steel plate and CFRP strips (containing carbon fiber cloth (UM46-40G, Torayca). This

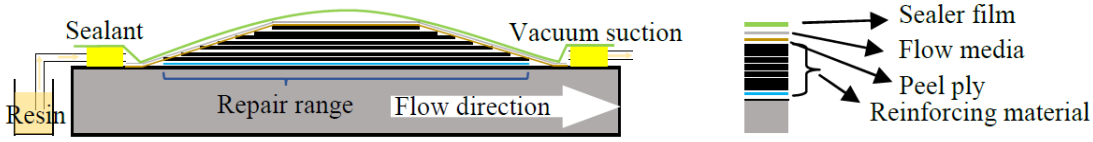

Fig. 5.1 Schematic of the VaRTM process (adapted from Ref. 99).

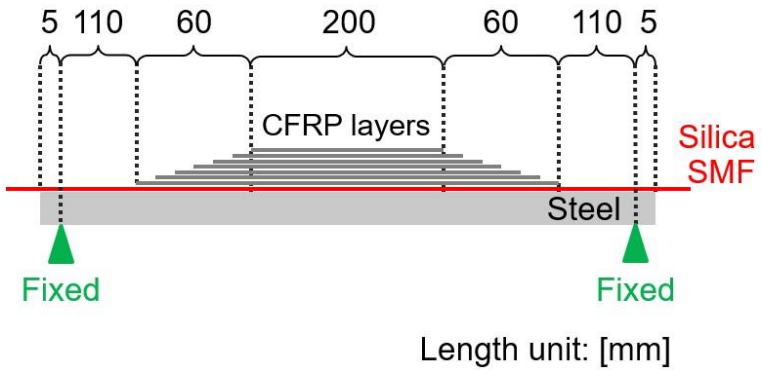

Fig. 5.2 Structure of the specimen.

structure was fabricated by placing the SMF before the infusing liquid resin during the VaRTM process. The depth of the structure (both the steel plate and the CFRP strips) was 39 mm, and the thickness of the steel plate was 12 mm. The total thickness of the CFRP strips composed of seven tapered layers (the length of each strip differed by 10 mm) was ~3 mm.

5. 3 Experimental conditions

Figure 5.3 shows the experimental setup of SA-BOCDR for measuring the strain distributions along the sensing fiber. The 1550-nm light from a semiconductor laser was divided into two light beams: incident and reference. After passing through a PSCR, the incident light was amplified to ~28 dBm using an EDFA and injected into the sensing fiber embedded in the specimen. In the meantime, the reference light was guided to a 1-km-long delay fiber, amplified to ~3 dBm, and then heterodyned with the Stokes light (Brillouin-scattered from the sensing fiber; amplified to ~1 dBm). The heterodyned optical signal was converted into an electrical signal using a PD, and amplified by 23 dB using an electrical amplifier to improve the SNR. Thereafter, the spectral power change at a fixed frequency ν_{B0} (= 10.83 GHz) of the BGS was acquired using the narrow band-pass filtering function of an ESA and observed using an OSC. The video and resolution bandwidths of the ESA were 3 kHz and 10 MHz, respectively. Averaging was performed 1024 times to enhance the SNR.

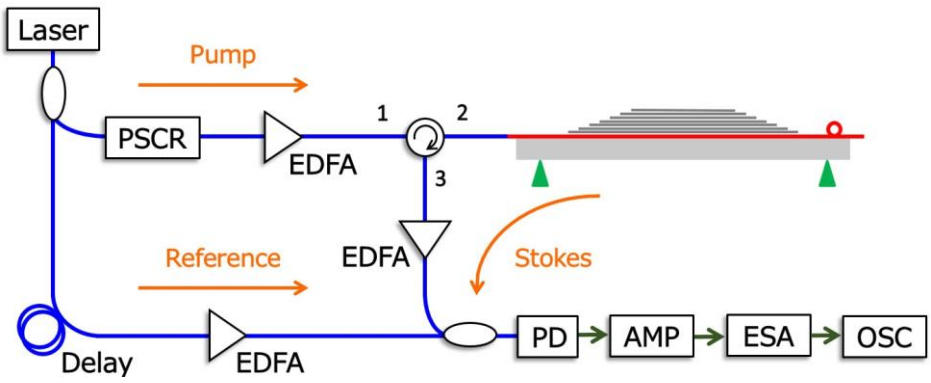

Fig. 5.3 Experimental setup for SA-BOCDR. EDFA, erbium-doped fiber amplifier; ESA, electrical spectrum analyzer; OSC, oscilloscope; PD, photo detector; PSCR, polarization scrambler.

To resolve the sensing locations, the laser output frequency was sinusoidally modulated and a so-called correlation peak was generated in the sensing fiber. By sweeping the modulation frequency f_m (= 9.132–9.156 MHz), the correlation peak was scanned along the fiber, enabling a distributed measurement. The measurement range d_m was 11.3 m, which was determined by f_m. By setting the modulation amplitude Δf to 1.52 GHz, the spatial resolution of the system was 7.1 cm.

We performed two different types of experiments: one for evaluating the magnitude of tensile and compressive strains applied to the sensing fiber, and the other for detecting the breakage of the fiber. First, using a three-point bending device (Fig. 5.4), tensile and compressive strains were applied to the middle of the specimen by tightening the top screw with a pitch of 2 mm (the specimen was upturned when tensile strains were applied). We measured the distributed tensile and compressive strains from 0 to 1.5 and from 0 to 2.5 turns (of the top screw), respectively. Measurements were performed every 0.5 turns. According to our calculation based on the finite-element analysis, the strain increases by ~400 με with each additional turn, leading to the applied strains of approximately 0, 200, 400, and 600 με (for tensile strains) and 0, 200, 400, 600, 800, and 1000 με (for compressive strains).

Similar experiments were performed by applying larger compressive strains to the specimen until the sensing fiber was broken. Using SA-BOCDR, the power-change distributions were measured while the top screw was tightened from 0 to 6.0 turns, correspo nding to strains of 0 to ~2400 με. Throughout the measurements, the room temperature was 23 °C.

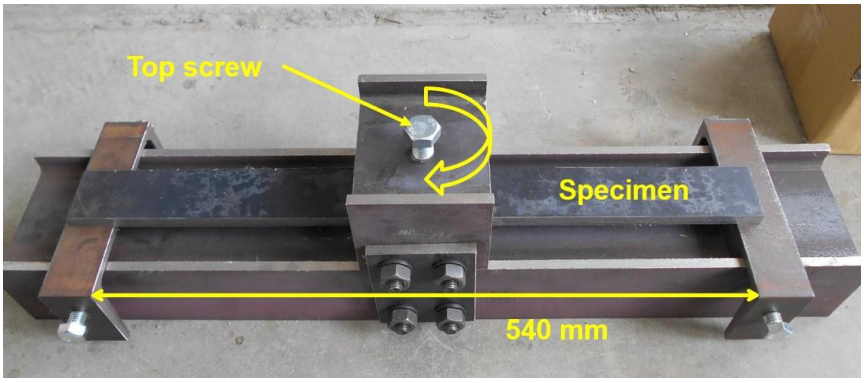

Fig. 5.4 Three-point bending device.

5. 4 Experimental results

5. 4. 1 Strain distribution measurements

First, we present the experimental results of evaluating the magnitude of the applied tensile and compressive strains. Figure 5.5(a) shows the measured power-change distributions along the whole sensing fiber when tensile strains of 0, 200, 400, and 600

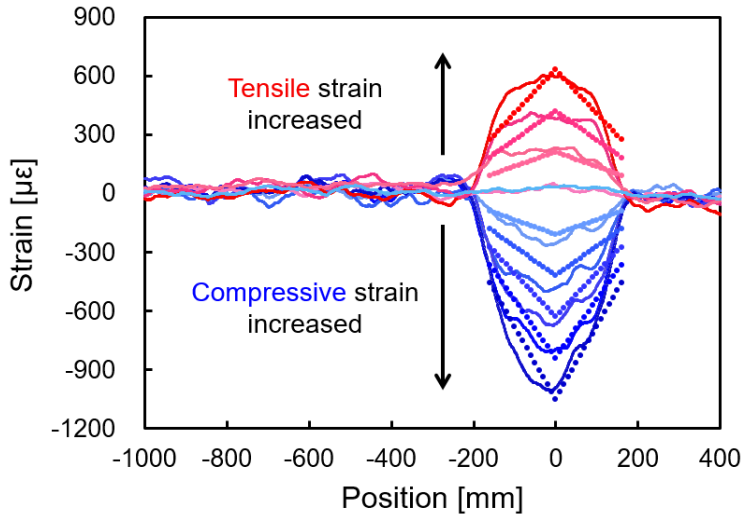

(a)

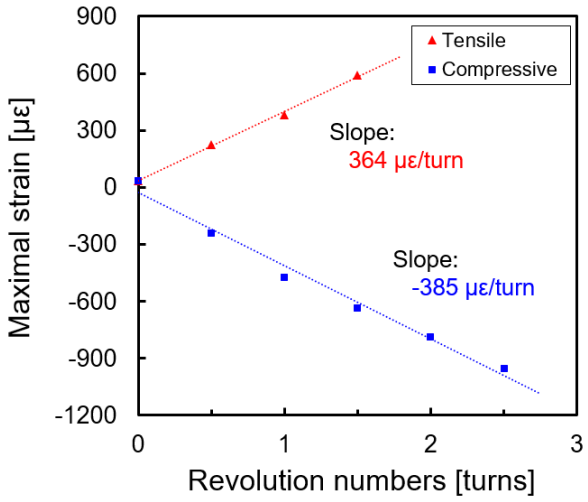

(b)

Fig. 5.5 (a) Strain distributions along the sensing fiber measured when the tensile strains of 0, 200, 400, and 600 με and the compressive strains of 0, 200, 400, 600, 800, and 1000 με were applied. The dotted lines indicate the theoretical trends. (b) Maximal tensile and compressive strains (derived from (a)) plotted in terms of the revolution numbers of the top screw.

με and compressive strains of 0, 200, 400, 600, 800, and 1000 με were applied to the specimen. The vertical axis was converted into strain using the known strain-dependence coefficient of a power change of –1.59 dB/%. Note that the positive and negative signs indicate tensile and compressive strains, respectively. The horizontal axis indicates the relative distance from the midpoint of the embedded section of the sensing fiber (positive values correspond to distal locations). The power changes were observed along a ~390-mm-long section around the embedded section. Note that the actually embedded length of the sensing fiber was ~320 mm; the ~70-mm difference corresponds to the nominal spatial resolution. With increasing applied tensile and compressive strains, the measured strains also increased moderately in accordance with the theoretical values (shown by dotted lines; which are not theoretical SA-BOCDR outputs but theoretical strain distributions). In Fig. 5.5(b), the maximal strain obtained from each measured distribution in Fig. 5.5(a) is plotted as a function of the number of revolutions of the top screw. Irrespective of tensile or compressive strains, the maximal strain increased almost linearly with increasing the number of revolutions of the screw. The calculated slopes for tensile and compressive strains were ~364 με/turn and ~385 με/turn, respectively, in a moderate agreement with theoretical values (~400 με/turn). The discrepancy seems to be caused by the insufficient adhesion strength of the sensing fiber.

5. 4. 2 Fiber breakage detection

Subsequently, we detected the breakage of the sensing fiber by applying larger compressive strains to the specimen. The top screw was tightened to 0, 1.5, 3.0, 4.5, 5.3, 5.5, and 6.0 turns. The measured distributions of the power change are shown in Fig. 5.6. The vertical axis was defined to be positive when the strain was compressive. When the number of revolutions was equal to or smaller than 4.5, the power changes were observed along the correct section. In this range of strains, the power change was almost proportional to the number of revolutions. However, when the number of revolutions was larger than 5.3 (~2120 με), the power change showed a drastic increase along the distal side from the midpoint of the specimen. This behavior implies that considerable optical loss was induced, possibly by fiber breakage. Figure 5.7 shows the photographs of the specimen after the revolution number of 6.0 turns was applied. Part of the CFRP strips were clearly peeled off from the steel. These results indicate that SA-BOCDR has the

capability to indirectly predict the peeling of composite structures via fiber breakage detection.

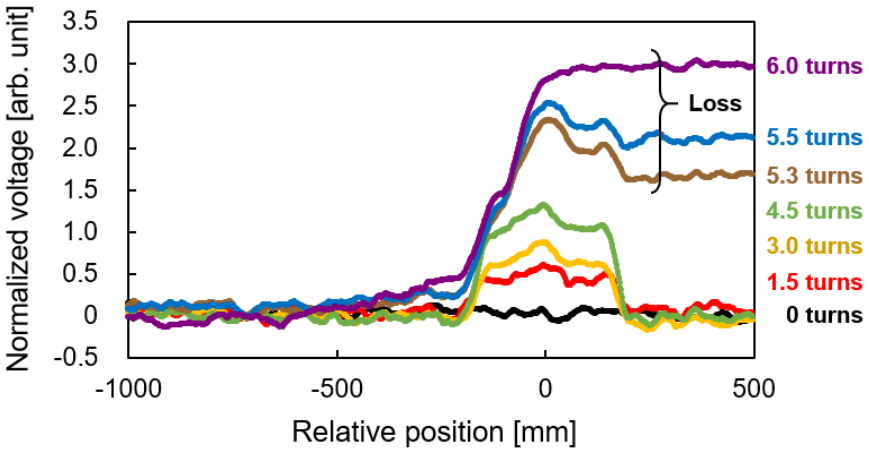

Fig. 5.6 Power-change distributions along the sensing fiber measured when the compressive strains were applied until the fiber was broken.

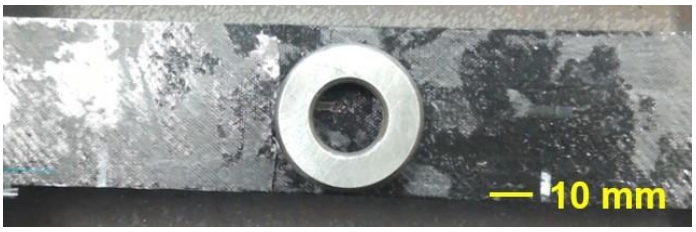

(a)

(b)

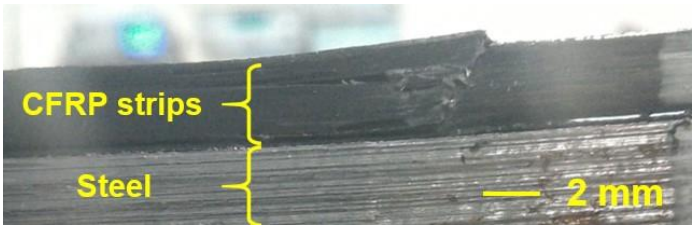

(c)

Fig. 5.7 Photographs of the CFRP strips peeled off from the steel; (a) top view, (b, c) side views.

5. 4 Discussions

In this section, for the user's sake, we make a discussion on how to determine the experimental parameters in SA-BOCDR under the given conditions, such as the frequency span (i.e., strain range), measurement range, spatial resolution, and repetition rate. First of all, the modulation frequency f_m and amplitude Δf should be fixed to a certain value using Eqs. (1-1) and (1-2). Then, the BGS of the sensing fiber at room temperature needs to be obtained to optimize the linear range and ν_{B0}. In most cases, the linear range is almost the same as the strain dynamic range of the system.

The parameters also can be determined in the same manner even when the several sensing fibers with different BFSs are connected each other. Since SA-BOCDR (or standard BOCDR) allows random access to any sensing position in the sensing fiber, unlike time-domain schemes, accurate distributed measurement can be performed along different fibers with different BFSs by controlling the modulation frequency f_m.

5. 5 Conclusion

In conclusion, we experimentally investigated the strain distributions along the sensing fiber embedded in the CFRP-strengthened steel plate. The measured tensile and compressive strains were shown to be linearly dependent on the number of revolutions of the top screw. The dependence coefficients were ~364 με/turn for tensile strain and ~385 με/turn for compressive strain, which were in moderate agreement with the theoretical values. We also detected the breakage of the embedded sensing fiber when large compressive strains were applied. The optical loss appeared when the screw was tightened to 5.3 turns (~2120 με), and the embedded sensing fiber was completely broken at 6.0 turns (~2400 με). We believe that, by presenting a promising example of composite structural diagnosis, this work will provide an important basis for the future development of SA-BOCDR-based health monitoring systems for practical applications.

6 Conclusions

To achieve real-time distributed strain, temperature, and even loss measurements with single-end accessibility and a high spatial resolution, in this thesis, we proposed a new configuration of Brillouin optical correlation-domain reflectometry (BOCDR)—named slope-assisted (SA-) BOCDR—which operates with the assistance of the slope of the Brillouin gain spectrum (BGS). In this method, instead of observing the whole BGS, we detect the spectral power at a certain frequency on a linear range of BGS, which enables a higher sampling rate. After carefully investigating its operation with some unique features, performance improvements were performed toward practical applications. Finally, some pseudo-field tests were conducted using a silica-fiber-embedded composite structure to show the practical usefulness of the system.

In Chapter 1: "Introduction," the basic concepts of optical fibers and optical fiber sensors were described. We also explained the principle of Brillouin scattering for sensing applications. Furthermore, conventional Brillouin-based fiber-optic distributed sensors are briefly reviewed. The purpose of this thesis is also presented including the necessity of high-speed BOCDR.

In Chapter 2: "Proposal of slope-assisted (SA-) BOCDR," the principle of SA-BOCDR was presented. After explaining that the system can achieve a higher sampling rate by detecting the spectral power at a certain frequency on a linear region of BGS, we also showed that, unlike difficult in standard (frequency-based) BOCDR, newly developed SA-BOCDR can provide loss distribution along the sensing fiber, because it operates based on power information. The basic operation of the system was then verified through simultaneous distributed measurement of strain, temperature, and loss with a high sampling rate.

In Chapter 3: "Characterization," we presented the detailed operation of SA-BOCDR with some unique features. First, the relationship between the final system output and

actual Brillouin frequency shift distribution along the fiber under test (FUT) was investigated both theoretically and experimentally. As a result, we found that SA-BOCDR has a unique ability to detect hotspots even shorter than the nominal spatial resolution. This “beyond-nominal-resolution” effect was well clarified, and using this effect, we successfully detected world’s shortest strained and heated sections both in silica and polymer optical fibers. Following these works, we showed the influences of the experimental conditions (incident power and spatial resolution) on the measurement sensitivity of the system, which can provide a useful guideline in setting the experimental conditions of SA-BOCDR. Finally, considering some practical applications, a long-distance measurement with a > 10-km range was also demonstrated. To achieve such a long measurement range, it was found that the length of the delay line in a reference path should be at least four times longer than the FUT. In addition, we also showed that unintended forward-propagating Brillouin-scattered light in the reference path should be suppressed to obtain high signal-to-noise ratio of the system. A 3-m-long heated section in a 13-km-long silica fiber was then detected in a distributed manner by exploiting aforementioned “beyond-nominal-resolution” effect.

In Chapter 4: “Performance improvements,” the experimental results for the enhancement of stability, sensitivity, strain dynamic range, and robustness were provided. To start with, we eliminated the loss sensitivity of SA-BOCDR for stable strain and temperature measurements using a trench-index-type special silica fiber with low bending loss. Then, the stability of SA-BOCDR was also enhance by mitigating polarization-dependent power fluctuations by employing polarization-maintaining fibers (PMFs). We also showed that PMF-based SA-BOCDR can provide a higher measurement sensitivity than silica-fiber-based systems by optimizing polarization states. Subsequently, the strain dynamic range was enhanced by investigating its trade-off relation to the spatial resolution. After showing that the unique bell-shaped background noise, which is unavoidable in BOCDR systems, was the origin of this limitation, we investigated the trade-off relation between the strain dynamic range and the spatial resolution of the system. As a result, we achieved the strain dynamic range ~3 times wider than that previously reported at the cost of lowered spatial resolution. Finally, polymer optical fibers (POFs) were employed to enhance the robustness of the system. Due to their high propagation loss, the measurement sensitivity was found to be

a function of the sensing location in the POF. Thus, we demonstrated POF-based distributed measurements by compensating this effect.

In Chapter 5: “Pseudo-field test,” the relevance of SA-BOCDR was evaluated by providing an example of structural health monitoring using a composite structure, in which a standard silica fiber is embedded. After preparing a specimen (a carbon-fiber-reinforced-plastic strengthened steel plate), we induced tensile and compressive strains to the embedded fibers by applying load to the structure using a three-point bending device and conducted distributed strain measurements. The obtained results moderately agreed with the theoretical trends. In addition, we performed similar experiments by applying larger strains until the sensing fiber is broken and showed SA-BOCDR can indirectly predict the peeling of the composite structures by detecting the breakage of the embedded fiber.

Finally, we would like to make a conclusion by discussing how to use SA-BOCDR in practice. Standard BOCDR and SA-BOCDR have their own merits and demerits. For example, standard BOCDR has a relatively high measurement accuracy, but their operation speed has been limited due to the necessity of acquisition of the whole BGS. On the other hand, SA-BOCDR has a relatively low measurement accuracy since it works based on power information, however, real-time distributed measurement is feasible in SA-BOCDR. In addition, the unique feature called beyond-nominal-resolution effect is highly useful in many practical cases. Thus, these two systems should be switched according to applications. Since standard BOCDR and SA-BOCDR is composed of extremely similar setup, they are expected to be switched easily and instantaneously only with a simple action.

Abbreviations

BFS	Brillouin frequency shift
BGS	Brillouin gain spectrum
BOCDA	Brillouin optical correlation-domain analysis
BOCDR	Brillouin optical correlation-domain reflectometry
BOFDA	Brillouin optical frequency-domain analysis
BOFDR	Brillouin optical frequency-domain reflectometry
BOTDA	Brillouin optical time-domain analysis
BOTDR	Brillouin optical time-domain reflectometry
CFRP	carbon fiber-reinforced plastic
EDFA	erbium-doped fiber amplifier
ESA	electrical spectrum analyzer
FUT	fiber under test
LD	laser diode
OSC	oscilloscope
PANDA	polarization-maintaining and absorption-reducing
PD	photodiode
PFGI-POF	perfluorinated graded-index polymer/plastic optical fiber

PMF	polarization-maintaining fiber
POF	polymer/plastic optical fiber
PSCR	polarization scrambler
RBW	radio bandwidth
SA-BOCDR	slope-assisted Brillouin optical correlation-domain reflectometry
SMF	single-mode fiber
SNR	signal-to-noise ratio
SOP	state of polarization
VaRTM	vacuum-assisted resin transfer molding
VBW	video bandwidth

Acknowledgements

It would not have been possible to write this dissertation without the help and support of the kind people around me, to only some of whom it is possible to give particular mention here.

Above all, I would like to express my deepest gratitude to my supervisor, Professor Kentaro Nakamura, for providing me this precious opportunity to study in his laboratory. The completion of this work could not have been possible without his continuous guidance, considerate encouragement, and invaluable discussion, not to mention his unsurpassed knowledge of ultrasonic and optical technology.

I also would like to express my sincere appreciation to Assistant Professor Yosuke Mizuno for his minute guidance, warm encouragement, and help throughout the course of this work. Especially, I appreciate his instruction related to logical thinking, paper writing skills, presentation techniques, and knowledge on nonlinear optics.

I also gratefully acknowledge the members of my thesis committee, Professor Hiroyuki Uenohara, Professor Kotaro Kajikawa, Professor Masahiro Yamaguchi, and Professor Tomoyuki Miyamoto.

I am extremely grateful to all the members in Nakamura Laboratory for their feedback, cooperation, and of course friendship. Furthermore, I am grateful to the secretary of the laboratory Ms. Mayumi Azuma for her kind help in various aspects.

I would like to acknowledge to Professor Fumio Koyama and Professor Hiroyuki Uenohara for providing many devices and fibers, which are indispensable in this work. In addition, my heartfelt appreciation also goes to Prof. Yosuke Tanaka, Prof. Hitoshi Nakamura, Assoc. Prof. Yukihiro Matsumoto, Mr. Yutaka Ochi, and Mr. Takahiro Matsui for providing valuable advices and for preparing a specimen during the collaborative research period.

Of course, I greatly appreciate my friends for all the good times we have had together. I take this opportunity to record my thanks to them for their listening and careful advice.

Last but not the least, I would like to express my indebtedness to my loving family: my parents and my sister for their understanding, continuous support and love they have given me. I could not have done this work without them. Also, Janggun and Mung deserve a special thanks for cheering me up.

August, 2019 Heeyoung Lee

References

[1] K. C. Kao and G. A. Hockham, “Dielectric-fibre surface waveguides for optical frequencies,” IEEE Proc. **113**(7), 1151 (1966).

[2] H. Lamm, “Biegsame optische gerate,” Z. Instrumenten. **50**, 579 (1930).

[3] A. C. S. van Heel, “A new method of transporting optical images without aberrations,” Nature **173**(4392), 39 (1954).

[4] H. H. Hopkins and N. S. Kapany, “Transparent fibres for the transmission of optical images,” Optica Acta **1**(4), 164 (1955).

[5] F. P. Kapron, D. B. Keck, and R. D. Maurer, “Radiation losses in glass optical waveguides,” Appl. Phys. Lett. **17**(10), 423 (1970).

[6] W. G. French, J. B. MacChesney, P. B. O’Connor, and G. W. Tasker, “Optical waveguides with very low loss,” Bell Syst. Tech. J. **53**(5), 951 (1974).

[7] T. Miya, Y. Terunuma, T, Hosaka, and T, Miyashita, “Ultimate low-loss single-mode fiber at 1.55 μm,” Electron. Lett. **15**(4), 106 (1979).

[8] R. Ramaswani and K. Sivarajan, *Optical Networks: A Practical Perspective*, 2nd ed. (Morgan Kaufmann Publishers, San Francisco, 2002).

[9] G. P. Agrawal, *Fiber-Optic Communication Systems*, 3rd ed. (Wiley, New York, 2002).

[10] I. P. Kaminow and T. Li, Eds., *Optical Fiber Telecommunications*, Vols. 4A and 4B (Academic Press, Boston, 2002).

[11] D. Davies and S. A. Kingsley, “The use of optical fibers as instrumentation transducers,” Proc. CLEO’76, **24**, 1976.

[12] V. Vali and R. W. Shorthill, “Fiber ring interferometer,” Appl. Opt. **15**(5), 1099 (1976).

[13] E. Udd, *Fiber Sensors* (Wiley, New York, 1991).

[14] C. Menadier, C. Kissinger, and H. Adkins, “The fotonic sensor”, Instrum. & Control Syst. **40**, 114 (1967).

[15] Y. Koike, E. Nihei, N. Tanio, and Y. Ohtsuka, “Graded-index plastic optical fiber composed of methyl methacrylate and vinyl phenylacetate copolymers,” Appl. Opt. **29**(18), 2686 (1990).

[16] T. Ishigure, Y. Koike, and J. W. Fleming, “Optimum index profile of the perfluorinated polymer-based GI polymer optical fiber and its dispersion properties,” J. Lightwave Technol. **18**(2), 178 (2000).

[17] I. Mollers, D. Jager, R. Gaudino, A. Nocivelli, H. Kragl, O. Ziemann, N. Weber, T. Koonen, C. Lezzi, A. Bluschke, and S. Randel, "Plastic optical fiber technology for reliable home networking: overview and results of the EU project pof-all," IEEE Commun. Magazine **47**(8), 58 (2009).

[18] S. Liehr, P. Lenke, M. Wendt, K. Krebber, M. Seeger, E. Thiele, H. Metschies, B. Gebreselassie, and J.C. Munich, "Polymer Optical Fiber Sensors for Distributed Strain Measurement and Application in Structural Health Monitoring," IEEE Sensors J. **9**(11), 1330 (2009).

[19] K. Nakamura, I. R. Husdi, and S. Ueha, “A distributed strain sensor with the memory effect based on the POF OTDR,” Proc. SPIE **5855**, 807 (2005).

[20] K. Minakawa, N. Hayashi, Y. Mizuno, and K. Nakamura, “Thermal memory effect in polymer optical fibers,” IEEE Photon. Technol. Lett. **27**(13), 1394 (2015).

[21] D. Inaudi, A. Ruefenacht, B. von Arx, H. P. Noher, S. Vurpillot, and B. Glisic, “Monitoring of a concrete arch bridge during construction,” Proc. SPIE **4696**, 146 (2002).

[22] K. Hotate, “Fiber distributed Brillouin sensing with optical correlation domain techniques,” Optical Fiber Technology (Elsevier Inc.), **19**(6), Part B, 700 (2013).

[23] K. Hotate: “Distributed fiber sensing technology: Currents and challenges,” Optica Pura Aplicada. **45**(2), 63 (2012).

[24] G. P. Agrawal, *Nonlinear Fiber Optics*, 2nd ed. (Academic Press, New York, 1995).

[25] T. Horiguchi, T. Kurashima, and M. Tateda, “Tensile strain dependence of Brillouin frequency shift in silica optical fibers,” IEEE Photon. Technol. Lett. **1**(5), 107 (1989).

[26] T. Kurashima, M. Tateda, and M. Tateda, “Thermal effects on the Brillouin frequency shift in jacketed optical silica fibers,” Appl. Opt. **29**(15), 2219 (1990).

[27] K. Hotate and K. Kajiwara, “Proposal and experimental verification of Bragg wavelength distribution measurement within a long-length FBG by synthesis of optical coherence function,” Opt. Express **16**(11), 7881 (2008).

[28] A. Wada, K. Ikuma, M. Syoji, S. Tanaka, and N. Takahashi, “Wide-dynamic-range high-resolution fiber fabry-perot interferometric sensor with chirped fiber Bragg gratings,” J. Lightwave Technol. **31**(19), 3176 (2013).

[29] Y. Nakazaki and S. Yamashita, “Fast and wide tuning range wavelength-swept fiber laser based on dispersion tuning and its application to dynamic FBG sensing,” Opt. Express **17**(10), 8310 (2009).

[30] T. Horiguchi and M. Tateda, “BOTDA-nondestructive measurement of single-mode optical fiber attenuation characteristics using Brillouin interaction: Theory,” J. Lightwave Technol. **7**(8), 1170 (1989).

[31] X. Tu, H. Luo, Q. Sun, X. Hu, and Z. Meng, “Performance analysis of slope-assisted dynamic BOTDA based on Brillouin gain or phase-shift in optical fibers,” J. Opt. **17**(10), 105503 (2015).

[32] Z. Li, L. Yan, L. Shao, W. Pan, B. Luo, J. Liang, and H. He, “Coherent BOTDA sensor with single-sideband modulated probe light,” IEEE Photon. J. **8**(1), 6800908 (2016).

[33] W. Li, X. Bao, Y. Li, and L. Chen, “Differential pulse-width pair BOTDA for high spatial resolution sensing,” Opt. Express **16**(26), 21616 (2008).

[34] Y. Dong, D. Ba, T. Jiang, D. Zhou, H. Zhang, C. Zhu, Z. Lu, H. Li, L. Chen, and X. Bao, “High-spatial-resolution fast BOTDA for dynamic strain measurement based on differential double-pulse and second-order sideband of modulation,” IEEE Photon. J. **5**(3), 2600407 (2013).

[35] Y. Peled, A. Motil, I. Kressel, and M. Tur, “Monitoring the propagation of mechanical waves using an optical fiber distributed and dynamic strain sensor based on BOTDA,” Opt. Express **21**(9), 10697 (2013).

[36] A. Minardo, R. Bernini, and L. Zeni, “Numerical analysis of single pulse and differential pulse-width pair BOTDA systems in the high spatial resolution regime,” Opt. Express **19**(20), 19233 (2011).

[37] Y. Dong, L. Chen, and X. Bao, “Time-division multiplexing-based BOTDA over 100 km sensing length,” Opt. Lett. **36**(2), 277 (2011).

[38] X. Tu, H. Luo, Q. Sun, X. Hu, and Z. Meng, “Performance analysis of slope-assisted dynamic BOTDA based on Brillouin gain or phase-shift in optical fibers,” J. Opt. **17**(10), 105503 (2015).

[39] M. A. Soto, S. L. Floch, and L. Thévenaz, “Bipolar optical pulse coding for performance enhancement in BOTDA sensors,” Opt. Lett. **21**(14), 16390 (2013).

[40] I. Sovran, A. Motil, and M. Tur, “Frequency-scanning BOTDA with ultimately fast acquisition speed,” IEEE Photon. Technol. Lett. **27**(13), 1426 (2015)

[41] T. Kurashima, T. Horiguchi, H. Izumita, S. Furukawa, and Y. Koyamada, “Brillouin optical-fiber time domain reflectometry,” IEICE Trans. Commun. **E76B**(4), 382 (1993).

[42] D. Iida and F. Ito, “Detection sensitivity of Brillouin scattering near Fresnel reflection in BOTDR measurement,” J. Lightwave Technol. **26**(4), 417 (2008).

[43] M. Ohsaki, M. Tateda, T. Omatsu, and H. Ohno, “Spatial resolution enhancement of distributed strain measurement using BOTDR by partially gluing optical fiber,” IEICE Trans. Commun. **E85-B**(8), 1636 (2002).

[44] N. Nitta, M. Tateda, and T. Omatsu, “Spatial resolution enhancement in BOTDR by spectrum separation method,” Opt. Rev. **9**(2), 49 (2002).

[45] Q. Li, J. Gan, Y. Wu, Z. Zhang, J. Li, and Z. Yang, “High spatial resolution BOTDR based on differential Brillouin spectrum technique,” IEEE Photon. Technol. Lett. **28**(14), 1493 (2016).

[46] F. Wang, W. Zhan, X. Zhang, and Y. Lu, “Improvement of spatial resolution for BOTDR by iterative subdivision method,” J. Lightwave Technol. **31**(23), 3663 (2013).

[47] Y. Koyamada, Y. Sakairi, N. Takeuchi, and S. Adachi, “Novel technique to improve spatial resolution in Brillouin optical time-domain reflectometry,” IEEE Photon. Technol. Lett. **19**(23), 1910 (2007).

[48] D. Garus, K. Krebber, and F. Schliep, “Distributed sensing technique based on Brillouin optical-fiber frequency-domain analysis,” Opt. Lett. **21**(17), 1402 (1996).

[49] R. Bernini, A. Minardo, and L. Zeni, “Distributed sensing at centimeter-scale spatial resolution by BOFDA: Measurements and signal processing,” IEEE Photon. J. **4**(1), 48 (2012).

[50] A. Minardo, R. Bernini, R. Ruiz-Lombera, J. Mirapeix, J. M. Lopez-Higuera, and

L. Zeni, “Proposal of Brillouin optical frequency-domain reflectometry (BOFDR),” Opt. Express **24**(26), 29994 (2016).

[51] K. Hotate and T. Hasegawa, “Measurement of Brillouin gain spectrum distribution along an optical fiber using a correlation-based technique—proposal, experiment and simulation—,” IEICE Trans. Electron. **E83-C**(3), 405 (2000).

[52] J. H. Jeong, K. H. Chung, S. B. Lee, K. Y. Song, J. M. Jeong, and K. Lee, “Linearly configured BOCDA system using a differential measurement scheme,” Opt. Express **22**(2), 1467 (2014).

[53] R. Cohen, Y. London, Y. Antman, and A. Zadok, “Brillouin optical correlation domain analysis with 4 millimeter resolution based on amplified spontaneous emission,” Opt. Express **22**(10), 12070 (2014).

[54] C. Zhang, M. Kishi, and K. Hotate, “5,000 points/s high-speed random accessibility for dynamic strain measurement at arbitrary multiple points along a fiber by Brillouin optical correlation domain analysis,” Appl. Phys. Express **8**(4), 042501 (2015).

[55] K. Y. Song, Z. He, and K. Hotate, “Distributed strain measurement with millimeter-order spatial resolution based on Brillouin optical correlation domain analysis,” Opt. Lett. **31**(17), 2526 (2006).

[56] W. Zou, C. Jin, and J. Chen, “Distributed strain sensing based on combination of Brillouin gain and loss effects in Brillouin optical correlation domain analysis,” Appl. Phys. Express **5**(8), 082503 (2012).

[57] K. Y. Song, M. Kishi, Z. He, and K. Hotate, “High-repetition-rate distributed Brillouin sensor based on optical correlation-domain analysis with differential frequency modulation,” Opt. Lett. **36**(11), 2062 (2011).

[58] E. Preter, et al.: “High-resolution Brillouin optical correlation domain analysis with no spectral scanning,” Opt. Exp. **24**(24), 27253 (2016).

[59] K. Y. Song, Z. He, and K. Hotate, “Effects of intensity modulation of light source on Brillouin optical correlation domain analysis,” J. Lightwave Technol. **25**(5), 1238 (2007).

[60] Y. H. Kim, K. Lee, and K. Y. Song, “Brillouin optical correlation domain analysis with more than 1 million effective sensing points based on differential measurement,” Opt. Express **23**(26), 33241 (2015).

[61] Y. Mizuno, W. Zou, Z. He, and K. Hotate, "Proposal of Brillouin optical correlation-domain reflectometry," Opt. Express **16**(16), 12148 (2008).

[62] Y. Mizuno, W. Zou, Z. He, and K. Hotate, "Operation of Brillouin optical correlation-domain reflectometry: Theoretical analysis and experimental validation," J. Lightwave Technol. **28**(22), 3300 (2010).

[63] N. Hayashi, Y. Mizuno, and K. Nakamura, "Simplified Brillouin optical correlation-domain reflectometry using polymer optical fiber," IEEE Photon. J. **7**(1), 6800407 (2015).

[64] Y. Mizuno, Z. He, and K. Hotate, "One-end-access high-speed distributed strain measurement with 13-mm spatial resolution based on Brillouin optical correlation-domain reflectometry," IEEE Photon. Technol. Lett. **21**(7), 474 (2009).

[65] Y. Mizuno, Z. He, and K. Hotate, "Measurement range enlargement in Brillouin optical correlation-domain reflectometry based on temporal gating scheme," Opt. Express **17**(11), 9040 (2009).

[66] Y. Mizuno, Z. He, and K. Hotate, "Measurement range enlargement in Brillouin optical correlation-domain reflectometry based on double-modulation scheme," Opt. Express **18**(6), 5926 (2010).

[67] Y. Mizuno, Z. He, and K. Hotate, "Distributed strain measurement using a tellurite glass fiber with Brillouin optical correlation-domain reflectometry," Opt. Commun. **283**(11), 2438 (2010).

[68] S. Manotham, M. Kishi, Z. He, and K. Hotate, "1-cm spatial resolution with large dynamic range in strain distributed sensing by Brillouin optical correlation domain reflectometry based on intensity modulation," Proc. SPIE **8351**, 835136 (2012).

[69] N. Hayashi, Y. Mizuno, and K. Nakamura, "Distributed Brillouin sensing with centimeter-order spatial resolution in polymer optical fibers," J. Lightwave Technol. **32**(21), 3999 (2014).

[70] Y. Mizuno and K. Nakamura, "Experimental study of Brillouin scattering in perfluorinated polymer optical fiber at telecommunication wavelength," Appl. Phys. Lett. **97**(2), 021103 (2010).

[71] N. Hayashi, Y. Mizuno, and K. Nakamura, "Brillouin gain spectrum dependence on large strain in perfluorinated graded-index polymer optical fiber," Opt. Express

20(19), 21101 (2012).

[72] Y. Mizuno and K. Nakamura, "Potential of Brillouin scattering in polymer optical fiber for strain-insensitive high-accuracy temperature sensing," Opt. Lett. **35**(23), 3985 (2010).

[73] Y. Mizuno, N. Hayashi, and K. Nakamura, "Polarisation state optimisation in observing Brillouin scattering signal in polymer optical fibres," IEICE Electron. Lett. **49**(1), 56 (2013).

[74] Y. Mizuno, N. Hayashi, H. Fukuda, K. Y. Song, and K. Nakamura, "Ultrahigh-speed distributed Brillouin reflectometry," Light: Sci. Appl. **5**, e16184 (2016).

[75] A. Fellay, L. Thevenez, M. Facchini, M. Nikles, and P. Robert, "Distributed sensing using stimulated Brillouin scattering: towards ultimate resolution," Tech. Dig. Opt. Fiber Sens. **16**, 324 (1997).

[76] K. Hotate and Z. He, "Synthesis of optical-coherence function and its applications in distributed and multiplexed optical sensing," J. Lightwave Technol. **24**(7), 2541 (2006).

[77] Y. Peled, A. Motil, L. Yaron, and M. Tur, "Slope-assisted fast distributed sensing in optical fibers with arbitrary Brillouin profile," Opt. Express **19**(21), 19845 (2011).

[78] A. Minardo, A. Coscetta, R. Bernini, and L. Zeni, "Heterodyne slope-assisted Brillouin optical time-domain analysis for dynamic strain measurements," J. Opt. **18**(2), 025606 (2016).

[79] S. Takahashi and S. Shibata, "Thermal variation of attenuation for optical fibers," J. Non-Cryst. Solids **30**(3), 359 (1979).

[80] Y. Koike, "The future of plastic optical fiber," NPG Asia Mater. 1, 22 (2009).

[81] A. Yeniay, J. M. Delavaux, and J. Toulouse, "Spontaneous and stimulated Brillouin scattering gain spectra in optical fibers," J. Lightwave Technol. **20**(8), 1425 (2002).

[82] K.Y. Song, Z. He, K. Hotate, "Optimization of Brillouin optical correlation-domain analysis system based on intensity modulation scheme," Opt. Express **14**(10), 4256 (2006).

[83] S. Todoroki, "In-situ observation of fiber-fuse propagation," Jpn. J. Appl. Phys. **44**, 4022 (2005)

[84] Y. Mizuno, N. Hayashi, H. Tanaka, K. Nakamura, S. Todoroki, "Observation of polymer optical fiber fuse," Appl. Phys. Lett. **104** 043302 (2014).

[85] Y. Mizuno, N. Hayashi, H. Tanaka, K. Nakamura, "Spiral propagation of polymer optical fiber fuse accompanied by spontaneous burst and its real-time monitoring using Brillouin scattering," IEEE Photon. J. **6,** 6600307 (2014).

[86] M. Kashiwagi and K. Hotate, "Long range and high resolution reflectometry by synthesis of optical coherence function at region beyond the coherence length," IEICE Electron. Express **6**(8), 497 (2009).

[87] O. Furukawa, S. Tezuka, M. Tsukamoto, S. Matsuura, M. Kishi, and K. Hotate, "Beyond 21 km distributed strain measurement with Brillouin optical correlation domain reflectometry using polarization diversity method and temporal gating scheme," IEEJ Trans. Fundam. Mater. **137**(1), 52 (2017). [in Japanese]

[88] S. Matsuo, M. Ikeda, H. Kutami, and K. Himeno, "Low-bending-loss and low-splice-loss single-mode fibers," IEICE Trans. Electron. **E88-C**, 889 (2005).

[89] S. Matsuo, T. Nunome, K. Himeno, and H. Tsuchiya, "Dispersion and splice characteristics of bend-insensitive fibers with trench index profile compliant with G.652," IEICE Trans. Electron. **E91-C**, 1129 (2008).

[90] Y. Sasaki, K. Okamoto, T. Hosaka, and N. Shibata, "Polarization-maintaining and absorption-reducing fibers," in Optical Fiber Communication Conference, 1982 OSA Technical Digest Series (Optical Society of America, 1982), paper ThCC6.

[91] M. O. van Deventer and A. J. Boot, "Polarization properties of stimulated Brillouin scattering in single-mode fibers," J. Lightwave Technol. **12**(4), 585 (1994).

[92] L. Zou, X. Bao, F. Ravet, and L. Chen, "Distributed Brillouin fiber sensor for detecting pipeline buckling in an energy pipe under internal pressure," Appl. Opt. **45**, 3372 (2006).

[93] S. Villalba and J. R. Casas, "Application of optical fiber distributed sensing to health monitoring of concrete structures," Mech. Syst. Signal Process **39,** 441 (2013).

[94] X. Zhao, P, Gong, G. Qiao, J. Lu, X. Lv, and J. Qu, "Brillouin corrosion expansion sensors for steel reinforced concrete structures using a fiber optic coil

winding method," Sensors **11**, 10798 (2011).

[95] D. G. Pearce, "Understanding CFRP as a design material," Fibre Sci. Technol. **3**(2), 129 (1970).

[96] U. Meier, "Carbon fiber-reinforced polymers: modern materials in bridge engineering," Struct. Eng. Int. **2**(1), 7 (1992).

[97] C. Soutis, "Carbon fiber reinforced plastics in aircraft construction," Mater. Sci. Eng. A **412**(1-2), 171 (2005).

[98] S. Rizkalla, M. Dawood, and D. Schnerch, "Development of a carbon fiber reinforced polymer system for strengthening steel structures," Composites Part A **39**(2), 388 (2008).

[99] G. Mieda, H. Nakamura, T. Matsui, Y. Ochi, Y. Mizuno, K. Nakamura, and Y. Matsumoto, "Bond strength of CFRP molded on steel surface by VaRTM technology and its fiber optic sensing," Proc. Asia–Pacific Conf. FRP in Structures (APFIS), 2017, P78.

[100] C. Dong, "Development of a process model for the vacuum assisted resing transfer molding simulation by the response surface method," Composites Part A **37**(9), 1316 (2006).

Related publications

A. Journal papers

[1] H. Lee, N. Hayashi, Y. Mizuno, and K. Nakamura, "Refractive index sensing using V-shaped polymer optical fibers," Jpn. J. Appl. Phys., vol. 54, no. 11, 118001 (2015).

[2] H. Lee, N. Hayashi, Y. Mizuno, and K. Nakamura, "Observation of Brillouin gain spectrum in optical fibers in telecommunication band: effect of pump wavelength," IEICE Electron. Express, vol. 13, no. 3, 20151066 (2016).

[3] H. Lee, N. Hayashi, Y. Mizuno, and K. Nakamura, "Slope-assisted Brillouin optical correlation-domain reflectometry: proof of concept," IEEE Photon. J., vol. 8, no. 3, 6802807 (2016).

[4] H. Lee, N. Hayashi, Y. Mizuno, and K. Nakamura, "Operation of slope-assisted Brillouin optical correlation-domain reflectometry: comparison of system output with actual frequency shift distribution," Opt. Express, vol. 24, no. 25, pp. 29190-29197 (2016).

[5] H. Lee, N. Hayashi, Y. Mizuno, and K. Nakamura, "Slope-assisted Brillouin optical correlation-domain reflectometry using polymer optical fibers with high propagation loss," J. Lightwave Technol., vol. 35, no. 11, pp. 2306-2310 (2017).

[6] H. Lee, Y. Mizuno, and K. Nakamura, "Measurement sensitivity dependencies on incident power and spatial resolution in slope-assisted Brillouin optical correlation-domain reflectometry," Sens. Actuat. A: Phys., vol. 268, pp. 68-71 (2017).

[7] H. Lee, Y. Mizuno, and K. Nakamura, "Detection of 2-mm-long strained section in silica fiber using slope-assisted Brillouin optical correlation-domain reflectometry," Jpn. J. Appl. Phys., vol. 57, no. 2, 020303 (2018).

[8] H. Lee, T. Ma, Y. Mizuno, and K. Nakamura, "Bending-loss-independent operation of slope-assisted Brillouin optical correlation-domain reflectometry," Sci. Rep., vol. 8, 7844 (2018).

[9] H. Lee, Y. Ochi, T. Matsui, Y. Matsumoto, Y. Tanaka, H. Nakamura, Y. Mizuno, and K. Nakamura, "Distributed strain measurement and possible breakage detection of optical-

fiber-embedded composite structure using slope-assisted Brillouin optical correlation-domain reflectometry," Appl. Phys. Express, vol. 11, no. 7, 072501 (2018).

[10] H. Lee, K. Noda, Y. Mizuno, and K. Nakamura, "Distributed temperature sensing based on slope-assisted Brillouin optical correlation-domain reflectometry with over 10 km measurement range," Electron. Lett., vol. 55, no. 5, pp. 276-278 (2019).

[11] H. Lee, Y. Mizuno, and K. Nakamura, "Enhanced stability and sensitivity of slope-assisted Brillouin optical correlation-domain reflectometry using polarization-maintaining fibers," OSA Contin., vol. 2, no. 3, pp. 874-880 (2019).

[12] H. Lee, K. Noda, Y. Mizuno, and K. Nakamura, "Trade-off relation between strain dynamic range and spatial resolution in slope-assisted Brillouin optical correlation-domain reflectometry," Meas. Sci. Technol., vol. 30, no. 7, 075204 (2019).

[13] N. Hayashi, H. Lee, Y. Mizuno, and K. Nakamura, "Observation of backward guided-acoustic-wave Brillouin scattering in optical fibers using pump-probe technique," IEEE Photon. J., vol. 8, no. 3, 7100707 (2016).

[14] M. Shizuka, H. Lee, N. Hayashi, Y. Mizuno, and K. Nakamura, "Simplified optical correlation-domain reflectometry employing proximal reflection point," Jpn. J. Appl. Phys., vol. 55, no. 12, 128003 (2016).

[15] S. Shimada, H. Lee, M. Shizuka, H. Tanaka, N. Hayashi, Y. Matsumoto, Y. Tanaka, H. Nakamura, Y. Mizuno, and K. Nakamura, "Refractive index sensing using ultrasonically crushed polymer optical fibers," Appl. Phys. Express, vol. 10, no. 1, 012201 (2017) [Featured in "Spotlights"].

[16] T. Kawa, G. Numata, H. Lee, N. Hayashi, Y. Mizuno, and K. Nakamura, "Single-end-access strain and temperature sensing based on multimodal interference in polymer optical fibers," IEICE Electron. Express, vol. 14, no. 3, 20161239 (2017).

[17] Y. Mizuno, H. Ujihara, H. Lee, N. Hayashi, and K. Nakamura, "Polymer optical fiber tapering using hot water," Appl. Phys. Express, vol. 10, no. 6, 062502 (2017).

[18] T. Kawa, G. Numata, H. Lee, N. Hayashi, Y. Mizuno, and K. Nakamura, "Temperature sensing based on multimodal interference in polymer optical fibers: room-temperature sensitivity enhancement by annealing," Jpn. J. Appl. Phys., vol. 56, no. 7, 078002 (2017).

[19] Y. Mizuno, H. Lee, S. Shimada, Y. Matsumoto, Y. Tanaka, H. Nakamura, and K. Nakamura, "Pilot demonstration of refractive index sensing using polymer optical fiber crushed with slotted screwdriver," IEICE Electron. Express, vol. 14, no. 21, 20170962 (2017).

[20] R. Ishikawa, H. Lee, A. Lacraz, A. Theodosiou, K. Kalli, Y. Mizuno, and K. Nakamura, "Pressure dependence of fiber Bragg grating inscribed in perfluorinated polymer fiber,"

IEEE Photon. Technol. Lett., vol. 29, no. 24, pp. 2167-2170 (2017).

[21] N. Matsutani, H. Lee, Y. Mizuno, and K. Nakamura, "Long-term stability enhancement of Brillouin measurement in polymer optical fibers using amorphous fluoropolymer," Jpn. J. Appl. Phys., vol. 57, no. 1, 018001 (2018).

[22] Y. Mizuno, H. Lee, N. Hayashi, and K. Nakamura, "Hydrostatic pressure dependence of Brillouin frequency shift in polymer optical fibers," Appl. Phys. Express, vol. 11, no. 1, 012502 (2018).

[23] R. Ishikawa, H. Lee, A. Lacraz, A. Theodosiou, K. Kalli, Y. Mizuno, and K. Nakamura, "Strain dependence of perfluorinated polymer optical fiber Bragg grating measured at different wavelengths," Jpn. J. Appl. Phys., vol. 57, no. 3, 038002 (2018).

[24] A. G. Leal-Junior, A. Frizera, M. J. Pontes, P. Antunes, N. Alberto, M. F. Domingues, H. Lee, R. Ishikawa, Y. Mizuno, K. Nakamura, P. André, and C. A. F. Marques, "Dynamic mechanical analysis on fused polymer optical fibers: towards sensor applications," Opt. Lett., vol. 43, no. 8., pp. 1754-1757 (2018).

[25] Y. Mizuno, S. Hagiwara, T. Kawa, H. Lee, and K. Nakamura, "Displacement sensing based on modal interference in polymer optical fibers with partially applied strain," Jpn. J. Appl. Phys., vol. 57, no. 5, 058002 (2018).

[26] A. G. Leal-Junior, A. Frizera, H. Lee, Y. Mizuno, K. Nakamura, T. Paixão, C. Leitão, M. F. Domingues, N. Alberto, P. Antunes, P. André, C. A. F. Marques, and M. J. Pontes, "Strain, temperature, moisture, and transverse force sensing using fused polymer optical fibers," Opt. Express, vol. 26, no. 10, pp. 12939-12947 (2018).

[27] Y. Mizuno, G. Numata, T. Kawa, H. Lee, N. Hayashi, and K. Nakamura, "Multimodal interference in perfluorinated polymer optical fibers: Application to ultrasensitive strain and temperature sensing," IEICE Trans. Electron., vol. E101-C, no. 7, pp. 602-610 (2018) <invited review>.

[28] A. G. Leal-Junior, A. Frizera, H. Lee, Y. Mizuno, K. Nakamura, C. Leitão, M. F. Domingues, N. Alberto, P. Antunes, P. André, C. A. F. Marques, and M. J. Pontes, "Design and characterization of curvature sensor using fused polymer optical fibers," Opt. Lett., vol. 43, no. 11, pp. 2539-2542 (2018).

[29] Y. Mizuno, H. Lee, and K. Nakamura, "Recent advances in Brillouin optical correlation-domain reflectometry," Appl. Sci., vol. 8, no. 10, 1845 (2018) <invited review>.

[30] Y. Mizuno, N. Matsutani, N. Hayashi, H. Lee, M. Tahara, H. Hosoda, and K. Nakamura, "Brillouin characterization of slimmed polymer optical fibers for strain sensing with extremely wide dynamic range," Opt. Express, vol. 26, no. 21, pp. 28030-28037 (2018).

[31] K. Noda, G. Han, H. Lee, Y. Mizuno, and K. Nakamura, "Proposal of external modulation

scheme for fiber-optic correlation-domain distributed sensing," Appl. Phys. Express, vol. 12, no. 2, 022005 (2019).

[32] Y. Mizuno, T. Ma, R. Ishikawa, H. Lee, A. Theodosiou, K. Kalli, and K. Nakamura, "Lorentzian demodulation algorithm for multimode polymer optical fiber Bragg gratings," Jpn. J. Appl. Phys., vol. 58, no. 2, 028003 (2019).

[33] Y. Mizuno, S. Hagiwara, N. Matsutani, K. Noda, H. Lee, and K. Nakamura, "Observation of multimodal interference in millimeter-long polymer optical fibers," IEICE Electron. Express, vol. 16, no. 8, 20190135 (2019).

[34] Y. Mizuno, H. Lee, N. Hayashi, and K. Nakamura, "Noise suppression technique for distributed Brillouin sensing with polymer optical fibers," Opt. Lett., vol. 44, no. 8, pp. 2097-2100 (2019).

[35] Y. Mizuno, R. Ishikawa, H. Lee, A. Theodosiou, K. Kalli, and K. Nakamura, "Potential of discriminative sensing of strain and temperature using perfluorinated polymer FBG," IEEE Sens. J., vol. 19, no. 12, pp. 4458-4462 (2019).

[36] K. Noda, H. Lee, Y. Mizuno, and K. Nakamura, "First demonstration of Brillouin optical correlation-domain reflectometry based on external modulation scheme," Jpn. J. Appl. Phys., vol. 58, no. 6, 068004 (2019).

[37] Y. Mizuno, S. Hagiwara, H. Lee, Y. Ochi, T. Matsui, Y. Matsumoto, Y. Tanaka, H. Nakamura, and K. Nakamura, "Infrared thermometry for breakage detection of optical fibers embedded in structures," Appl. Phys. Express, vol. 12, no. 6, 062007 (2019).

[38] Y. Mizuno, G. Han, K. Noda, H. Lee, and K. Nakamura, "Low-cost Brillouin optical correlation-domain reflectometry involving merely one fibre amplifier," Electron. Lett., vol. 55, no. 13, pp. 754-756 (2019) [Featured: "Reflect on this: Optical reflectometry implemented using only one fibre amplifier for distributed strain sensing," Electron. Lett., vol. 55, no. 13, p. 720 (2019)].

[39] Y. Mizuno, T. Ma, R. Ishikawa, H. Lee, A. Theodosiou, K. Kalli, and K. Nakamura, "Twist dependencies of strain and temperature sensitivities of perfluorinated graded-index polymer optical fiber Bragg gratings," Appl. Phys. Express, vol. 12, no. 8, 082007 (2019).

B. Selected international conference papers

[40] H. Lee, N. Hayashi, Y. Mizuno, and K. Nakamura, "Refractive index sensing using V-shaped plastic optical fibers," 8th IEEE International Conference on Advanced Infocomm Technology (ICAIT 2015), paper C4-4, Hangzhou, China, October 25-27, 2015.

[41] H. Lee, N. Hayashi, Y. Mizuno, and K. Nakamura, "Proof of concept for Brillouin optical correlation-domain reflectometry assisted by spectral slope," 21st OptoElectronics and Communication Conference and International Conference on Photonics in Switching (OECC/PS 2016), paper WC4-4, Niigata, Japan, July 3-7, 2016.

[42] H. Lee, N. Hayashi, Y. Mizuno, and K. Nakamura, "POF-based slope-assisted Brillouin optical correlation-domain reflectometry," 25th International Conference on Plastic Optical Fibres (POF 2016), paper OP4, Birmingham, UK, September 13-15, 2016.

[43] H. Lee, N. Hayashi, Y. Mizuno, and K. Nakamura, "Beyond-nominal-resolution distributed strain sensing by slope-assisted Brillouin optical correlation-domain reflectometry," 6th Asia-Pacific Optical Sensors Conference (APOS 2016), paper W4A.16, Shanghai, China, October 11-14, 2016.

[44] H. Lee, N. Hayashi, Y. Mizuno, and K. Nakamura, "Power-based Brillouin optical correlation-domain reflectometry for high-speed distributed sensing," 3rd Annual World Congress of Smart Materials (WCSM 2017), paper 501-1630, Bangkok, Thailand, March 16-18, 2017.

[45] H. Lee, N. Hayashi, Y. Mizuno, and K. Nakamura, "Slope-assisted Brillouin optical correlation-domain reflectometry using high-loss plastic optical fibers," 25th International Conference on Optical Fibre Sensors (OFS-25), paper We-P117, Jeju, Korea, April 24-28, 2017.

[46] H. Lee, Y. Mizuno, and K. Nakamura, "Operation of power-based BOCDR: measurement sensitivity influenced by spatial resolution," 12th Conference on Lasers and Electro-Optics Pacific Rim, 22nd OptoElectronics and Communications Conference, and 5th Photonics Global Conference (CLEO-PR/OECC/PGC 2017), paper s1720, Singapore, July 31-August 4, 2017.

[47] H. Lee, Y. Mizuno, and K. Nakamura, "Detection of 5-mm-long heated section in plastic optical fiber using slope-assisted BOCDR," 26th International Conference on Plastic Optical Fibres (POF 2017), paper 62, Aveiro, Portugal, September 13-15, 2017 [POF2017 Best Student Paper Award].

[48] H. Lee, Y. Mizuno, and K. Nakamura, "Detection of world's shortest hot spots in silica and plastic optical fibers by slope-assisted Brillouin optical correlation-domain

reflectometry," 22nd International Microoptics Conference (MOC 2017), paper H-4, Tokyo, Japan, November 19-22, 2017 [MOC2017 Student Award].

[49] H. Lee, Y. Mizuno, N. Hayashi, and K. Nakamura, "Pressure dependence of Brillouin frequency shift in plastic optical fibers," 22nd International Microoptics Conference (MOC 2017), paper P-106, Tokyo, Japan, November 19-22, 2017.

[50] H. Lee, Y. Ochi, T. Matsui, Y. Matsumoto, Y. Tanaka, H. Nakamura, Y. Mizuno, and K. Nakamura, "Health monitoring of composite structure based on slope-assisted Brillouin optical correlation-domain reflectometry," 7th Asia-Pacific Optical Sensors Conference (APOS 2018), paper Tue_9, Matsue, Japan, May 28-31, 2018 [APOS2018 Student Paper Award].

[51] H. Lee, Y. Mizuno, and K. Nakamura, "Highly sensitive slope-assisted BOCDR utilizing polarization-maintaining fiber," 23rd OptoElectronics and Communications Conference (OECC 2018), paper 6C1-2, Jeju, Korea, July 2-6, 2018.

[52] H. Lee, Y. Mizuno, and K. Nakamura, "Slope-assisted Brillouin optical correlation-domain reflectometry with strain dynamic range limited by "Mt. Fuji" shaped noise floor," 10th International Conference on Information Optics and Photonics (CIOP 2018), paper 000347, Beijing, China, July 8-11, 2018.

[53] H. Lee, Y. Mizuno, and K. Nakamura, "Enhanced strain dynamic range of slope-assisted Brillouin optical correlation-domain reflectometry," Asia Communications and Photonics Conference (ACP 2018), paper Su1B.2, Hangzhou, China, October 26-29, 2018.

[54] H. Lee, Y. Mizuno, and K. Nakamura, "Slope-assisted Brillouin optical correlation-domain reflectometry: from fundamentals to applications," Asia Communications and Photonics Conference (ACP 2018), paper S3B.2, Hangzhou, China, October 26-29, 2018 <invited>.

[55] H. Lee, K. Noda, Y. Mizuno, and K. Nakamura, "Distributed strain measurement using power-based Brillouin sensor with three folded dynamic range," 7th International Symposium on Sensor Science (I3S 2019), paper S5-1700, Naples, Italy, May 9-11, 2019.

[56] H. Lee, Y. Mizuno, N. Hayashi, and K. Nakamura, "Noise-suppressed distributed Brillouin sensing using plastic optical fibers," 24th OptoElectronics and Communications Conference and International Conference on Photonics in Switching and Computing (OECC/PSC 2019), paper WP4-C3, Fukuoka, Japan, July 7-11, 2019.

[57] H. Lee, K. Noda, Y. Mizuno, and K. Nakamura, "Real-time distributed fiber sensing based on slope-assisted BOCDR," 18th International Conference on Optical Communications and Networks (ICOCN 2019), paper W1F.2, Huangshan, China, August 5-8, 2019 <invited>.

C. Selected domestic conference papers

[58] 李熙永、林寧生、水野洋輔、中村健太郎, “散乱スペクトルの傾斜を用いたブリルアン光相関領域リフレクトメトリ”, 応用物理学会第57回光波センシング技術研究会(LST-57), pp. 123-128, 東京理科大学神楽坂キャンパス, 2016年6月14日-15日.

[59] 李熙永、林寧生、水野洋輔、中村健太郎, “傾斜利用BOCDRのプラスチック光ファイバへの適用”, 応用物理学会第58回光波センシング技術研究会(LST-58), pp. 27-32, 東京理科大学神楽坂キャンパス, 2016年12月8日-9日.

[60] 李熙永、林寧生、水野洋輔、中村健太郎, “プラスチック光ファイバを用いた歪・温度分布の高速測定”, 第30回光通信システム(OCS)シンポジウム, P-6, 三島東レ総合研修センター, 2016年12月20日-21日.

[61] 李熙永、林寧生、水野洋輔、中村健太郎, “傾斜利用BOCDRによる理論空間分解能を超えた極短歪の検出”, 応用物理学会第59回光波センシング技術研究会(LST-59)講演論文集, pp. 195-200, 東京理科大学神楽坂キャンパス, 2017年6月6日-7日.

[62] 李熙永、水野洋輔、中村健太郎, “傾斜利用BOCDRによる世界最短歪の検出”, 電子情報通信学会2017年度第2回光ファイバ応用技術研究会(OFT)講演論文集, pp. 5-8, 北海道大学, 2017年8月31日-9月1日 [光ファイバ応用技術研究会学生奨励賞受賞].

[63] 李熙永、水野洋輔、中村健太郎, “リアルタイムひずみ分布計測”, 光ファイバセンシング振興協会第9回シンポジウム, paper P-7, 東京工業大学大岡山キャンパス, 2017年10月30日.

[64] 李熙永、萩原園子、越智寛、松井孝洋、松本幸大、田中洋介、中村一史、水野洋輔、中村健太郎, “炭素繊維強化プラスチックに埋め込んだ光ファイバに沿った歪分布測定と破断点検出”, 応用物理学会第60回光波センシング技術研究会(LST-60)講演論文集, pp. 99-104, 東京理科大学神楽坂キャンパス, 2017年12月5日-6日.

[65] 李熙永、越智寛、松井孝洋、松本幸大、田中洋介、中村一史、水野洋輔、中村健太郎, “構造物に埋め込んだ光ファイバに沿った歪分布の高空間分解能測定”, 第31回光通信システム(OCS)シンポジウム, P-8, 三島東レ総合研修センター, 2017年12月19日-20日.

[66] 李熙永、萩原園子、越智寛、松井孝洋、松本幸大、田中洋介、中村一史、水野洋輔、中村健太郎, “傾斜利用BOCDRによる光ファイバを埋め込んだ複合材料構造の健全性診断”, 電子情報通信学会2017年度第6回光ファイバ応用技術研究会(OFT)講演論文集, pp. 11-16, 沖縄県立博物館, 2018年2月15-16日.

[67] 李熙永、水野洋輔、中村健太郎, “PMFを用いた傾斜利用BOCDRの特性評価”, 電子情報通信学会2018年度第1回光ファイバ応用技術研究会(OFT)講演論文集, pp. 11-16, 機械振興会館, 2018年5月18日.

[68] 李熙永、水野洋輔、中村健太郎, “PANDAファイバを用いた傾斜利用BOCDR”, 応用物理学会第61回光波センシング技術研究会(LST-61)講演論文集, pp. 71-76, 東京理科大学神楽坂キャンパス, 2018年6月12日-13日.

[69] 李熙永、水野洋輔、中村健太郎, “傾斜利用BOCDRによる長距離分布測定”, 電子情報通信学会2018年度第3回光ファイバ応用技術研究会(OFT)講演論文集, pp. 145-148, 東北大学電気通信研究所, 2018年10月11日-12日 [光ファイバ応用技術研究会学生ポスター奨励賞受賞].

[70] 李熙永、野田康平、水野洋輔、中村健太郎, “Noise reduction in POF-based Brillouin sensing”, 電子情報通信学会2019年度第1回光ファイバ応用技術研究会(OFT)講演論文集, pp. 1-6, 大阪府立大学I-siteなんば, 2019年5月16日-17日.

D. Selected domestic annual meeting presentations

[71] 李熙永、林寧生、水野洋輔、中村健太郎, “V字に曲げたプラスチック光ファイバを用いた屈折率センシング”, 2015年(平成27年)秋季第76回応用物理学会学術講演会, 13p-2K-8, 名古屋国際会議場、2015年9月13日-16日.

[72] 李熙永、林寧生、水野洋輔、中村健太郎, “光ファイバ中のブリルアン利得スペクトルの励起光波長依存性”, 2016年(平成28年)春季第63回応用物理学関連連合講演会, 20p-P6-3, 東京工業大学大岡山キャンパス、2016年3月19日-22日.

[73] 李熙永、林寧生、水野洋輔、中村健太郎, “ブリルアン散乱スペクトルの傾斜を利用したBOCDR”, 2016年(平成28年)春季第63回応用物理学関連連合講演会, 19a-H116-12, 東京工業大学大岡山キャンパス、2016年3月19日-22日.

[74] 李熙永、水野洋輔、中村健太郎, “傾斜利用ブリルアン光相関領域反射計による世界最短ホットスポットの検出”, 2017年(平成29年)秋季第78回応用物理学会学術講演会, 6a-A414-8, 福岡国際会議場, 2017年9月5日-8日.

[75] 李熙永、水野洋輔、中村健太郎, “電気スペクトルアナライザのビデオ帯域幅の調整による傾斜利用BOCDRの歪ダイナミックレンジの向上”, 2017年(平成29年)秋季第78回応用物理学会学術講演会, 7a-PA5-13, 福岡国際会議場, 2017年9月5日-8日.

[76] 李熙永、水野洋輔、中村健太郎, “傾斜利用BOCDRを用いたCFRP補強鋼材中の歪分

布計測”, 2018年(平成30年)春季第65回応用物理学会学術講演会, 19a-C303-3, 早稲田大学西早稲田キャンパス, 2018年3月17日-20日.

[77] 李熙永、水野洋輔、中村健太郎, “傾斜利用ブリルアン光相関領域反射計による 10 km 遠方での温度分布測定”, 2018年(平成30年)秋季第79回応用物理学会学術講演会, 20a-PB5-9, 名古屋国際会議場, 2018年9月18日-21日.

[78] 李熙永、水野洋輔、中村健太郎, “傾斜利用ブリルアン光相関領域反射計のダイナミックレンジの向上”, 2018年日本光学会年次学術講演会 Optics & Photonics Japan (OPJ2018), 1pB3, 筑波大学東京キャンパス, 2018年10月30日-11月2日.

[79] 李熙永、野田康平、水野洋輔、中村健太郎, “プラスチック光ファイバを用いたブリルアン光相関領域反射計のノイズ低減法”, 2019年(平成31年)春季第66回応用物理学会学術講演会, 11p-PB2-7, 東京工業大学大岡山キャンパス, 2019年3月9日-12日.

E. Articles

[80] 科学新聞, “光ファイバーの世界最短変形区間 検出成功,” 2018 年 1 月 1 日 8 面.

[81] 水野洋輔、李熙永、林寧生、福田英幸、中村健太郎, “ロボットの”神経”に期待される超高速分布型光ファイバーセンサー,” OPTRONICS, vol. 36, no. 12, pp. 21-26 (2017).

F. Awards

1. 2017 年　Best Student Paper Award, 26th International Conference on Plastic Optical Fibres
2. 2017 年　MOC2017 Student Award, 22nd International Microoptics Conference
3. 2018 年　2017 年度 学生奨励賞, 光ファイバ応用技術研究会
4. 2018 年　Student Paper Award, 7th Asia-Pacific Optical Sensors Conference
5. 2018 年　学生ポスター奨励賞, 光ファイバ応用技術研究会
6. 2018 年　第 21 回 光設計奨励賞 (共同受賞), 日本光学会 光設計グループ